TOUGHREACT V3.0-OMP Sample Problems:

V3-OMP Sample Problem Authors: Tianfu Xu, Eric Sonnenthal, Nicolas Spycher, and Liange Zheng

Toughreact V3-OMP Code Authors: Eric Sonnenthal, Nicolas Spycher, Tianfu Xu, Liange Zheng, Norman Miller, and Karsten Pruess

Earth Sciences Division, Lawrence Berkeley National Laboratory
University of California, Berkeley, CA 94720

June -2014 - Draft

1 Sample Problems

The most efficient starting point for setting up a reactive transport simulation is by the use of well-tested input files from other simulations. Here we present applications of TOUGHREACT V3-OMP to problems in geothermal reservoirs, groundwater quality, nuclear waste isolation, supergene copper enrichment, and geologic disposal of greenhouse gases. The test problems also serve as checks and benchmarks to verify proper code installation. The input files can be used as templates to facilitate preparation of input data for new problems. To assist with checking on code performance, the distribution files include output files generated for each of the sample problems. These problems were run on a six-core (12-thread) Xeon Mac Pro workstation using Intel Fortran V14.0. The sample problems have also been tested on a Dell workstation running 64-bit MS Windows with the code compiled using the Intel Visual Fortran XE Composer v12.1, and on an Intel Xeon (8-core cpu) cluster running Linux and compiled with Intel Fortran V13. Slight differences in results may occur on different platforms or with different compilers and compiler options. Our tests have shown essentially identical results on these different systems.

1.1 Problem 1 – Aqueous Transport with Adsorption (Linear Kd) and Decay (EOS9)

A 1-D homogeneous fully water-saturated porous medium is considered (Figure 8.1-1), using the following parameters: a porosity of 0.1, a pore velocity v of 0.1 m/day, a solid density of 2600 kg/m^3, a distribution coefficient (Kd) of 0.042735 l/kg, which corresponds to a retardation factor R of 2 (Equation C.8 in Appendix C), and a half-life $t_{1/2}$ of 20 days. The flow system is a cylindrical, horizontal porous medium with cross-sectional area of 1 m^2 and 12 m length, divided into 60 grid blocks of 0.2 m thickness. Parameters for water flow are specified in file flow.inp (Fig. 8.1.2). Water chemical compositions are assigned through data in files solute.inp (Figure 8.1-3) and chemical.inp (Fig. 8.1.4). In chemical.inp, the record starting with "(1 1)" following the record 'INITIAL AND BOUNDARY WATER TYPES' specify that one initial water composition will be read, as well as one boundary water composition. The data entered in solute.inp under "default values of chemical zone codes for grid blocks" assign the first (and only) initial water type to all grid blocks in the problem, as well as assigning the first (only) boundary water composition to all injection grid blocks. Injection occurs only in block "F 1" (GENER block in file flow.inp), and with the boundary water chemical composition.

Figure 1.1—1 Simplified conceptual model for 1-D transport with linear Kd and decay

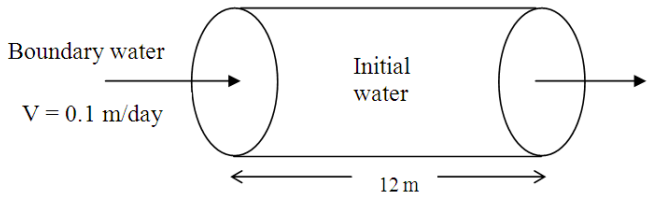

The EOS9 flow module is used. Part of the concentration output file is given in Figure 8.1-5. The complete input and output files are provided with the distribution files.

A total of four species are simulated in a single run. Species 1 is not subject to adsorption (R = 1) and decay ($t_{1/2}$ = infinite), and is denoted by 'na+' in chemical input file 'chemical.inp'. Species 2 has R = 2 and $t_{1/2}$ = infinite, and is denoted by 'skdd1' in the chemical input file 'chemical.inp'. Species 3 has a R = 1 and a $t_{1/2}$ = 20 days, and is denoted by 'skdd2' in the input file. Species 4 has R = 2 and $t_{1/2}$ = 20 days, and is denoted by 'skdd3' in the input file. Species skdd1, skdd2, and skdd3 are artificial tracer species. The species names must appear in the primary species block of the thermodynamic database. Initial concentrations for all four species are set equal to a very small value of 10^{-10} mol/l (practically zero, because TOUGHREACT uses log10 calculations for concentrations in order to avoid convergence problems). The inlet concentrations are set equal to 10^{-4} mol/l for all four species. An analytical solution for this problem is given in Javandel et al. (1984). In the numerical simulation, we give a diffusion coefficient of zero. Dispersion is not considered in this code. However, the upstream weighting scheme used in the code results in a numerical dispersivity $\alpha_n = \Delta x/2 = 0.1$ m (where Δx is the grid size, 0.2 m is used in the simulation). In the analytical calculations, we use a dispersion coefficient $D = \alpha_n v = 0.01$ m^2/day to account for the numerical dispersion in the simulation. The numerical results together with analytical solution are presented in Figure 8.1-6.

Figure 1.1—2 Flow input file (flow.inp) for Problem 1, transport with Kd and decay

```
# Transport of NaCl solution4
# EOS9 flow input
ROCKS----1----*----2----*----3----*----4----*----5----*----6----*----7----*----8
ROCK1     1      2600.        0.1   6.51E-12   6.51E-12   6.51E-12   0.00E+00      952.9
                                        0.00
REFCO           1.0E05        4.0

MULTI----1----*----2----*----3----*----4----*----5----*----6----*----7----*----8
    1     1     2     6          ! Isothermal case
START----1----*----2----*----3----*----4----*----5----*----6----*----7----*----8
REACT----1MOPR(20)-2----*----3----*----4----*----5----*----6----*----7----*----8
0002
PARAM----1----*-123456789012345678901234----*----5----*----6----*----7----*----8
   21000      5000030000000000000501005000
 0.00000E0   8.6400E6     1.e+01   8.64E+03F    1       -9.806650
    1.E-06
           1.001E+05                  4.0

RPCAP----1----*----2----*----3----*----4----*----5----*----6----*----7----*----8
    1            .333        -.1         1.         0.
    1       9.79020E3       .333         1.
TIMES----1----*----2----*----3----*----4----*----5----*----6----*----7----*----8
```

```
    2
   4.32e+6  8.6400E6
ELEME----1----*----2----*----3----*----4----*----5----*----6----*----7----*----8
A11 1              10.2000E+000.4000E+00          0.1000E+000.5000E+00-.5000E+00
A11 2              10.2000E+000.4000E+00          0.3000E+000.5000E+00-.5000E+00
A11 3              10.2000E+000.4000E+00          0.5000E+000.5000E+00-.5000E+00
...
CONNE----1----*----2----*----3----*----4----*----5----*----6----*----7----*----8
A11 1A11 2                  10.1000E+000.1000E+000.1000E+01
A11 2A11 3                  10.1000E+000.1000E+000.1000E+01
A11 3A11 4                  10.1000E+000.1000E+000.1000E+01
...

GENER----1----*----2----*----3----*----4----*----5----*----6----*----7----*----8
A11 1    0                  1     WATE  1.1576E-4          0.
A1160    0                  1     WATE -1.1576E-4          0.

INCON----1----*----2----*----3----*----4----*----5----*----6----*----7----*----8

ENDCY
```

Figure 1.1—3 Solute transport input file (solute.inp) for Problem 1, transport with Kd adsorption and decay

```
# Title
'Aqueous transport with Kd and decay'
#ISPIA,itersfa,ISOLVC,ngamm,NGAS1,ichdump,kcpl,Ico2h2o,iTDS_REACT
    2    1      5       1     0      0      2      0     0
#constraints for reactive chemical transport:  sl1min, rcour, stimax, cnfact
   1.00e-4       0.9       4.0       1.0
#Read input and output file names:
TherAkin10.dat                ! thermodynamic database
iter.dat                      ! iteration information
kdd_conc.dat                  ! aqueous concentrations in tecplot form
kdd_min.dat                   ! mineral data  in tecplot form
kdd_gas.dat                   ! gas data  in tecplot form
kdd_tim.dat                   ! concentrations at specific elements over time
#Weighting parameters
1.0       1.0    0.d-10   0.0d-05           ! itime wupc,dffun,dffung
#data to convergence criteria:
1 0.100E-03  300 0.100E-04   30 0.100E-05  0.00E-05  0.00E-05    !  TOLDC,TOLDR
#NWTI NWNOD NWCOM NWMIN NWAQ NWADS NWEXC iconflag minflag igasflag
   40    1    4    0     0     0     0      1       1        0
#pointer of nodes for writing in time:
A11 1
#pointer of components for writing:
    3    4    5    6
#pointer of minerals for writing:
0
#Individual aqueous species for which to output concentrations in time and plot
files:

#Adsorption species for which to output concentrations in time and plot files:

#Exchange species for which to output concentrations in time and plot files:

#IZIWDF IZBWDF IZMIDF IZGSDF IZADDF IZEXDF IZPPDF IZKDDF IZBGDF
     1      1       0      0      0      0      0     1     0
# ELEM(a5) NSEQ NADD IZIW IZBW IZMI IZGS IZAD IZEX izpp IZKD IZBG

# this "end" record is needed now
end
```

Figure 1.1—4 Chemical input file (chemical.inp) for Problem 1, transport with Kd adsorption and decay

```
# Title
```

```
'Aqueous transport with Kd and decay'
# '-------------------------------------------------------------------------------'
# 'DEFINITION OF THE GEOCHEMICAL SYSTEM'
# 'PRIMARY AQUEOUS SPECIES'
'h2o'       0
'h+'        0
'na+'       0
'skdd1'     0           ! species with Kd/decay
'skdd2'     0
'skdd3'     0
'*'
# 'AQUEOUS KINETICS'
'*'
# 'AQUEOUS COMPLEXES'
'oh-'
'*'
# 'MINERALS'
'*'
# 'GASES'
'*'
# 'SURFACE COMPLEXES'
'*'
# 'species with Kd and decay    decay constant(1/s)'
'skdd1'                 0.0d0        0.0  0.0     ! with only Kd
'skdd2'                 4.0113d-07   0.0  0.0     ! with only decay    t(1/2)=20
days
'skdd3'                 4.0113d-07   0.0  0.0     ! with both Kd and decay
'*'
# 'EXCHANGEABLE CATIONS'
'*'
#'-------------------------------------------------------------------------------'
# 'INITIAL AND BOUNDARY WATER TYPES'
1   1        !niwtype, nbwtype = number of initial and boundary waters
# Index  Speciation T(C)  P(bar)
1               25.0      1.0
#'        icon        guess         ctot         '
'h2o'      1        1.000d+0       1.000d+0       ,  ,   0.
'h+'       1        1.0000d-7      1.000d-7       ,  ,   0.
'na+'      1        1.000d-10      1.000d-10      ,  ,   0.
'skdd1'    1        1.000d-10      1.000d-10      ,  ,   0.
'skdd2'    1        1.000d-10      1.000d-10      ,  ,   0.
'skdd3'    1        1.000d-10      1.000d-10      ,  ,   0.
'*'
# Index  Speciation T(C)  P(bar)
1               25.0      1.0
#'       icon        guess         ctot         '
'h2o'      1        1.000d+0       1.000d+0       ,  ,   0.
'h+'       1        1.0000d-7      1.000d-7       ,  ,   0.
'na+'      1        1.000d-04      1.000d-04      ,  ,   0.
'skdd1'    1        1.000d-04      1.000d-04      ,  ,   0.
'skdd2'    1        1.000d-04      1.000d-04      ,  ,   0.
'skdd3'    1        1.000d-04      1.000d-04      ,  ,   0.
'*'
#'-------------------------------------------------------------------------------'
#'INITIAL MINERAL ZONES'
'*'
#'-------------------------------------------------------------------------------'
#'INITIAL AND INJECTION GAS ZONES'
'*'
#'-------------------------------------------------------------------------------'
#'Permeability-Porosity Zones'
'*'
#'-------------------------------------------------------------------------------'
#'INITIAL SURFACE ADSORPTION ZONES'
'*'
#'-------------------------------------------------------------------------------'
#'INITIAL LINEAR EQUILIBRIUM Kd ZONE'
1                              !kdtpye=number of Kd zones
1                              !idtype
#'species   solid-density(Sden,kg/dm**3)  Kd(l/kg=mass/kg solid / mass/l'
'skdd1'            0.0                 2.0
```

```
'skdd3'            0.0                 2.0
'*'
#'--------------------------------------if Sden=0 Kd store retardation factor'
#'INITIAL ZONES OF CATION EXCHANGE'
'*'
#'-------------------------------------------------------------------------'
#'end'
```

Figure 1.1—5 Part of aqueous concentrations output file (kdd_conc.dat) for Problem 1, transport with Kd adsorption and decay after 50 days (0.136896 yr)

X	Sl	T(C)	pH	t_na+	t_skdd1	t_skdd2	t_skdd3
0.100	0.1000E+01	4.000	6.9427	0.1000E-03	0.9996E-04	0.9352E-04	0.8782E-04
0.300	0.1000E+01	4.000	6.9427	0.1000E-03	0.9992E-04	0.8746E-04	0.7712E-04
0.500	0.1000E+01	4.000	6.9427	0.1000E-03	0.9988E-04	0.8180E-04	0.6773E-04
0.700	0.1000E+01	4.000	6.9427	0.1000E-03	0.9978E-04	0.7650E-04	0.5947E-04
0.900	0.1000E+01	4.000	6.9427	0.1000E-03	0.9940E-04	0.7154E-04	0.5217E-04
1.100	0.1000E+01	4.000	6.9427	0.1000E-03	0.9842E-04	0.6690E-04	0.4567E-04
1.300	0.1000E+01	4.000	6.9427	0.1000E-03	0.9639E-04	0.6257E-04	0.3979E-04
1.500	0.1000E+01	4.000	6.9427	0.1000E-03	0.9280E-04	0.5852E-04	0.3437E-04
1.700	0.1000E+01	4.000	6.9427	0.9999E-04	0.8723E-04	0.5472E-04	0.2931E-04
1.900	0.1000E+01	4.000	6.9427	0.9997E-04	0.7957E-04	0.5117E-04	0.2454E-04
2.100	0.1000E+01	4.000	6.9427	0.9993E-04	0.7006E-04	0.4785E-04	0.2006E-04
2.300	0.1000E+01	4.000	6.9427	0.9983E-04	0.5929E-04	0.4473E-04	0.1593E-04
2.500	0.1000E+01	4.000	6.9427	0.9963E-04	0.4810E-04	0.4180E-04	0.1225E-04
2.700	0.1000E+01	4.000	6.9427	0.9926E-04	0.3735E-04	0.3903E-04	0.9085E-05
2.900	0.1000E+01	4.000	6.9427	0.9860E-04	0.2774E-04	0.3639E-04	0.6490E-05
3.100	0.1000E+01	4.000	6.9428	0.9753E-04	0.1970E-04	0.3385E-04	0.4458E-05

Figure 1.1—6 Relative concentrations at 50 days for 1-D aqueous solute transport with adsorption (linear Kd) and decay (concentrations are normalized to the inlet concentration of 10-4 mol/l).

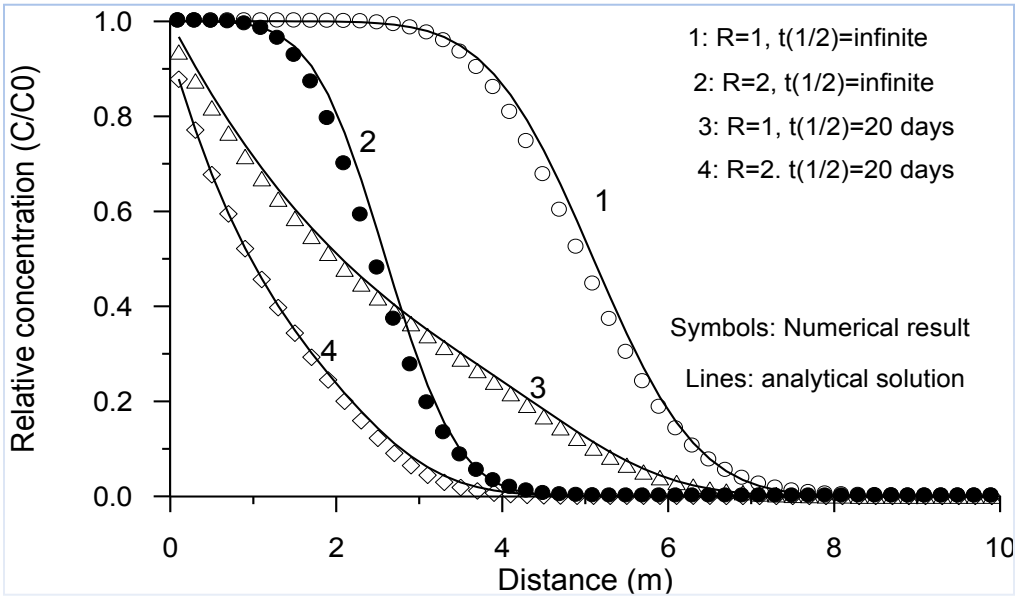

1.2 Problem 2 – Water Quality in the Aquia Aquifer, Maryland (EOS9)

$NaHCO_3$ type waters in coastal plain aquifers of the eastern United States have been related to freshening of the aquifer (Chapelle and Knobel, 1983). These investigators depict major cation concentration patterns as a function of flow length in the Aquia aquifer (Maryland). The water composition in this aquifer shows zonal bands with changes in concentrations of major cations that have been attributed to cation exchange and calcite dissolution/precipitation.

The observed water compositional pattern has been simulated previously using PHREEQM (Appelo, 1994). For the TOUGHREACT simulation, hydrological conditions and all input data are the same as those used in Appelo (1994). The aim is to validate our model applicability to field-scale ambient problems. Figure 8.2-1 shows a schematic cross section along a flow path. The aquifer is bounded to the east by a change in facies. The prepumping hydraulic head distribution suggests a confined aquifer in the upstream half and gradual loss of water in the downstream part of the aquifer (Chapelle and Drummond, 1983). Leakage probably occurs via Pleistocene channels that cut through the confining beds. The hydrological conditions have been modeled assuming a one-dimensional flow tube with recharge at x = 0, and with seepage into the confining layers evenly distributed over the second half of the flow tube.

Figure 1.2—1 **Schematic cross section of the Aquia aquifer (Maryland) adapted from Appelo (1994). Recharge occurs in the outcrop of the formation: discharge is assumed to take place evenly in the downstream half. (1 foot equals 0.3048 m; 1 mile equals 1.609 km).**

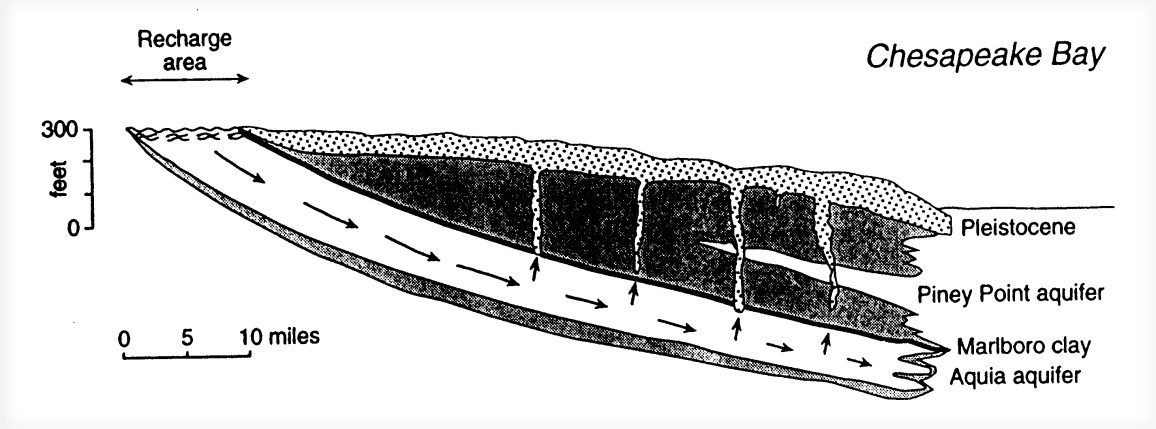

It was assumed that the initial water composition was brackish as a result of mixing of seawater with fresh water during deposition of the overlying Marlboro clay, a brackish water clay. The recharge water composition is presumed to be unchanged from that analyzed in the upstream reaches of the aquifer. The initial and recharge water compositions are presented in Table 8.2-1. These data are inferred from observations and paleohydrochemical conditions. A detailed analysis of

this problem is presented in Appelo (1994). To obtain the recharge water composition in the first 10 miles (16 km) of the flow path, the exchange capacity for the first 10 miles was set to zero.

Table 1.2—1 **Initial and recharge water composition (concentrations are given in mmol/l) for modeling the water quality patterns in the Aquia aquifer. X^- represents cation exchange sites. Data are from Appelo (1994).**

	pH	Na^+	K^+	Mg^{2+}	Ca^{2+}	Cl^-	HCO_3^-	SO_4^{2-}	X^-
Initial	6.80	87.4	1.92	9.98	4.31	10.8	15.75	0.27	2.00
Recharge	7.57	0.15	0.00	0.00	1.40	0.10	2.80	0.00	

The EOS9 flow module is used. The flow and solute transport input files are similar to the previous example. Here we only present the chemical input file in Figure 8.2-2. The complete input and output files are provided with the distribution files. The thermodynamic data used for aqueous species and mineral (calcite) can be found in the database file ThermAkin10.dat. Part of the output file for aqueous chemical concentrations is given in Figure 8.2-3. Parameters for water flow are specified in file flow.inp. A pore velocity of 2.42 mile/ka (1.2347×10^{-10} m/s) was used in the upper part of the aquifer. A porosity of 0.3 was used throughout. A dispersivity of 2.0 miles (3.2 km) was used by Appelo (1994). Dispersion is not treated in TOUGHREACT, and therefore it was approximated by setting the diffusion coefficient $D = \alpha v = 3.951\times10^{-7}$ m^2/s (entered in solute.inp) and setting the tortuosity to 1.0 in flow.inp.

Aqueous species chemical compositions are assigned in files solute.inp and chemical.inp. In chemical.inp, the record with "(1 1)" following the record 'INITIAL AND BOUNDARY WATER TYPES' specifies that one initial water composition as well as one boundary water composition will be read. The data entered in solute.inp under "default values of chemical zone codes for nodes" assign the first (and only) initial water type to all grid blocks in the problem, as well as assigning the first (only) boundary (recharge) water composition to all injection grid blocks. Recharge takes place only in grid block "F 1" using the boundary water chemical composition. The cation exchange reactions and their selectivities are listed in Table 8.2-2 (from Appelo, 1993). The Gaines-Thomas convention (Appelo, 1993) was used for cation exchange. In this convention, selectivities are calculated by using the equivalent fraction of the exchanged cations for the activity of the exchanged cations. It should be pointed out that selectivity is a relative concept. Na^+ was chosen as the reference. Therefore, Na^+ selectivity is equal to one. According to this definition, a lower selectivity corresponds to a higher exchange capacity. A divalent cation, in general, is more strongly exchanged than a monovalent cation. Usually, Ca^{2+} has a higher affinity for the exchange complex, usually in the following exchange order: $Ca^{2+} > Mg^{2+} > K^+ > Na^+$ (Appelo, 1993). Selectivity of H^+ is very sensitive in the simulation,

because it affects pH and thus calcite dissolution and the availability of Ca^{2+}. To obtain a better pH fit with the observations, the original H^+ selectivity (1.3092×10^{-6}) was adjusted to 3.1×10^{-6} (Figure 8.2-4).

Table 1.2—2 List of cation exchange reactions considered for modeling the water quality patterns in the Aquia aquifer (–X represents cation exchange sites). The cation selectivity listed is based on Appelo (1994).

Cation exchange	Selectivity (in terms of Na^+)
$Na^+ + 0.5Ca\text{-}X_2 = 0.5Ca^{2+} + Na\text{-}X$	0.3981
$Na^+ + 0.5Mg\text{-}X_2 = 0.5Mg^{2+} + Na\text{-}X$	0.5012
$Na^+ + K\text{-}X = K^+ + Na\text{-}X$	0.1995
$Na^+ + H\text{-}X = H^+ + Na\text{-}X$	1.3092×10^{-6}

Figure 1.2—2 Chemical input file (chemical.inp) for Problem 2.

```
# Title
'Water quality in the Aquia aquifer'
# '-------------------------------------------------------------------------------'
# 'DEFINITION OF THE GEOCHEMICAL SYSTEM'
# 'PRIMARY AQUEOUS SPECIES'
'h2o'       0
'h+'        0
'ca+2'      0
'mg+2'      0
'na+'       0
'k+'        0
'hco3-'     0
'so4-2'     0
'cl-'       0
'*'
# 'AQUEOUS KINETICS'
'*'
# 'AQUEOUS COMPLEXES'
'oh-'
'nahco3(aq)'
'cahco3+'
'mghco3+'
'co2(aq)'
'co3-2'
'caco3(aq)'
'mgso4(aq)'
'naso4-'
'kso4-'
'naco3-'
'*'
# 'MINERALS'          ! equilibrium mineral goes first
'calcite'           0    0      0    0
0.0   0.    0.00
'*'
# 'GASES'
'*'
# 'SURFACE COMPLEXES'
'*'
# 'species with Kd and decay    decay constant(1/s)'
'*'
```

```
# 'EXCHANGEABLE CATIONS'
1     1
# '                 master     convention     ex. coef.'
'na+'               1            1            1.0000
'k+'                0            1            0.1995
'ca+2'              0            1            0.3981
'mg+2'              0            1            0.5012
'h+'                0            1            3.1E-6      !initial:1.3092E-6
'*'
# '------------------------------------------------------------------------------'
# 'INITIAL AND BOUDARY WATER TYPES'
1   1        !niwtype, nbwtype = number of initial and boundary waters
# Index  Speciation T(C)  P(bar)
1     25.0   1.0
# '        icon        guess         ctot          '
'h2o'      1        1.000d+0       1.000d+0    '   '    0.
'h+'       3        1.585d-7       1.585d-7    '   '    0.       !pH=6.8
'ca+2'     1        2.000d-3       4.380d-3    '   '    0.
'mg+2'     1        5.000d-3       9.920d-3    '   '    0.
'na+'      1        8.000d-2       8.740d-2    '   '    0.
'k+'       1        1.000d-3       1.900d-3    '   '    0.
'hco3-'    1        1.000d-2       1.550d-2    '   '    0.
'so4-2'    1        1.500d-4       2.700d-4    '   '    0.
'cl-'      1        1.000d-1       1.018d-1    '   '    0.
'*'
# Index  Speciation T(C)  P(bar)
1     25.0   1.0
# '        icon        guess         ctot         '
'h2o'      1        1.000d+0       1.000d+0    '   '    0.
'h+'       3        2.692d-7       2.692d-7    '   '    0.       !pH=7.57
'ca+2'     1        1.000d-3       1.400d-3    '   '    0.
'mg+2'     1        0.600d-6       1.000d-6    '   '    0.
'na+'      1        0.800d-4       1.000d-4    '   '    0.
'k+'       1        3.000d-5       5.000d-5    '   '    0.
'hco3-'    1        1.000d-3       2.800d-3    '   '    0.
'so4-2'    1        0.500d-6       1.000d-6    '   '    0.
'cl-'      1        0.900d-4       1.000d-4    '   '    0.
'*'
# '------------------------------------------------------------------------------'
#  'INITIAL MINERAL ZONES'
 1                                    !nmtype= number of mineral zones
 1                                   !imtype
#  'mineral         vol.frac.'
 'calcite'            0.3     0
 '*'
# '------------------------------------------------------------------------------'
# 'INITIAL AND INJECTION GAS ZONES'
'*'
# '------------------------------------------------------------------------------'
# 'Permeability-Porosity Zones'
'*'
# '------------------------------------------------------------------------------'
# 'INITIAL SURFACE ADSORPTION ZONES'
'*'
# '---------------------------------------if Sden=0 Kd store retardation factor'
# 'INITIAL LINEAR EQUILIBRIUM Kd ZONE
'*'
# '---------------------------------------if Sden=0 Kd store retardation factor'
# 'INITIAL ZONES OF CATION EXCHANGE'
1                      !nxtype= number of exchange zones
# 'zone            ex. capacity(meq/100 g solid)'
1                   3.2345
'*'
# '------------------------------------------------------------------------------'
# 'end'
```

Figure 1.2—3 Part of aqueous concentrations output file (aqui_con.dat) for Problem 2, water quality in Aquia aquifer after 144×10^6 years.

X	pH	t_ca+2	t_mg+2	t_na+	t_k+	t_hco3-
6.000	7.5695	0.1913E-02	0.1871E-03	0.1027E-03	0.6555E-04	0.3483E-02
10.000	7.6173	0.1712E-02	0.3772E-03	0.1068E-03	0.8558E-04	0.3458E-02
14.000	7.6809	0.1479E-02	0.5899E-03	0.1155E-03	0.1201E-03	0.3427E-02
18.000	7.7471	0.1271E-02	0.7584E-03	0.1338E-03	0.1740E-03	0.3391E-02
22.000	7.8051	0.1117E-02	0.8446E-03	0.1719E-03	0.2504E-03	0.3346E-02
26.000	7.8560	0.1003E-02	0.8494E-03	0.2498E-03	0.3491E-03	0.3284E-02
30.000	7.9119	0.8954E-03	0.7864E-03	0.4075E-03	0.4625E-03	0.3195E-02
34.000	7.9925	0.7602E-03	0.6624E-03	0.7202E-03	0.5680E-03	0.3071E-02
38.000	8.1329	0.5650E-03	0.4749E-03	0.1320E-02	0.6149E-03	0.2920E-02
42.000	8.4233	0.2960E-03	0.2323E-03	0.2377E-02	0.5036E-03	0.2799E-02
46.000	8.7950	0.1259E-03	0.9092E-04	0.3343E-02	0.2829E-03	0.2867E-02
50.000	8.9168	0.9132E-04	0.6409E-04	0.3808E-02	0.1902E-03	0.3088E-02
54.000	8.8670	0.9270E-04	0.6558E-04	0.4191E-02	0.1728E-03	0.3459E-02
58.000	8.7568	0.1046E-03	0.7518E-04	0.4672E-02	0.1806E-03	0.4001E-02
62.000	8.6466	0.1185E-03	0.8662E-04	0.5218E-02	0.1956E-03	0.4626E-02
66.000	8.5777	0.1279E-03	0.9467E-04	0.5624E-02	0.2074E-03	0.5088E-02

The results after a simulation time of 144 ka are compared to observations of major cations and alkalinity (Figure 8.2-4). The agreement between numerical results and observations is reasonably satisfactory. The fit for Mg^{2+} can be further improved by adjusting Mg^{2+} selectivity. The sequential appearance of Mg^{2+} and K^{+} is attributed to chromatographic separation and can be varied in the model only by varying the Mg^{2+}/K^{+} selectivity. An apparent dip in alkalinity is observed just before Na^{+} concentrations increase, which is matched by the simulation. The upstream increase of Ca^{2+} concentrations in the region where K^{+} and Mg^{2+} are at a peak indicates an increased concentration of Ca-X_2 (X represents cation exchange sites). The increase occurred during flushing of Na^{+} and is due to dissolution of calcite. The increase of Na^{+} and alkalinity at the downstream end agrees with earlier conclusions about the development of $NaHCO_3$ water quality in a freshening aquifer (Chapelle and Knobel, 1983).

Figure 1.2—4 **Concentrations of Na+, K+, Mg2+, Ca2+, alkalinity, and pH along a flow path in the Aquia aquifer (Maryland). Symbols indicate observations provided by Appelo (1994) and originally from Chapelle and Knobel (1983); solid lines represent simulated concentrations using TOUGHREACT.**

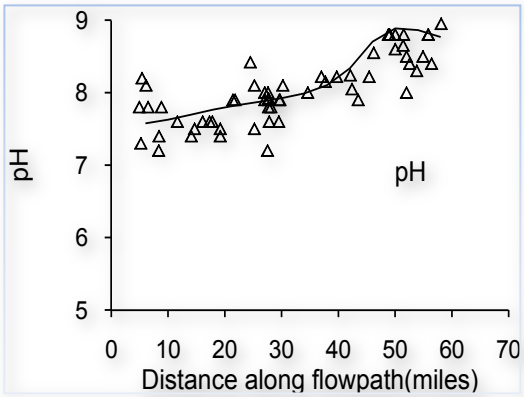

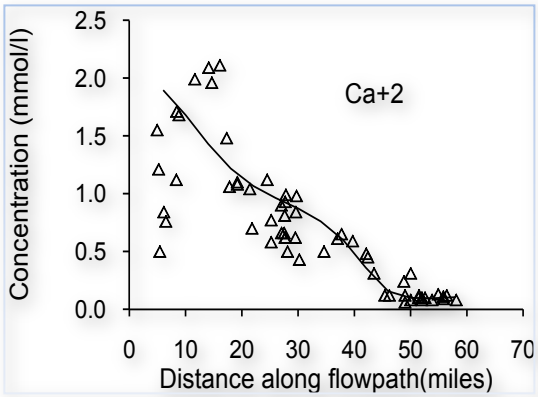

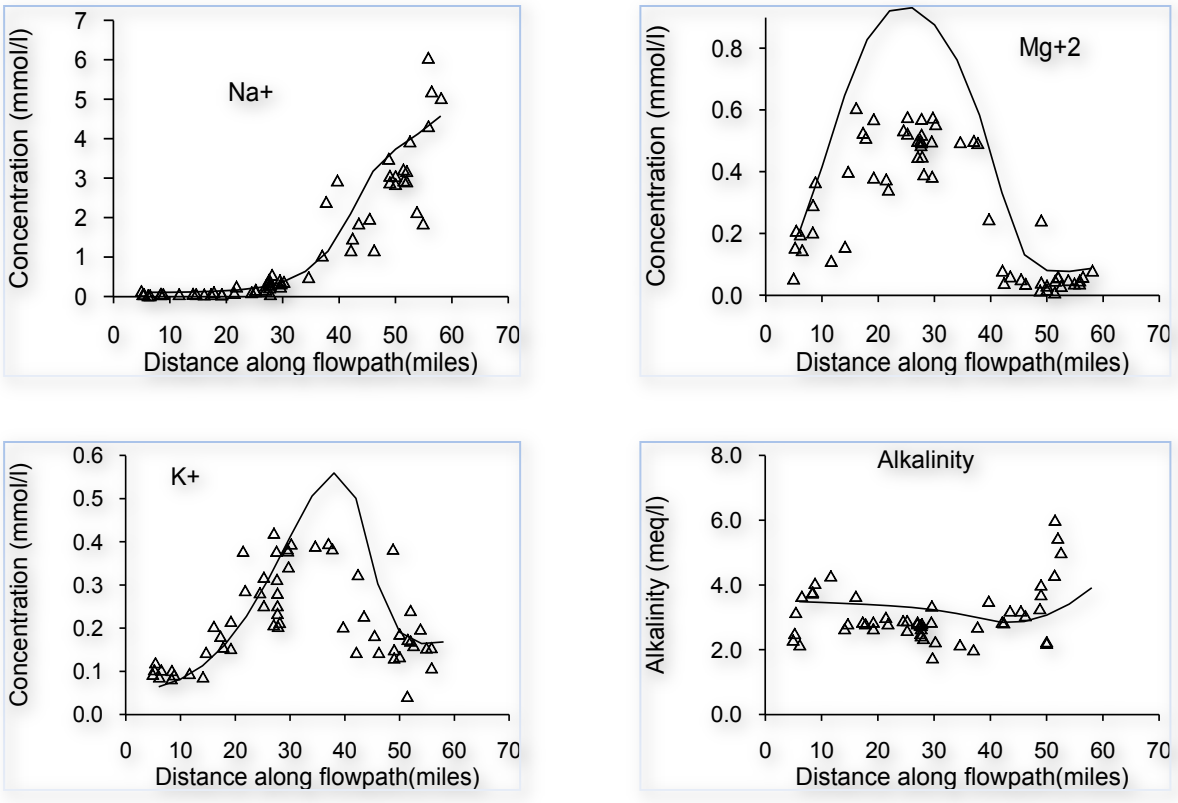

1.3 Problem 3 – Infiltration and Calcite Deposition at Yucca Mountain, Nevada (EOS3)

1.3.1 Problem statement

Yucca Mountain in southern Nevada (USA) is being investigated as a possible site for an underground nuclear waste repository. The semiarid environment and a thick (500 to 700 m) unsaturated zone (UZ) are considered to be favorable for long-term isolation of radioactive waste (Montazer and Wilson, 1984). The percolation flux in the UZ is an important parameter addressed in site characterization and hydrological modeling of Yucca Mountain, because it controls seepage into drifts that may contact waste packages. Hydrogenic calcite deposits in fractures and lithophysal cavities at Yucca Mountain were studied to estimate past percolation fluxes (Carlos et al., 1995; Vaniman and Chipera, 1996; Paces et al., 1998; Marshall et al., 1998; Marshall et al., 1999). These deposits provide evidence of water flow in the past and may improve an understanding of current and future UZ percolation rates, because direct measurements of infiltration fluxes over thousands of years are not possible.

An objective of these prior studies was to investigate the relationship between percolation flux and measured calcite abundances. The U.S. Geological Survey determined calcite abundances from a deep surface-based borehole (WT-24) (Paces et al., 2001) by measuring the CO_2 given off by heating of the rock. Geochronology work performed by the Geological Survey (Paces et al., 1998; Neymark et al., 2001) indicates that calcite formed over approximately 10 million years. Hydrogenic mineral coatings in the UZ are non-uniformly distributed and located almost entirely on fracture footwalls and cavity floors, in contrast to saturated environments, in which vein and cavity deposits usually coat all surfaces (Paces et al., 1998).

Here, we present some results of a reaction-transport numerical model for calcite deposition under different infiltration conditions using TOUGHREACT. The model considers a complete set of hydrological and geochemical processes, including the following essential factors affecting calcite precipitation: (1) infiltration, (2) the ambient geothermal gradient, (3) gaseous CO_2 diffusive transport and partitioning in liquid and gas phases, (4) fracture-matrix interaction for water flow and chemical constituents (dual permeability), and (5) water-rock interaction. In addition, any effects of water-rock interaction (e.g., pH modification) also affects the calcite solubility and hence its abundance in each rock unit. The dual permeability model allows us to address not only the abundances of calcite with depth, but also their relative abundances in fractures and in the rock matrix as a function of the hydrological/geochemical processes. More details on problem setup and results are given in Xu et al. (2003a).

1.3.2 Calcite precipitation mechanisms

Rainfall, along with wind-blown dust, carries much of the calcium to the surface (Vaniman et al., 2001). In the soil zone, strong evapotranspiration along with some water-rock interaction and root-zone biological processes leads to saturation with respect to calcite. The depth to reach calcite equilibrium depends on climate and infiltration variations over time and episodic water flow, as well as on near-surface biogeochemical conditions. During more typical smaller infiltration events, calcite may reach equilibrium close to the surface. However, large infiltration pulses of calcite-undersaturated water can dissolve near-surface calcite and reach equilibrium at a greater depth. Because we are primarily interested in calcite deposition in a deep geological unit, the Topopah Spring welded tuff (TSw), where the potential repository may be located, uncertainties in the infiltrating water composition near the surface are not significant because calcite reaches saturation well above this unit. In addition, the constant infiltration rate and steady-state water flow conditions over geological time used in our simulations are also justified by evidence that calcite growth in the UZ has remained approximately constant over at least the past 8 million years, as indicated by radiocarbon, ^{230}Th/U, and U-Pb ages (Paces et al., 1998).

The primary driving force for calcite precipitation from percolating waters in the UZ is its decreasing solubility with increasing temperature. Therefore, consideration of the ambient geothermal gradient is very important for calcite precipitation. The temperature distribution is a function of the crustal heat flow and the effect of infiltration, which has been evaluated in Sonnenthal and Bodvarsson (1998). The modeled temperature distributions in borehole WT-24 are discussed later. Pore waters extracted from deep locations of the Yucca Mountain rock matrix are close to equilibrium with respect to calcite (Paces et al., 2001), and no measurements of aqueous concentrations are available from fractures because they generally have low liquid saturations. Previous models for calcite precipitation, under conditions of local equilibrium (Marshall et al., 1999), have indicated that increased infiltration-percolation fluxes result in greater abundances of calcite precipitated over time. These models have not considered, however, effects such as water-rock interaction, changes to the geothermal gradient, and fracture-matrix interaction. They have also assumed a fixed partial pressure of CO_2.

The Ca concentration and CO_2 partial pressure in percolating water are major controlling factors for the abundance of calcite and its stability. This is a result of the decreasing solubility of CO_2 gas in water with increasing temperature, which in turn causes the following degassing process: $HCO_3^- + H^+ \rightarrow CO_2\ (g) + H_2O$. Gaseous CO_2 is also redistributed by gas phase diffusive transport. Degassing increases the pH, and then contributes to calcite precipitation: $Ca^{2+} + HCO_3^- \rightarrow CaCO_3$ (calcite) + H^+. Water and gas flow between fractures and the adjacent matrix governs the resulting calcite distribution within each medium. Calcite precipitation is also affected by other factors such as the dissolution and precipitation of aluminosilicate minerals (mainly through modifying the pH and the CO_2 partial pressure).

1.3.3 Hydrogeological and geochemical conditions

Hydrogeological Conditions

The Yucca Mountain UZ consists of layers of welded and non-welded volcanic tuffs. The welded and non-welded tuffs have vastly different hydrologic properties. The welded units are characterized by relatively low porosity, low matrix permeability, and high fracture density, whereas the nonwelded tuffs have higher matrix porosity and permeability, and lower fracture density (Liu et al., 1998; Sonnenthal and Bodvarsson, 1999). Montazer and Wilson (1984) developed a conceptual model for the UZ at Yucca Mountain that identified five main hydrogeological units based on the degree of welding and on the associated relationship to fracture intensity. This conceptual model has formed the basis for modeling flow in the UZ at Yucca Mountain. A schematic East-West cross-section through Yucca Mountain illustrating the major hydrogeological units in the UZ at Yucca Mountain is shown in Figure 8.3-1. Table 8.3-1 provides a description of the units, each of which is further

divided into a number of model layers with different hydrogeological and geochemical properties (Ahlers and Liu, 2000; Sonnenthal and Spycher, 2001; Spycher et al., 2003a). The Calico Hills nonwelded (CHn) unit is comprised of zeolitic and vitric nonwelded tuffs underlying the basal vitrophyre of the Topopah Spring Tuff. Below the CHn are the Crater Flat undifferentiated (CFu) units, consisting of the lower Bullfrog and Tram Tuffs of the Crater Flat Group. The hydrogeological units below the TSw were not considered in the geochemical transport simulations, so details regarding these units are not given in Table 8.3-1. This is based on: (1) the lateral flow that may occur in these units, (2) they have a more complex mineral assemblage (zeolites, glass, and clays) which has a less well-constrained effect on calcite reactions, and (3) we are primarily interested in calcite deposition within the TSw unit, where the potential repository is located (TSw4 and TSw5 model layers in Table 8.3-1). The exclusion of the underlying hydrogeological units does not affect the results in the TSw unit because flow is predominantly gravity driven, and upward chemical diffusion is subordinate to downward advective transport.

Figure 1.3—1 **Schematic East-West cross-section through Yucca Mountain depicting the major hydrogeological units in the unsaturated zone and the approximate location of the potential repository horizon (Xu et al., 2001; Sonnenthal and Bodvarsson, 1999).**

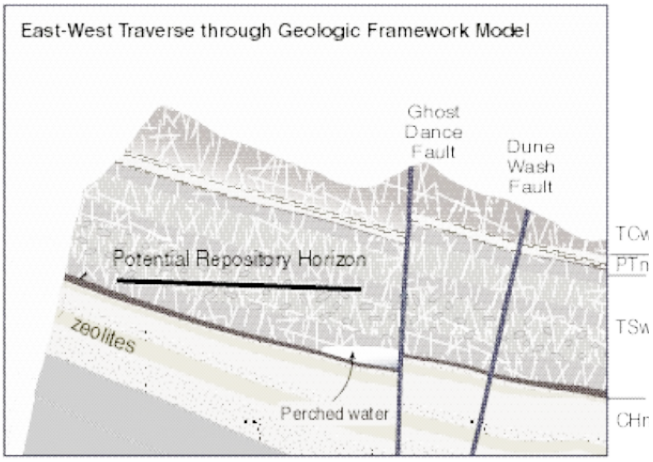

Table 1.3—1 **Hydrogeologic units, model layers, and hydrogeological properties for the Yucca Mountain Unsaturated Zone Flow and Transport Model as given by the property calibration model (Ahlers and Liu, 2000).**

Hydrogeologic unit	Description	Model layer	Fracture		Matrix	
			Permeability (m2)	Porosity	Permeability (m2)	Porosity
TCw: Tiva Canyon Welded unit	Moderately to densely welded portions	TCw1	2.41×10-12	3.7×10-2	3.86×10-15	0.253
		TCw2	1.00×10-10	2.6×10-2	2.74×10-19	0.082

	of the Tiva Canyon Tuff of the Paintbrush Group	TCw3	5.42×10-12	1.9×10-2	9.23×10-17	0.203
PTn: Paintbrush Nonwelded unit	Variably welded Paintbrush Tuff and its associated bedded tuffs, including those located at the bottom of the Tiva Canyon and top of the Topopah Spring Tuffs	PTn1	1.86×10-12	1.4×10-2	9.90×10-13	0.387
		PTn2	2.00×10-11	1.5×10-2	2.65×10-12	0.439
		PTn3	2.60×10-13	3.2×10-3	1.23×10-13	0.254
		PTn4	4.67×10-13	1.5×10-2	7.86×10-14	0.411
		PTn5	7.03×10-13	7.9×10-3	7.00×10-14	0.499
		PTn6	4.44×10-13	4.6×10-3	2.21×10-13	0.492
TSw: Topopah Spring welded unit	Moderately to densely welded portions of the Topopah Spring Tuff down to and including the densely welded basal vitrophyre	TSw1	3.21×10-11	7.1×10-3	6.32×10-17	0.053
		TSw2	3.56×10-11	1.2×10-2	5.83×10-16	0.157
		TSw3	3.86×10-11	8.4×10-3	3.08×10-17	0.154
		TSw4	1.70×10-11	1.0×10-2	4.07×10-18	0.110
		TSw5	4.51×10-11	1.5×10-2	3.04×10-17	0.131
		TSw6	7.01×10-11	2.0×10-2	5.71×10-18	0.112
		TSw7	7.01×10-11	2.0×10-2	4.49×10-18	0.094
		TSw8	5.92×10-13	1.6×10-2	4.53×10-18	0.037
		TSw9	4.57×10-13	5.9×10-3	5.46×10-17	0.173

A one-dimensional vertical column corresponding to the location of a deep borehole (WT-24) was chosen for modeling calcite deposition because measured calcite abundances (Paces et al., 2001) were available for comparison. The model grid, hydrogeological parameters and flow conditions were adopted from the hydrological property calibration work performed by Ahlers and Liu (2000).

Geochemical Model

Initial mineral abundances, potential secondary minerals, reactive surface areas, kinetic and thermodynamic data were taken from the modeling work of coupled thermal, hydrological, and chemical (THC) processes for the potential high-level nuclear waste repository at Yucca Mountain (Sonnenthal and Spycher, 2001; Spycher et al., 2003a). Minerals considered in the simulations are calcite, gypsum, goethite, tridymite, cristobalite-α, quartz, amorphous silica, hematite, fluorite, albite, K-feldspar, anorthite, Ca-smectite, Mg-smectite, Na-smectite, illite, kaolinite, opal-CT, stellerite, heulandite, mordenite, clinoptilolite, and volcanic glass. This full assemblage of minerals and the corresponding aqueous species are hereafter termed the extended-case geochemical system, because

it has more complexities and uncertainties in terms of thermodynamics and kinetics of mineral solid solutions (clays, zeolites and feldspars), effects on pH, and the partial pressure of CO_2. A simpler set of minerals and aqueous species (base-case geochemical system) disregards all aluminosilicates, Fe- and Mg-bearing minerals.

Calcite and gypsum dissolution and precipitation were assumed to take place under geochemical equilibrium, whereas dissolution and precipitation of the other minerals was treated under kinetic constraints. Initial mineral abundances were derived from X-ray diffraction measurements on cores and studies of fracture surfaces (Carey et al., 1998; S. Levy, unpublished data). Potential secondary minerals (i.e., those allowed to precipitate but which may not necessarily form) were determined from field and experimental observations of water-rock interaction and from equilibrium geochemical model calculations. Reactive surface areas of minerals on fracture walls were calculated from the fracture-matrix interface area/volume ratio, the fracture porosity, and the derived mineral volume fractions. These areas were based on the fracture densities, fracture porosities, and mean fracture diameter. Mineral surface areas in the rock matrix were calculated using the geometric area of a cubic array of truncated spheres that make up the framework of the rock and reductions to those areas owing to the presence of alteration phases such as clays and zeolites. Full details are given in Sonnenthal and Spycher (2001).

Initial pore water chemical concentrations were based on analyses of ultracentrifuged water (L. DeLoach, unpublished data) and chemical speciation calculations (Sonnenthal and Spycher, 2001; Spycher et al., 2003a). Except for perched water that lies well below the potential repository horizon, water has not been observed in fractures in the UZ. Therefore, the initial composition of water in the fractures was assumed to be the same as the matrix pore water (Table 8.3-2). The same water composition, re-equilibrated at the temperature of the top model boundary, was assumed for infiltrating water. Oxidizing conditions were considered for this water, because the fracture permeability of the rock is high and the system is unsaturated (air phase is everywhere present). The CO_2 gas partial pressures used for initial and top boundary conditions of the gas transport are in equilibrium with the corresponding aqueous chemical composition. An elevated gas partial pressure (relative to an atmospheric value of 0.344×10^{-3} bar) at the upper boundary can be attributed to soil-zone CO_2 production.

Table 1.3—2 **Water and gas chemistry used for initial and boundary conditions of the reaction-transport simulations (Sonnenthal and Spycher, 2001).**

Component	Concentration	Unit
Ca^{2+}	101	mg/L

Mg^{2+}	17	mg/L
Na^{+}	61.3	mg/L
K^{+}	8	mg/L
SiO_2 (aq)	70.5	mg/L
Al^{3+}	1.67×10^{-5}	mg/L
HCO_3^{-}	200	mg/L
Cl^{-}	117	mg/L
SO_4^{2-}	116	mg/L
F^{-}	0.86	mg/L
Fe^{3+}	6.46×10^{-8}	mg/L
pH	8.32 (at 25 ºC) 7.75 (at 17ºC)	
PCO_2	2.726×10^{-3} at 17 °C	bar

Simulation Setup

Simulations were performed using three infiltration rates, a base-case rate of 5.92 mm/yr (Ahlers and Liu, 2000), and bounding rates of 2 mm/yr and 20 mm/yr. The corresponding steady-state water flow conditions were used for geochemical transport simulations. Steady-state temperature distributions corresponding to the same three infiltration rates were obtained using a top temperature of 15.6ºC at the land surface and a bottom temperature of 28ºC at the water table (Figure 8.3-5). For the three infiltration rates, the same water and gas chemistry was used for the top boundary condition. The EOS3 flow module was used for these simulations.

For the reactive transport simulations of calcite precipitation, a simulation time of 10 million years was selected, based on the following inferences: (1) calcite growth has remained approximately constant over the past 8 million years, as indicated by radiocarbon, $^{230}Th/U$, and U-Pb ages (Paces et al., 1998) (2) the tuff is 12.7 million years old (Paces et al., 1998), and (3) all dated surfaces indicated by ages of outer mineral surfaces are young compared to the age of the tuffs. Infiltration rates and temperatures were held constant throughout the simulation, and therefore the results can only be considered to reflect the average conditions over this period of time.

In this manual, we only present results for a base-case infiltration rate of 5.92 mm/yr. More results are given in Xu et al. (2003a). The corresponding input and output files are provided with the distribution files. To shorten the run time for testing, the simulation time in the PARAM input block of flow.inp is specified as 3.15576E09 s (100 years). For a simulation of ten million years, users can reset this variable to 3.15576E13. Parts of output files for fluid flow, aqueous chemical concentrations, and changes of mineral abundances are given in Figures 8.3-2, 8.3-3 and 8.3-4.

Figure 1.3—2 Part of file flow.out for Problem 3 (calcite and infiltration).

```
Fua18(     1,  1) ST = 0.100000E+01 DT = 0.100000E+01 DX1= 0.000000E+00
```

```
Fua18(      2,   1) ST = 0.300000E+01 DT = 0.200000E+01 DX1= 0.000000E+00
Fua18(      3,   1) ST = 0.700000E+01 DT = 0.400000E+01 DX1= 0.000000E+00
Fua18(      4,   1) ST = 0.150000E+02 DT = 0.800000E+01 DX1= 0.000000E+00
Fua18(      5,   1) ST = 0.310000E+02 DT = 0.160000E+02 DX1= 0.000000E+00

----------------------------

          OUTPUT DATA AFTER (  1022,   1)-2-TIME STEPS

@@@@@@@@@@@@@@@@@@@@@@@@@@@@@@@@@@@@@@@@@@@@@@@@@@@@@@@@@@@@@@@@@@@@@@@@@@@@@@@@@@@
@

 TOTAL TIME     KCYC    ITER  ITERC    KON        DX1M         DX2M         DX3M
 0.31557E+10    1022       1   2088      2       0.00000E+00  0.00000E+00  0.00000E+00

@@@@@@@@@@@@@@@@@@@@@@@@@@@@@@@@@@@@@@@@@@@@@@@@@@@@@@@@@@@@@@@@@@@@@@@@@@@@@@@@@@@
@

ELEM.  INDEX      P           T           SG          SL        XAIRG       XAIRL
                 (PA)      (DEG-C)

Faa18      1 0.84256E+05 0.15750E+02 0.96625E+00 0.33752E-01 0.98668E+00 0.13256E-04
Maa18      2 0.84256E+05 0.15750E+02 0.70350E+00 0.29650E+00 0.98668E+00 0.13256E-04
Fba18      3 0.84581E+05 0.16021E+02 0.98275E+00 0.17250E-01 0.98650E+00 0.13304E-04
Mba18      4 0.84581E+05 0.16021E+02 0.61598E-02 0.99384E+00 0.98650E+00 0.13304E-04
Fca18      5 0.84842E+05 0.16287E+02 0.96976E+00 0.30242E-01 0.98631E+00 0.13340E-04
```

Figure 1.3—3 Part of file YMC_conc.dat for Problem 3 after t = 100 yr (SL is water saturation, T is temperature in °C, unit of concentrations is mol/l).

```
    Z           Sl         pH      t_ca+2       t_na+      t_cl-      t_sio2(aq)

 1482.000  0.3375E-01  8.2121  0.2231E-02  0.2666E-02  0.3304E-02  0.1233E-02
 1482.000  0.2965E+00  8.2128  0.2230E-02  0.2666E-02  0.3303E-02  0.1236E-02
 1449.000  0.1725E-01  8.1370  0.2385E-02  0.2667E-02  0.3301E-02  0.1403E-02
 1449.000  0.9938E+00  8.1380  0.2383E-02  0.2667E-02  0.3301E-02  0.1403E-02
 1422.000  0.3024E-01  8.1124  0.2402E-02  0.2667E-02  0.3301E-02  0.1293E-02
 1422.000  0.8104E+00  8.1124  0.2402E-02  0.2667E-02  0.3301E-02  0.1293E-02
 1413.000  0.4217E-01  8.1098  0.2405E-02  0.2667E-02  0.3301E-02  0.1197E-02
 1413.000  0.8338E+00  8.1097  0.2405E-02  0.2667E-02  0.3301E-02  0.1195E-02
 1404.000  0.2536E-01  8.1056  0.2392E-02  0.2667E-02  0.3301E-02  0.1182E-02
 1404.000  0.3328E+00  8.1056  0.2392E-02  0.2667E-02  0.3301E-02  0.1182E-02
 1396.000  0.3065E-01  8.1058  0.2395E-02  0.2667E-02  0.3301E-02  0.1186E-02
 1396.000  0.6580E+00  8.1057  0.2395E-02  0.2667E-02  0.3301E-02  0.1186E-02
 1370.000  0.2463E-01  8.1038  0.2398E-02  0.2667E-02  0.3300E-02  0.1182E-02
 1370.000  0.6159E+00  8.1037  0.2398E-02  0.2667E-02  0.3300E-02  0.1182E-02
 1344.000  0.2052E-01  8.1000  0.2390E-02  0.2666E-02  0.3300E-02  0.1181E-02
 1344.000  0.4469E+00  8.1000  0.2390E-02  0.2666E-02  0.3300E-02  0.1181E-02
```

Figure 1.3—4 Part of file YMC_min.dat for Problem 3 after t = 100 yr, giving changes in mineral abundances (in volume fraction, positive values indicate precipitation and negative dissolution).

```
Z      Porosity   calcite   ,glass        fluorite

 1482.000  0.99000  0.5215E-05  -0.6937E-11  0.0000E+00
 1482.000  0.25300  0.9256E-06  -0.1586E-06  0.0000E+00
 1449.000  0.99000  0.2815E-06  -0.2587E-11  0.0000E+00
 1449.000  0.08200  0.3220E-06  -0.5846E-06  0.0000E+00
 1422.000  0.99000  0.2767E-06  -0.6266E-11  0.0000E+00
 1422.000  0.20300  0.6945E-06  -0.4830E-06  0.0000E+00
 1413.000  0.99000  0.3649E-06  -0.2132E-10  0.0000E+00
 1413.000  0.38700  0.1355E-05  -0.5392E-07  0.0000E+00
```

```
1404.000   0.99000   0.2389E-06   -0.1301E-10   0.0000E+00
1404.000   0.43900   0.7408E-06   -0.2203E-07   0.0000E+00
1396.000   0.99000   0.2989E-06   -0.3547E-10   0.0000E+00
1396.000   0.25400   0.7384E-06   -0.6207E-07   0.0000E+00
1370.000   0.99000   0.2449E-06   -0.1265E-10   0.0000E+00
1370.000   0.41100   0.1133E-05   -0.5461E-07   0.0000E+00
1344.000   0.99000   0.2172E-06   -0.1451E-10   0.0000E+00
1344.000   0.49900   0.1084E-05   -0.4607E-07   0.0000E+00
```

Figure 1.3—5 **Modeled temperature profiles in borehole WT-24 as a function of depth for three infiltration rates.**

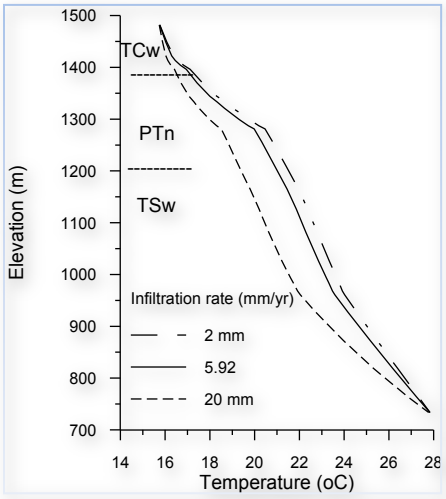

1.3.4 Results and discussion

The simulated total (fracture plus matrix) calcite abundances in the WT-24 column for three infiltration rates, together with USGS measured data, are presented in Figure 8.3-6. In general, the results obtained using the base-case infiltration rate (5.92 mm/yr) agree more closely with the measured WT-24 calcite abundances than those obtained using the other infiltration rates, especially for the PTn unit.

Figure 1.3—6 **Simulated total (fracture plus matrix) calcite abundances (volume fraction) in the WT-24 column for different infiltration rates after 10 million years (Extended geochemical system). Diamonds represent bulk rock calcite abundances measured by the U.S. Geological Survey (Paces et al., 2001).**

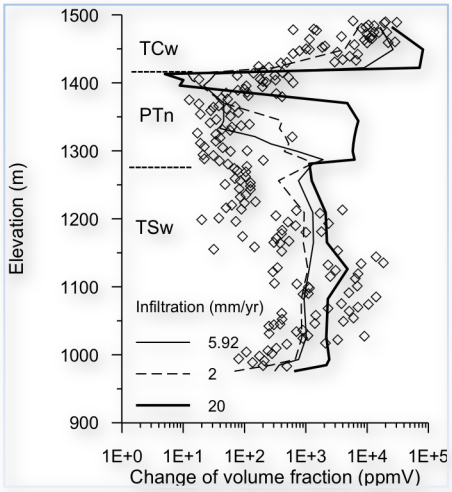

The simulated calcite abundances in the basal PTn layer for the three infiltration simulations are higher than those measured in WT-24. This is a result of an increase in the temperature gradient (Figure 8.3-5) resulting in a concomitant decrease in calcite solubility. Relatively greater calcite abundances in the bottom layer of the PTn have been observed at other locations such as in another deep borehole USW G-2 (Carey et al., 1998). The lower measured calcite abundances may also be a result of lateral flow that is not captured in the one-dimensional simulations.

Results for the welded TSw unit (a potential repository host rock unit) generally fall in the wide range of measured calcite data. Calcite abundances obtained using the highest infiltration rate (20 mm/yr) are closer to the high bound of measured values. Those values from the base-case (5.92 mm/yr) fall in the middle of the TSw measured data range. This may imply that 20 mm/yr is the high bound for the infiltration rate at the WT-24 location; whereas the base-case infiltration (5.92 mm/yr) from the flow property calibration (used for the flow model) may be close to the long-term mean infiltration rate for this location. More results are presented in Xu et al. (2003a).

1.4 Problem 4 – Bentonite Alteration due to Thermo-Hydro-Chemical (THC) Processes during the Early Thermal Period in a Nuclear Waste Repository (EOS4)

1.4.1 Problem statement

Simulating coupled thermal-hydrological-chemical (THC) processes in the backfill material and near-field environment of a heat-generating nuclear waste repository requires site-specific and detailed information to assess the coupled processes and their impact at any particular site, and to develop engineering designs. Before moving into site-specific investigations, we explore general

features and issues representing characteristics that are common and essential for many such systems.

The present study is not related to any particular site. However, the geometric configuration and the hydraulic parameters and mineralogical composition of the clayey formation are abstracted from a nuclear waste repository concept considered in Switzerland (NAGRA, 2002). The reference design for canisters to be stored in a repository for spent fuel and high-level waste (SF/HLW) involves a cast steel canister with about 20 cm wall thickness. The canisters are about 1 m in diameter and are surrounded by a 0.75-m thick bentonite buffer in emplacement tunnels which are 2.5 m in diameter (Figure 8.4-1). The repository tunnel is assumed to be in the water-saturated zone at a depth of 650 m below the land surface in the host rock which is referred to as the Opalinus Clay.

The swelling process of bentonite and clay is not considered in this paper. The impact of clay swelling on porosity and related flow and transport properties could be important. No redox reactions are considered in the simulations. While the system evolves from an oxidizing to a reducing environment, we concentrate our modeling analyses on the early period of heat loading and water resaturation, when oxidizing conditions are expected to prevail. The problem has been presented in Xu et al. (2011).

1.4.2 Problem Setup

Thermal and hydrological conditions

The present study employed a simplified model, which was previously used by Senger et al. (2008) and Xu et al. (2008). The model is represented by a radially symmetric geometry, ignoring the lateral no-flow boundary and gravity effects (Figure 8.4-1). The repository is located 650 m below the land surface. The Opalinus clay host rock is assumed to be initially fully water-saturated with a background pressure of 65 bar. The outer boundary at a radial distance of 75 m was set at a constant pressure of 65 bar and a constant temperature of 38°C.

Figure 1.4—1 **Radially symmetric model, representing a single waste canister, canister hull, bentonite backfill, and the Opalinus clay host rock.**

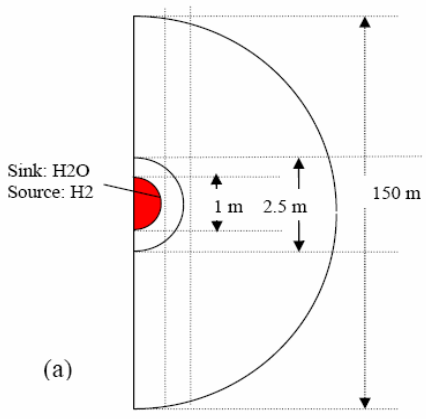

The thermo-physical properties for bentonite buffer and Opalinus clay are summarized in Table 8.4-1. The van Genuchten model (van Genuchten, 1980; Mualem, 1976) is used to describe the functional relationships between relative permeability and saturation, and capillary pressure and saturation for the different materials. The parameters were taken from Xu et al. (2008) and Senger and Ewing (2008). Senger and Ewing reported simulation results for a 3-D model of the thermo-hydrologic conditions in the vicinity of a backfilled SF emplacement tunnel. They quantified the coupled thermo-hydrologic evolution of temperature, saturation, and pressure to determine potential non-uniform resaturation of the bentonite buffer or potential localized accumulation of pore water in contact with the waste canister.

Table 1.4—1 Thermo-physical parameters for bentonite and Opalinus clay in the THC model.

	Bentonite	Opalinus Clay
Porosity ϕ [-]	0.475	0.14
Permeability k [m^2]	1×10^{-19}	1×10^{-20}
Pore compressibility (c_r) [Pa^{-1}]	3.58×10^{-9}	1.83×10^{-9}
Rock grain density ρ_R (kg/m^3)	2700	2670
Rock specific heat C_R (J/kg/^{o}C)	964	946.5
Thermal conductivity λ (W/m/^{o}C)	1.35	2.5
Two-Phase Constitutive Model	van Genuchten	van Genuchten
Residual liquid saturation S_{lr} [-]	0.3	0.5
Residual gas saturation S_{gr} [-]	0.02	0.02
van Genuchten parameter n [-]	1.82	1.67
Capillary strength pressure $1/\alpha$ [Pa]	1.8×10^7	1.8×10^7

A variable temperature inner boundary, representing heat generation due to decay from the waste package, was developed using successive fixed heat capacity at the canister grid block. This

heat boundary was specified such that a rough correspondence was obtained to the temperatures at the canister surface computed in the simulation of Senger and Ewing (2008). The temperature was set initially at 150°C at this grid block, and allowed to decrease through conductive heat transport into the bentonite buffer and surrounding host rock. The temperatures decreased from the initial 150°C to about 55°C after 1,000 years (Figure 8.4-2). An initial temperature of 38°C was used for the remaining grid blocks of the model domain.

Figure 1.4—2 Temperature evolution at the canister surface

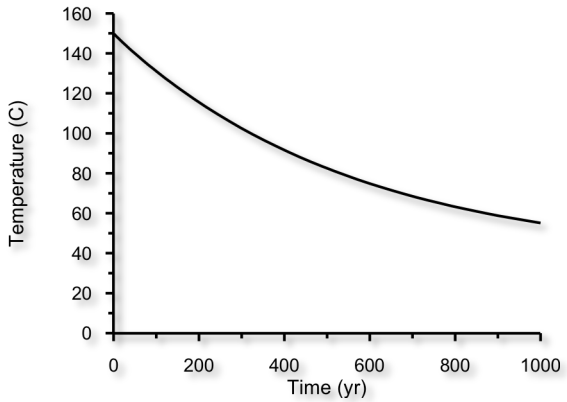

Geochemical conditions

The initial mineral composition of bentonite and Opalinus clay used in the present modeling is given in Table 8.4-2. The MX-80 type of bentonite is used for the buffer materials, containing 75% montmorillonite-Na, which is the dominant mineral. The mineral content of Opalinus clay was assigned based on that given in JNC (2000). Two initial water chemical compositions were used: (1) a dilute water composition, and (2) a composition measured for the BWS-A6 water extracted from the host rock (Fernández et al., 2006). Prior to simulating reactive transport, batch geochemical modeling of water-rock interaction for the two materials was conducted, equilibrating the initial water with the primary minerals listed in Table 8.4-2 at a temperature of 38°C. A reasonably short simulation time of 10 years is needed to obtain nearly steady-state aqueous solution compositions, which were then used as initial chemical conditions for reactive transport (THC) simulations.

Table 1.4—2 Initial mineral volume fractions and possible secondary mineral phases.

Mineral	Volume percent in term of solid	
	Bentonite	**Opalinus clay**
Calcite	1.4	15.0
Quartz	15.1	18.0
Kaolinite	1.0	10.0

Illite		20.0
K-feldspar	6.5	3.0
Montmorillonite-Na	75	10.0
Montmorillonite-Ca		10.0
Chlorite		10.0
Dolomite		1.0
Siderite		3.0
Ankerite		1.0
Annite	1.0	
Anhydrite		
Amorphous silica		

Kinetic parameters

Reactive chemical-transport modeling requires not only a conceptual understanding of the mechanisms involved in the nucleation, precipitation, and dissolution of the suite of participating minerals, but also quantitative estimates of relevant kinetic parameters. In this work, a general form of rate expression was used, which is based on transition state theory (TST; Lasaga, 1998).

The kinetic rate of mineraldissolution and precipitation includes a product of the rate constant and reactive surface area as represented by Eq. B.6 in Appendix B. The parameters used for the kinetic rate expression are given in Table 8.4-3. Calcite and anhydrite are assumed to react rapidly (relative to the time frame being modeled), and thus an equilibrium model can be used. In Table 8.4-3, we include separate rate constants (k^{25}), activation energies (E), and reaction order (n) for processes catalyzed by H^+ or OH^-. At any pH, the total rate is the sum of the rates from all three mechanisms. Catalysis by H^+ or OH^- is considered only for mineral dissolution. Parameters for the rate law were taken from Palandri and Kharaka (2004), who compiled and fitted experimental data reported by many investigators. Parameters for montmorillonite were set to those of smectite.

If the aqueous phase supersaturates with respect to a potential secondary mineral, a small volume faction of 1×10^{-6} is used for calculating the seed surface area for the new phase to grow. The precipitation of secondary minerals is represented using the same kinetic expression as that for dissolution. However, because precipitation rate data for most minerals are unavailable, only the neutral mechanism with parameters given in Table 8.4-3 were employed to describe precipitation. Multiple kinetic precipitation mechanisms can be specified in an input file of the TOUGHREACT program, should such information become available.

Mineral reactive-surface areas (the second column of Table 8.4-3) are based on the work of Sonnenthal et al. (2005) and Mukhopadhyay et al. (2009), and were calculated assuming that the

rock framework consists of a cubic array of truncated spheres. The larger surface areas for clay minerals are due to smaller grain sizes.

Table 1.4—3 **Parameters for calculating kinetic rate constants of minerals. Note that (1) all rate constants are listed for dissolution except opal-A; (2) *A* is specific surface area, k^{25} is kinetic constant at 25°C, *E* is activation energy, and *n* is the power term (Eq. B.12 in Appendix B); (3) the power terms *n* for both acid and base mechanisms are with respect to H^+.**

Mineral	A (cm²/g)	Parameters for kinetic rate law								
		Neutral mechanism		Acid mechanism			Base mechanism		
		k^{25} (mol/m²/s)	E (KJ/mol)	k^{25}	E	n (H^+)	k^{25}	E	n (H^+)
Calcite	Equilibrium								
Quartz	98	1.023 ×10⁻¹⁴	87.7						
Kaolinite	15 16	6.918 ×10⁻¹⁴	22.2	4.898 ×10⁻¹²	65.9	0.777	8.913 ×10⁻¹⁸	17.9	-0.472
Illite	15 16	1.660 ×10⁻¹³	35	1.047 ×10⁻¹¹	23.6	0.34	3.020 ×10⁻¹⁷	58.9	-0.4
K-feldspar	98	3.890 ×10⁻¹³	38	8.710 ×10⁻¹¹	51.7	0.5	6.310 ×10⁻¹²	94.1	-0.823
Montmorillonite-Na	15 16	1.660 ×10⁻¹³	35	1.047 ×10⁻¹¹	23.6	0.34	3.020 ×10⁻¹⁷	58.9	-0.4
Montmorillonite-Ca	15 16	1.660 ×10⁻¹³	35	1.047 ×10⁻¹¹	23.6	0.34	3.020 ×10⁻¹⁷	58.9	-0.4
Chlorite	15 16	3.02× 10⁻¹³	88	7.762 ×10⁻¹²	88	0.5			
Dolomite	98	2.951 ×10⁻⁸	52.2	6.457 ×10⁻⁴	36.1	0.5			
Siderite	98	1.260 ×10⁻⁹	62.76	6.457 ×10⁻⁴	36.1	0.5			
Ankerite	98	1.260 ×10⁻⁹	62.76	6.457 ×10⁻⁴	36.1	0.5			
Annite	98	2.818 ×10⁻¹⁴	22.0	1.413 ×10⁻¹²	22.0	0.37	2.818 ×10⁻¹⁵	22.0	-0.22
Anhydrite	Equilibrium								
Amorphous silica	98	3.000×10⁻¹⁰	49.8						

Simulations

Four simulations were performed. The first, base-case simulation used parameters given in Tables 8.4-1, 8.4.2, and 8.4.3. Mineral dissolution and precipitation rates are a product of the kinetic rate constant and reactive surface area, the magnitudes of which are highly uncertain and cover a wide range of values. Therefore, two sensitivity simulations (Simulations 2 and 3) were performed

by decreasing and increasing the surface area by one order of magnitude from the base-case value. Simulation 4 includes cation exchange from the base-case.

The EOS4 fluid property module was used to calculate the thermo-physical properties of the fluid mixture. In the EOS4 module, provision is made for vapor pressure lowering effects (see Pruess et al., 1999). Vapor pressure is expressed by Kelvin's equation, which is a function not only of temperature, but depends also on capillary pressure, which in turn is a function of saturation. Only the base-case simulation is presented here. The input and major output files are provided with the distribution files.

1.4.3 Results

After closure of an underground nuclear waste repository, the decay of radionuclides elevates temperature, and the bentonite buffer resaturates through water flow from the surrounding host rock. The perturbations from these thermal and resaturation processes induce mineral dissolution and precipitation. Consequently, the porosity of the bentonite buffer is changed. The simulated porosity distribution at different times for different cases is presented in Figure 8.4-3. For the first three cases without cation exchange, porosity decreases from the initial value of 0.475, indicating that precipitation dominates. Changes in porosity are larger close to the interface between the bentonite buffer and Opalinus Clay host rock, because resaturation processes carry chemical constituents from the host rock. Decreases in porosity are smaller close to the canister surface. Decreases in reactive surface area (rate) result in reductions in mineral alteration and porosity change (compare Figure 8.4-3b to 8.4-3a). Conversely, increases in reactive surface area cause increases in mineral alteration and porosity change (compare Figure 8.4-3c with 8.4-3a). Considering cation exchange (Figure 8.4-3d), porosity mostly increases, but slightly decreases close to the interface with the host rock; it does not change close to the canister surface. Overall, no significant changes in porosity occur during the first 1,000 years of thermal and resaturation processes.

Figure 1.4—3 **Distribution of porosity in bentonite buffer: (a) base case, (b) reactive surface area decreased by one order of magnitude, (c) reactive surface area increased by one order of magnitude, and (d) including cation exchange.**

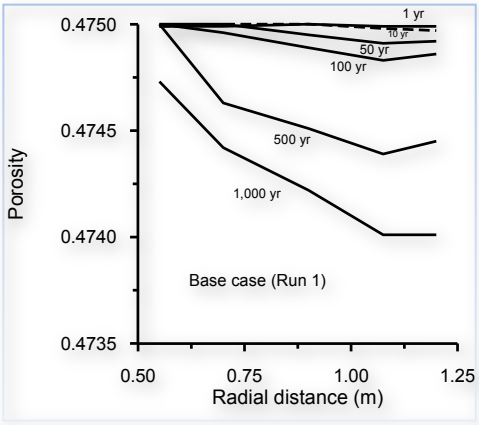

(a)

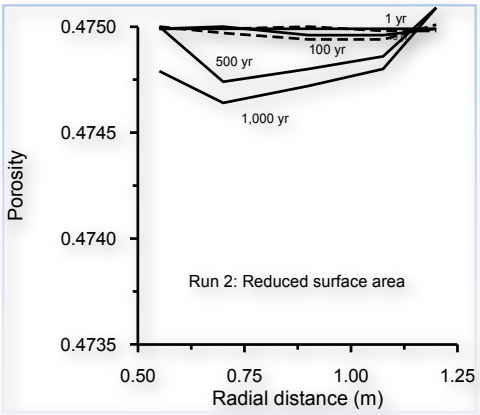

(b

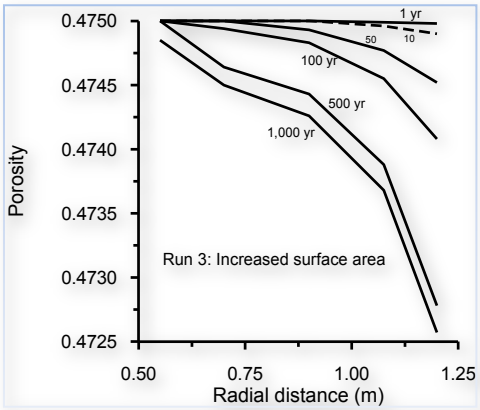

(c)

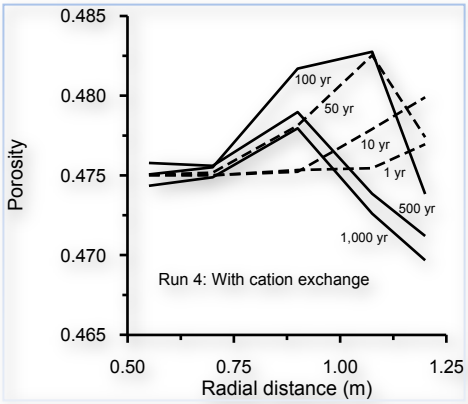

(d)

Montmorillonite-Na, the dominant mineral (with an initial volume fraction of 75%), dissolves in all four cases (Figure 8.4-4a). Decreases in reactive surface area (rate) results in reductions in montmorillonite-Na dissolution. Conversely, increases in reactive surface area cause increases in its dissolution. Considering cation exchange results in a reduction in Montmorillonite-Na dissolution. The pattern of annite dissolution is similar to that of montmorillonite-Na (Figure 8.4-4b). Calcite precipitates in most parts of the bentonite because its solubility decreases with temperature, but it dissolves close to the interface with the host rock supplying reactants for its precipitation close to the hot end of the canister surface (Figure 8.4-4c). Calcite dissolution and precipitation is not sensitive to changes in surface area. K-feldspar precipitation occurs over the entire radial distance, with more precipitation close to the interface with the host rock (Figure 8.4-4d). K-feldspar precipitation is proportional to changes in surface area. With cation exchange, less K-feldspar precipitates. Similar to K-feldspar, kaolinite precipitates over the entire thickness of the bentonite buffer, with more precipitation close to the interface with the host rock (Figure 8.4-4e). The pattern of chlorite precipitation is the same as kaolinite (Figure 8.4-4f).

Figure 1.4—4 Change in volume fraction of montmorillonite-Na in bentonite buffer obtained for the base case.

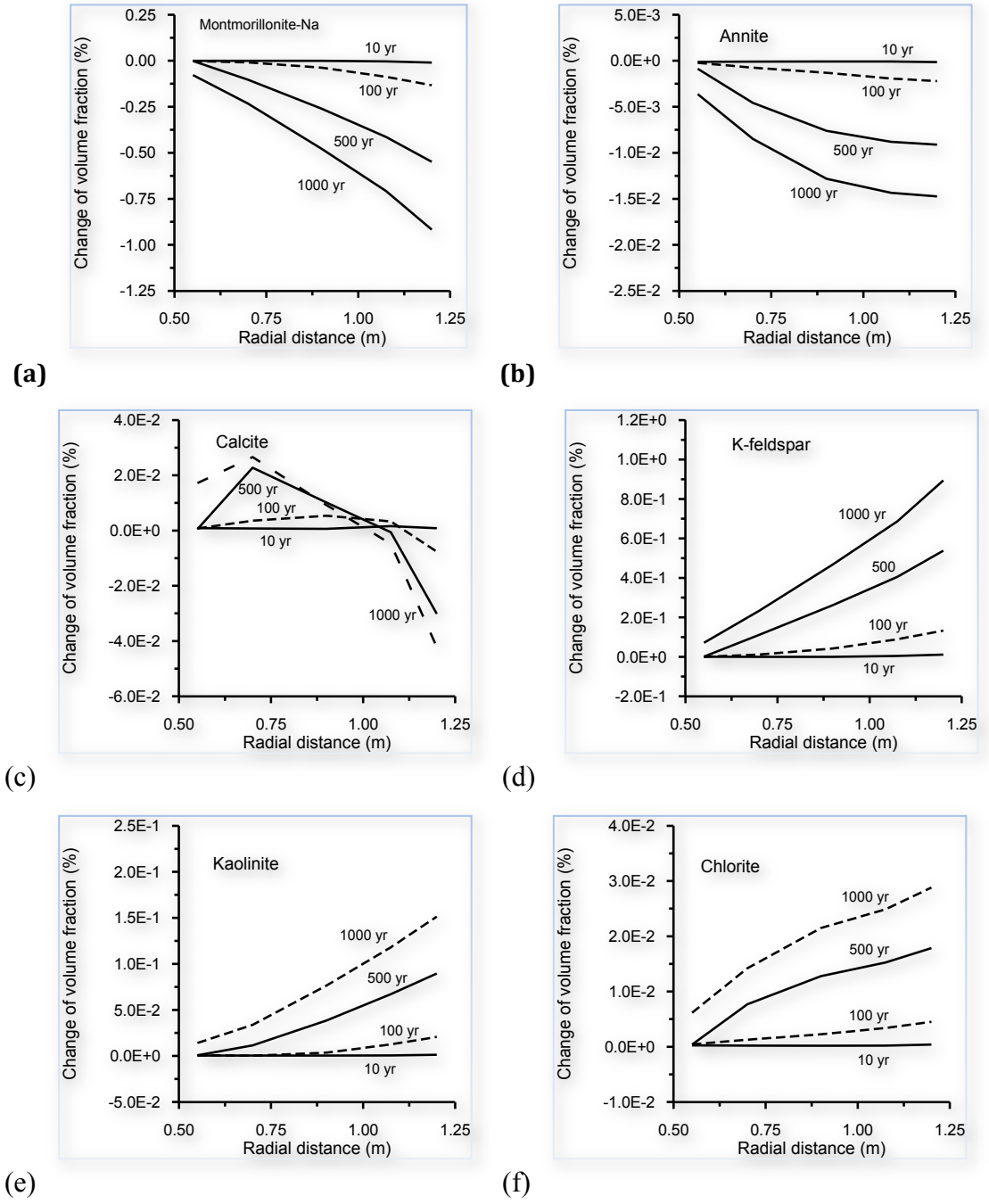

1.4.4 Summary

A 1D radially symmetric model of a SF waste canister emplaced with bentonite buffer in a deep underground repository in the Opalinus clay has been developed, representing the essential general features and issues related to a nuclear waste repository. Using this model, mineral alteration and changes in porosity for the early thermal and resaturation processes in a waste repository for SF waste canisters were examined for different cases. The following conclusions can be drawn from the modeling analyses:

The perturbations from these thermal and hydrological processes result in a decrease in porosity for cases without considering cation exchange, indicating precipitation dominates. Even though montmorillonite-Na with an initial volume fraction of 75% of the bentonite, dissolves for all simulation cases, the slight decrease in porosity is due to precipitation of K-feldspar, kaolonite, and chlorite. Decreases in porosity in the bentonite are larger close to the interface with the Opalinus clay host rock because resaturation processes carry chemical constituents from the host rock into the bentonite. Mineral alteration and changes in porosity are sensitive to reactive surface area, which strongly affects the kinetic reaction rates. Cation exchange indirectly affects mineral alteration, and thus has a second-order impact on porosity changes. Overall, mineral alteration and associated changes in porosity during the 1,000 year period of thermal and hydrological processes are relatively small and are expected to not significantly affect flow and transport properties.

The preliminary modeling presented here is for a simplified geometric configuration and abstracted hydraulic parameters and mineralogy of the clayey formation. However, this modeling and the sensitivity analyses were useful in identifying the role of some physical and chemical parameters in the alteration of the bentonite buffer materials. The developed model may provide a useful tool for gaining a better understanding of the coupled chemical and physical processes, as well as the controlling conditions and relevant parameters, for a site-specific repository system.

1.5 Problem 5 – 1-D Radial Model for CO_2 Sequestration in a Deep Saline Formation (ECO2N)

1.5.1 Problem statement

The feasibility of storing CO_2 in deep geologic formations has been discussed in the technical literature over the last decade. Studies include an evaluation of the feasibility of CO_2 aquifer storage in The Netherlands (Lohuis, 1993) and in the Alberta Basin, Canada (Gunter et al., 1993; Bachu et al., 1994; Law and Bachu 1996; Gunter et al., 1996 and 1997). Furthermore, large-scale CO_2 disposal in an aquifer is already being practiced in the Norwegian sector of the North Sea (Korbol and Kaddour, 1995).

Carbon dioxide is retained in geologic formations in three ways (Hitchon, 1996). First, CO_2 can be trapped as a gas or supercritical fluid under a low-permeability caprock. This process, commonly called hydrodynamic trapping, will likely be, in the short term, the most important mechanism of retention. Second, CO_2 can dissolve into the groundwater, referred to as a solubility trapping. The dissolution of CO_2 in groundwater increases the acidity of water and affects the solubilities of minerals composing the host rock matrix. Third, CO_2 can react directly or indirectly with minerals and organic matter in the geologic formation leading to the precipitation of secondary carbonates. The latter process, so-called "mineral trapping", is attractive because it could immobilize CO_2 for long time scales, and prevent its easy return to the atmosphere. The interaction of CO_2 with alkaline aluminosilicate minerals will also result in the formation of dissolved alkali carbonates and bicarbonates, thereby enhancing "solubility trapping".

Numerical modeling of geochemical processes is a necessary tool for investigating the long-term consequences of CO_2 disposal in deep formations, because alteration of the predominant host rock aluminosilicate minerals is very slow and is not experimentally accessible under ambient deep-aquifer conditions. Johnson et al. (2001) simulated CO_2 injection at Statoil's North-Sea Sleipner facility and analyzed the coupled process mechanisms that lead to hydrodynamic, solubility, and mineral trapping, as well as the relative effectiveness of the distinct sequestration processes as a function of key reservoir properties. McPherson and Lichtner (2001) used a sedimentary basin model, including multiphase flow of CO_2, groundwater, and brine, to evaluate resident times in possible aquifer storage sites and migration patterns and rates away from such sites in the Powder River Basin of Wyoming. Xu et al. (2004a) performed batch geochemical modeling for three different formation mineralogies in the presence of CO_2 at high pressure. The modeling included (1) redox processes that could be important in deep subsurface environments, (2) the presence of organic matter, (3) the kinetics of chemical interactions between the host rock minerals and the aqueous phase, and (4) CO_2 solubility dependence on pressure, temperature and salinity of the system (see Eq. B.14 through B.17 in Appendix B).

During large-scale injection of CO_2 into deep formations, geochemical processes are strongly affected by physical processes such as multiphase fluid flow and solute transport. Fluid pressures will rise as CO_2 displaces formation water in which it partly dissolves. The dissolution of primary and precipitation of secondary minerals change formation porosity and permeability, and could alter fluid flow patterns. All coupled hydrologic and chemical processes affect the feasibility of CO_2 injection and storage in deep formations. Uncoupled batch geochemical modeling and flow simulation are inadequate to describe the complex subsurface physical and chemical interactions expected to occur. A systematic process-based understanding of the coupled physical and chemical phenomena is required.

1.5.2 Definition of test problem

The response of deep formations to CO_2 injection will depend on many factors, including formation permeability and porosity, the presence of heterogeneities such as faults and layers of high or low permeability, the physical and chemical characteristics of the brines, and the nature of the mineral phases that are present. A great deal of specific and detailed information will be required to assess the feasibility of disposing of CO_2 in a brine formation at any particular site, and to develop engineering designs for CO_2 disposal systems. A basic issue in geologic disposal of CO_2 is the physical and chemical behavior in the vicinity of a CO_2 injection well. Previous numerical studies have investigated simple models of one- and two-dimensional radial flow to examine the displacement of formation waters by injected CO_2 (Pruess and Garcia, 2002; Pruess et al., 2005). These studies have provided initial insight into issues regarding volumetric sweep, CO_2 storage capacity, and pressurization processes that would arise from large-scale CO_2 injection. Exploratory studies of geochemical effects have also been conducted, using a zero-dimensional batch reaction approach to model the chemical reactions that would take place when different mineral assemblages are exposed to CO_2 at high pressures in the presence of brine (Perkins and Gunter, 1996; Gunter et al., 1997; Xu et al., 2004a). The present study combines the simple 1-D radial model previously investigated by Pruess et al. (2003) with the batch chemical reaction model of Xu et al. (2004a), to model the coupled processes of fluid flow and chemical reactions near a CO_2 injection well.

Geologic formation

The setup of the problem is similar to that of Xu et al. (2003b), except using the following (1) a porosity of 0.3 not 0.1, (2) a temperature of 75ºC (at about 2000 m depth) instead of 40ºC, (3) improved mineralogical composition, and kinetic rate law and parameters.

The geologic formation is assumed to be infinitely long and homogeneous with a thickness of 100 m, containing 1 M NaCl brine at a constant temperature of 75ºC. A 1-D radial model is used. This simplification does not consider non-uniform sweep that may occur due to formation heterogeneities, or due to buoyancy forces that would tend to drive CO_2 towards the top of the aquifer. Some justification for a 1-D approach can be derived from the slow rates and long time scales of geochemical changes, which will cause processes to play out over time that will make the distribution of CO_2 more uniform. Initially, injected CO_2 will tend to accumulate and spread out near the top of permeable intervals, partially dissolving in the aqueous phase. CO_2 dissolution causes the aqueous-phase density to increase by a few percent. This will give rise to buoyant convection where waters enriched in CO_2 will tend to migrate downward (Weir et al., 1995; Garcia, 2001). The process of CO_2 dissolution and subsequent aqueous phase convection will tend to mix aqueous CO_2 in the vertical direction. The time scale for significant convective mixing is likely to be slow (of the order of

hundreds of years or more; Ennis-King and Paterson, 2003), and may be roughly comparable to time scales for significant geochemical interactions of CO_2.

The well field is modeled as a circular region of 10,000 m radius, at the center of which CO_2 is injected uniformly at a constant rate of 90 kg/s. A 1-D radial grid was used with a spacing gradually increasing away from the well. The CO_2 injection was assumed to continue for a period of 10 years. The fluid flow and geochemical transport simulation was run for a period of 1,000 years.

Table 1.5—1 Hydrogeologic parameters for Problem 5.

Aquifer thickness	**100 m**
Permeability	10-13 m2
Porosity	0.30
Compressibility	4.5×10-10 Pa-1
Temperature	75 0C
Pressure	200 bar
Salinity	0.06 (mass fraction)
CO_2 injection rate	90 kg/s
Relative permeability	
Liquid (van Genuchten, 1980): $k_{rl} = \sqrt{S^*}\left\{1-\left(1-\left[S^*\right]^{1/m}\right)^m\right\}^2$ **irreducible water saturation** **exponent**	$S^* = (S_l - S_{lr})/(1 - S_{lr})$ $S_{lr} = 0.30$ $m = 0.457$
Gas (Corey, 1954):	
$k_{rg} = (1-\hat{S})^2(1-\hat{S}^2)$ **irreducible gas saturation**	$\hat{S} = \frac{(S_l - S_{lr})}{(S_l - S_{lr} - S_{gr})}$ $S_{gr} = 0.05$
Capillary pressure	
van Genuchten (1980) $P_{cap} = -P_0\left(\left[S^*\right]^{-1/m} - 1\right)^{1-m}$ **irreducible water saturation** **exponent** **strength coefficient**	$S^* = (S_l - S_{lr})/(1 - S_{lr})$ $S_{lr} = 0.00$ $m = 0.457$ $P_0 = 19.61\,kPa$

Geochemical system

A proxy for sediment from the United States Gulf Coast, modified from that originally presented by Apps (1996), was used for the reactive geochemical transport simulations. The mineralogy is similar to that commonly encountered in sedimentary basins. Apps (1996) presented a batch geochemical simulation of the evolution of Gulf Coast sediments as a basis for interpreting the chemical processes relating to the deep injection disposal of hazardous and industrial wastes.

The initial mineral abundances are shown in Table 8.5-2. The specification of formation mineralogy is determined in part by the availability of data. Most studies related to the Tertiary Gulf Coast sediments are concentrated in the state of Texas. The principal reservoir-quality sandstones within that region are respectively, the Frio, the Vicksberg and the Wilcox formations, all of which are found within the lower Tertiary. Of the three formations, the Frio was chosen as a representative candidate for the sequestration of supercritical carbon dioxide. It is the shallowest of the three formations, but over much of its areal extent, it is located at depths between 5,000 and 20,000 ft, depths sufficient to ensure adequate CO_2 densities for effective storage.

Calcite was assumed to react with aqueous species at local equilibrium because its reaction rate is typically quite rapid. Dissolution and precipitation of other minerals are kinetically-controlled. Kinetic rates are a product of the rate constant and reactive surface area (Eq. B.5 in Appendix B). Multiple mechanisms (including neutral, acid and base) are used for dissolution of minerals (Eqs. B.11 and B.12 in Appendix B). Kinetic parameters: rate constant (k_{25}), the activation energy (E_a), and the power term (n) for each mechanism are listed in Table 8.5-2. At any pH the total rate is the sum of the rates via each mechanism. Most of these parameters were taken from Palandri and Kharaka (2004) who compiled and fitted many experimental data reported by a large number of investigators. Parameters for illite were set to those of smectite. Acid pH parameters for siderite, ankerite, and dawsonite were set to those of dolomite. Neutral pH parameters for siderite were taken from Steefel (2001). Neutral pH parameters for ankerite and dawsonite are set to those of siderite.

Precipitation rate data do not exist for most minerals. Several aspects regarding precipitation are different from dissolution, including nucleation, crystal growth and Ostwald ripening processes, as well as the calculation of the reactive surface area (Steefel and van Capellen, 1990). These processes for mineral precipitation are not considered. Parameters for neutral pH in Table 8.5-2 were used for precipitation of the corresponding minerals. Notice that different sets of parameters for precipitation can be specified in the chemical input file of TOUGHREACT code.

The evolution of surface area in natural geologic media is complex, especially for multi-mineralic systems, and is not quantitatively understood at present. Mineral reactive surface areas (the third column of Table 8.5-2) were taken from Sonnenthal and Spycher (2001), which were calculated using a cubic array of truncated spheres that make up the framework of the rock. For clay

minerals kaolinite, illite, and smectite, increased surface areas were based on the smaller grain sizes of these sheet silicate minerals (Nagy, 1995). A reactive surface area calculated from grain size may be a poor estimate of the hydrologically accessible mineral surface area. To account for this effect, surface areas listed in Table 8.5-2 were reduced by one order of magnitude in the present simulations. The magnitudes of surface areas are highly uncertain and cover a wide range of values. Sensitivity regarding the kinetic rate constants and reactive surface areas should be addressed in the future.

Prior to CO_2 injection, a simulation of water-rock interaction was performed to obtain a nearly equilibrated water chemistry using a pure 1.0 M solution of sodium chloride reacting with the primary minerals listed in Table 8.5-2 at a temperature of 75 °C. The resulting water chemistry was used for the initial condition of reactive geochemical transport simulations under CO_2 injection.

Table 1.5—2 **Initial mineral volume fractions, possible secondary mineral phases, and their kinetic properties. Note that: (1) all rate constants are listed for dissolution; (2) A is the reactive surface area (Eq. B.5 in Appendix B), k_{25} is the kinetic constant at 25 °C, E_a is activation energy, and n is the power (Eq. B.11); (3) the power terms n for both acid and base mechanisms are with respect to H^+, (4) for pyrite, the neutral mechanism has a n with respect to O_2(aq), the acid mechanism has two species involved: one n with respect to H^+ and another n with respect to Fe^{3+} (see Eq. B.12); (5) dolomite, Ca-smectite, and pyrite were included in the list of possible secondary mineral phases in the input but they were not formed during the simulation.**

Mineral	Vol.% Of solid	A (m^2/g)	Parameters for kinetic rate law								
			Neutral mechanism		**Acid mechanism**			**Base mechanism**		
			k_{25} (mol/m^2/s)	**E_a (KJ/mol)**	**k_{25}**	**E_a**	**n (H^+)**	**k_{25}**	**E_a**	**n (H^+)**
***Primary*:**										
Quartz	57.888	9.8	1.023×10^{-14}	87.7						
Kaolinite	2.015	15 1.6	6.918×10^{-14}	22.2	4.898×10^{-12}	65.9	0.777	8.813×10^{-18}	17.9	-0.472
Calcite	1.929	Assumed at equilibrium								
Illite	0.954	15 1.6	1.660×10^{-13}	35	1.047×10^{-11}	23.6	0.34	3.020×10^{-17}	58.8	-0.4
Oligoclase	19.795	9.8	1.445×10^{-13}	69.8	2.138×10^{-11}	65	0.457			
K-feldspar	8.179	9.8	3.890×10^{-13}	38	8.710×10^{-11}	51.7	0.5	6.310×10^{-22}	94.1	-0.823
Na-smectite	3.897	15 1.6	1.660×10^{-13}	35	1.047×10^{-11}	23.6	0.34	3.020×10^{-17}	58.8	-0.4

Chlorite	4.556	9.8	3.02×10^{-13}	88	7.762×10^{-12}	88	0.5			
Hematite	0.497	12.9	2.512×10^{-15}	66.2	4.074×10^{-10}	66.2	1			
Secondary:										
Magnesite		9.8	4.571×10^{-10}	23.5	4.169×10^{-7}	14.4	1			
Dolomite		9.8	2.951×10^{-8}	52.2	6.457×10^{-4}	36.1	0.5			
Low-albite		9.8	2.754×10^{-13}	69.8	6.918×10^{-11}	65	0.457	2.512×10^{-16}	71	-0.572
Siderite		9.8	1.260×10^{-9}	62.76	6.457×10^{-4}	36.1	0.5			
Ankerite		9.8	1.260×10^{-9}	62.76	6.457×10^{-4}	36.1	0.5			
Dawsonite		9.8	1.260×10^{-9}	62.76	6.457×10^{-4}	36.1	0.5			
Ca-smectite		15 1.6	1.660×10^{-13}	35	1.047×10^{-11}	23.6	0.34	3.020×10^{-17}	58.8	-0.4
Pyrite		12.9	$k_{25}=2.818\times10^{-5}$ E_a =56.9 $n(O_2(aq))$=0.5		$k_{25}=3.02\times10^{-8}$ E_a =56.9 $n(H^+)$=-0.5, $n(Fe^{3+})$=0.5					

A new fluid property module, ECO2N, was used for this CO_2 disposal problem. ECO2N is based on work by Spycher and Pruess (2005), and provides an accurate description of the thermophysical properties of mixtures of water and CO_2 under conditions typically encountered in saline aquifers of interest for CO_2 disposal (10 $^oC \leq T \leq$ 110 ^oC; $P \leq$ 600 bars). Details on this new fluid property module can be found in the ECO2N manual.

As mentioned above, the reactive transport simulation was performed for a time period of 1,000 years. To demonstrate the RESTART feature, we performed a series of two TOUGHREACT runs. The first run was performed for 10 years. The input and major output files for the first run are provided with the distribution files. For the continuation run (restart) to 1,000 yr, we create a new subdirectory ~/P5_ECO2N-1Dradial/restart, into which we copy the input files (flow.inp, solute.inp, chemical.inp, therakin10.dat), the CO_2 property file (CO_2TAB), and the files SAVE and savechem from the first run. File SAVE is renamed INCON, savechem is renamed inchem, and the following minor changes are made in flow.inp: delete the INCON input block, and change the final simulation time from 3.15576E08 (10 years) to 3.15576E10 (1,000 years) in the PARAM input block. Now we can perform the restart run. Major output files from the restart run are also in subdirectory: ~/ P5_ECO2N-1Dradial/restart. Changes in porosity and permeability are a result of mineral dissolution and precipitation, consumption of CO_2 due to formation of carbonate minerals, and consumption of H_2O due to hydration reactions affecting the multiphase fluid flow. For longer time simulation, these

feedback effects should be coupled. This option can be used by specifying kcpl = 1 (porosity and permeability coupling) and Ico2h2o = 2 (CO_2 and H_2O coupling) in input file solute.inp. However, if the coupling options are used, the convergence for solving flow equations could be slower.

An important feature for ECO2N module (and also EOS2) from other modules is that partial pressures of CO_2 gas are calculated from fluid flow calculations and then fed to geochemistry. In contrast, with the EOS3 and EOS4 modules, CO_2 is assumed to be a trace gas and transported with the bulk gas phase by advection and diffusion. With EOS9, CO_2 is also assumed to be a trace gas but is transported only by diffusion because the bulk gas phase is not considered. With the ECO2N (or EOS2), if the CO_2 partial pressure in block 'INITIAL gas ZONES' of chemical.inp (see the file chemical.inp in the distribution files) is greater than zero, this partial pressure is taken as the background partial pressure (regions not flooded with the injected CO_2). If this value is set to zero, no background CO_2 partial pressure buffer is allowed.

1.5.3 Results and discussion

Figure 8.5-1a shows CO_2 gas (supercritical fluid) saturations along the radial distance (water saturations are complementary to gas saturations, or $S_l = 1- S_g$). After 10 years, the region close to the well in about 40 m radial distance is completely dryout. The CO_2 plume (two-phase region) extends to a radial distance of 1,250 m. Later, the gas saturation gradually decreases due to formation of secondary carbonate minerals (see Figures 8.5-1 and 8.5-2). In the CO_2 plume region, pH is mainly buffered by CO_2 gas dissolution and calcite dissolution, values close to 5 are maintained as long as both CO_2 gas and calcite mineral are present. pH gradually increases with time due to mineral alteration. After 1,000 years, a value close to 6 was attained.

Figure 1.5—1 **Distributions of CO_2 gas saturation (a) and pH at different times for Problem 5 (in the region close to the well in about 160 m distance, water is completely removed).**

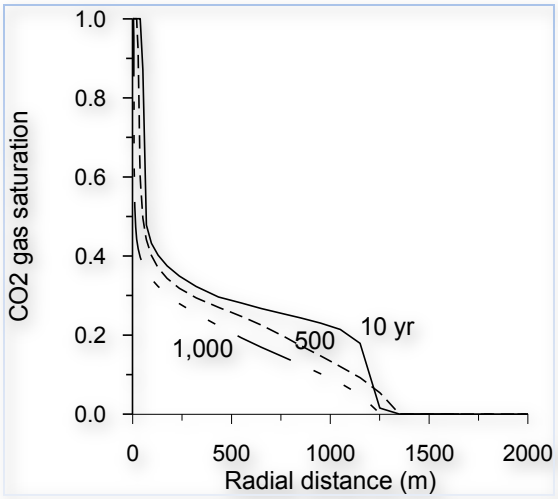

(a) CO_2 saturation

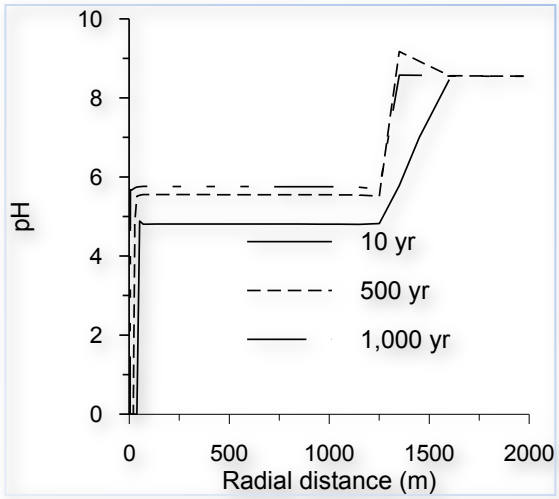

(b) pH

Significant ankerite precipitates due to CO_2 injection and dissolution of alumino-silicate minerals (Figure 8.5-2a). After 1,000 years, a maximum volume fraction of 0.02 (2%) formed at 1,250 m distance. Calcite dissolves rather than precipitates in the injected CO_2 plume region because a slightly low pH. Some dawsonite precipitates (Figure 8.5-2b) with a maximum volume fraction of 0.003 (0.3%). A small amount precipitation of magnesite and siderite occurs. No dolomite precipitation is observed in the simulation. The cumulative sequestration of CO_2 by carbonate mineral precipitation is given in Figure 8.5-3a. After 1,000 years, a maximum of 20 kg CO_2 per cubic meter medium could be sequestrated by carbonate precipitation. Addition of CO_2 mass to the solid matrix as secondary carbonate minerals decreases porosity (Figure 8.5-3b). More results on mineral alteration and on aqueous concentrations are given in the files, co2d_min.dat and co2d_conc.dat in the distribution files.

Figure 1.5—2 **Change in mineral abundance (in volume fraction, positive values indicate precipitation and negative dissolution) after different times for the 1-D radial flow problem.**

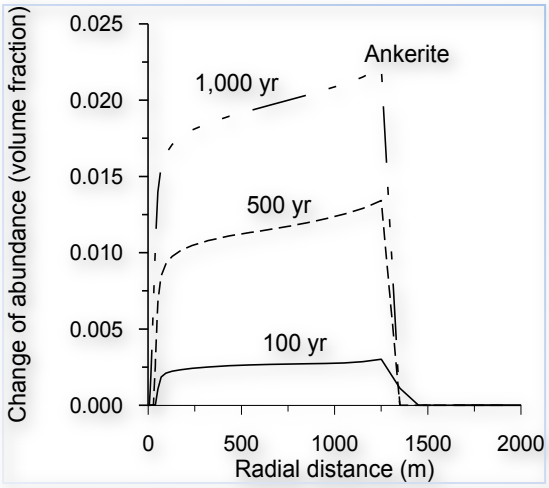

(a) Ankerite

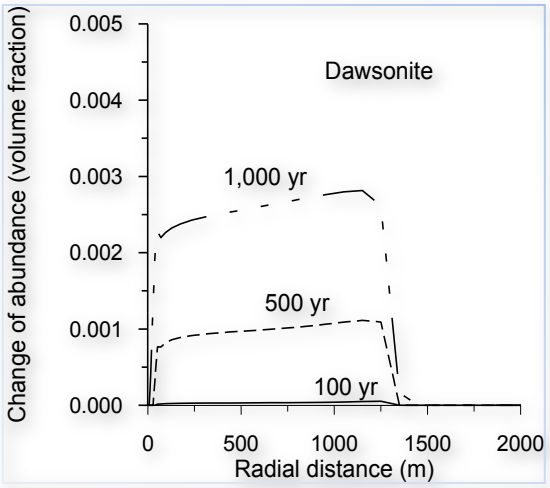

(b) Dawsonite

Figure 1.5—3 **Cumulative CO_2 sequestration by carbonate mineral precipitation for different times.**

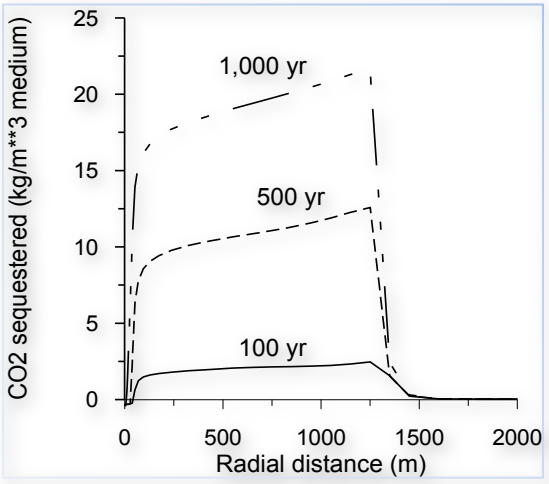

(a) CO_2 sequestered

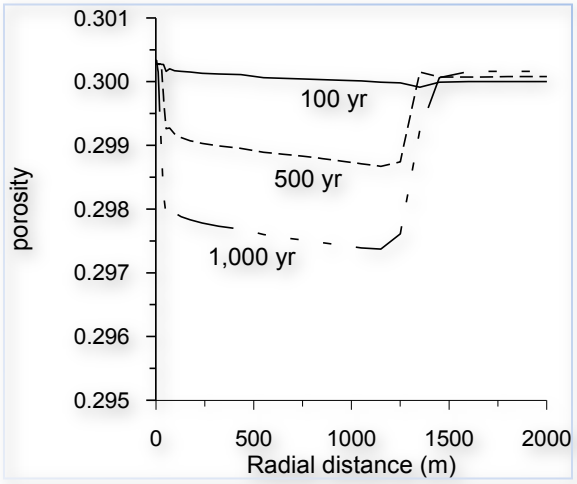

(b) Porosity

1.6 Problem 6 – 2-D Radial Model for CO_2 Sequestration in Deep Saline Formation

1.6.1 Problem Setup

The response of deep formations to CO_2 injection will depend on many factors, including formation permeability and porosity, the presence of heterogeneities such as faults and layers of high or low permeability, the physical and chemical characteristics of the brines, and the nature of the mineral phases that are present. A great deal of specific and detailed information will be required to

assess the feasibility of storing CO_2 in a brine formation at any particular site, and to develop engineering designs for CO_2 storage systems. Here, a generic two-dimensional (2-D) radial model was used to study the temporal evolution and spatial distribution of the injected CO_2 and the subsequent physical and chemical changes.

Fluid flow conditions

The 2-D radial model was a sandstone formation of 40 m thickness with a cylindrical geometrical configuration (Figure 8.6-1). The hydrogeological parameters used are essentially the same as the previous 1-D radial CO_2 sequestration problem (Table 8.5-1), except here using a porosity of 0.34, a horizontal permeability of 2.264×10^{-13} m^2, and a vertical permeability of 2.264×10^{-14} m^2. Temporal changes in porosity were calculated dynamically from changes in mineral volumes, and permeability calculated using cubic law (Eq. F.2 in Appendix F). A hydrostatic pressure distribution over the depth was specified initially. The shale caprock was assumed impermeable and non-reactive for the present study of coupled processes in the storage reservoir.

Figure 1.6—1 **Schematic representation of the 2-D radial flow model for supercritical CO_2 injection into a sandstone formation.**

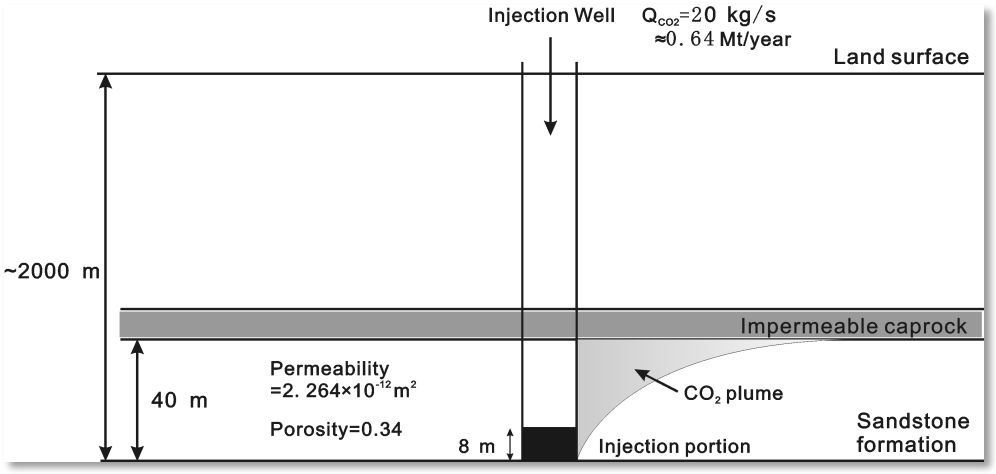

For numerical simulation, in the vertical direction a total of 20 model layers were used with a constant spacing of 2 m. In the horizontal direction, a radial distance of 100 km was modeled with a radial spacing that increases gradually away from the injection well. A total of 56 radial grid elements were used. The volume of the outer grid element is specified a large value of 10^{30} m^3, representing an infinite lateral boundary for constant pressure, temperature and concentrations. CO_2 injection was applied at the bottom portion over 8 m thickness with a constant rate of 20 kg/s (corresponding to 0.64 Mt/year) for a period of 10 years. The 2-D radial model of fluid flow and geochemical transport

was simulated for a period for 1,000 years, which may be the interested time scale for CO_2 geological sequestration. We started a homogeneous field for the geological model, later heterogeneity resulted from changes in porosity and permeability due to mineral alteration will seed the instability and motivate the convective mixing.

1.6.2 Geochemical system

The initial rock mineralogical composition was the same as the previous 1-D radial example, which may be representative of US Gulf Coast sandstone formations (Table 8.5-2). Calcite was assumed to react with aqueous species at local equilibrium because its reaction rate is typically quite rapid. Dissolution and precipitation of other minerals are kinetically-controlled. A multiple mechanism rate law is used. Kinetic parameters are the same as in the previous example. The initial water chemical composition, a NaCl-dominated brine, was also the same as the previous example. A temperature of 75°C was used throughout the domain and time, which may represent temperature at a depth of about 2 km, given a land surface temperature of 15°C and a geothermal gradient of 30°C/km.

1.6.3 Simulations

Same as the previous example, ECO2N fluid module was used for this 2-D radial flow CO_2 sequestration problem. As mentioned above, the reactive transport simulation was performed for a time period of 1,000 years. We performed a series of two TOUGHREACT runs. The first run was performed for 10 years (injection period). The input and major output files for the first run are provided with the distribution files. For the continuation run (restart) to 1,000 yr, create a new subdirectory into which copy the input files (flow.inp, solute.inp, chemical.inp, thermkin10.dat), the CO_2 property file (CO_2TAB), and the files SAVE and savechem from the first run. File SAVE is renamed INCON, savechem is renamed inchem, and the following minor changes are made in flow.inp: delete the INCON input block, and change the final simulation time from 3.15576E08 (10 years) to 3.15576E10 (1,000 years) in the PARAM input block. Now the restart run can be executed.

1.6.4 Results and discussion

Simulation results indicate that the supercritical CO_2 fluid injected at near the bottom of the storage formation migrates upward rapidly by buoyancy forces because the density of supercritical CO_2 phase is lower than that of aqueous phase (Figure 8.6-2). A small fraction of CO_2 gas is trapped in the porous rock as residual gas after injection. The residual gas trapping keeps CO_2 dissolving into brine and precipitating carbonate minerals, and gradually disappears at the bottom of the reservoir. With time most of the free CO_2 gas accumulates below the caprock, and then spreads laterally.

Figure 1.6—2 **Distribution of supercritical CO_2 phase saturation at 10 and 1000 yr for the 2-D radial injection model.**

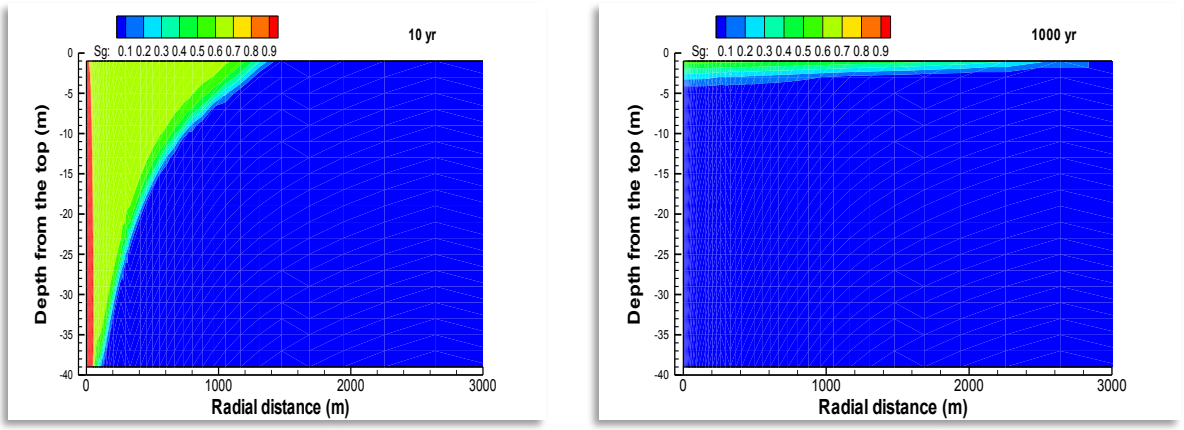

With the migration of CO_2 gas, the concentration of dissolved CO_2 rapidly increases to larger than 1 mol/kg H_2O in the two-phase region (Figure 8.6-3). The injected CO_2 dissolves in the surrounding formation water, forming H_2CO_3, HCO_3^-, and CO_3^{2-}, and decreasing pH. Then, the increased acidity induces dissolution of many of the primary host rock minerals (discussed later). The mineral dissolution increases concentrations of cations such as Na^+, Ca^{2+}, Mg^{2+}, and Fe^{2+}, which in turn form aqueous complexes with the bicarbonate ion such as $NaHCO_3$, $CaHCO_3^+$, $MgHCO_3^+$, and $FeHCO_3^+$. Over time they tend to increase dissolved CO_2 (solubility) and enhance solubility trapping.

Figure 1.6—3 **Distribution of total dissolved CO_2 (mol/kg H_2O) at 10 and 1000 yr.**

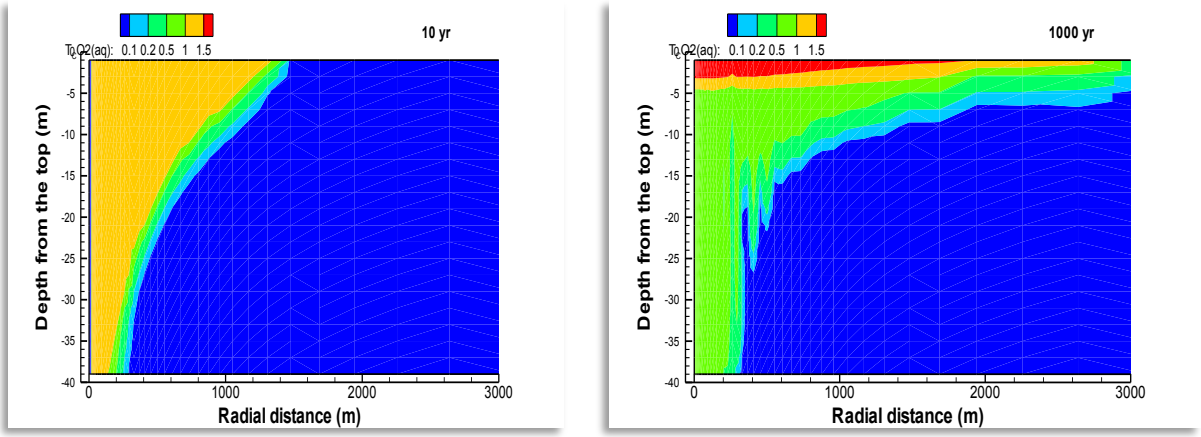

Minerals such as oligoclase and chlorite dissolve in the two-phase region and near the front of the single aqueous-phase zone, supplying reactants for carbonate mineral precipitation. Some

amount of siderite and dawsonite, and significant amount of ankerite precipitate (Figure 8.6-4), sequestering injected CO_2 (mineral trapping). At the same time, clay minerals such as smectite-Na precipitate. Changes in porosity are calculated from variations in mineral volume fractions (the bottom of Figure 8.6-5). Figures 8.6-3 and 8.6-4 show "finger" flow patterns near the bottom of the CO_2 plume. These are because of advection in the aqueous phase that is triggered by an increase in density due to CO_2 dissolution.

Figure 1.6—4 Distribution of siderite and ankerite precipitation at 1000 yr.

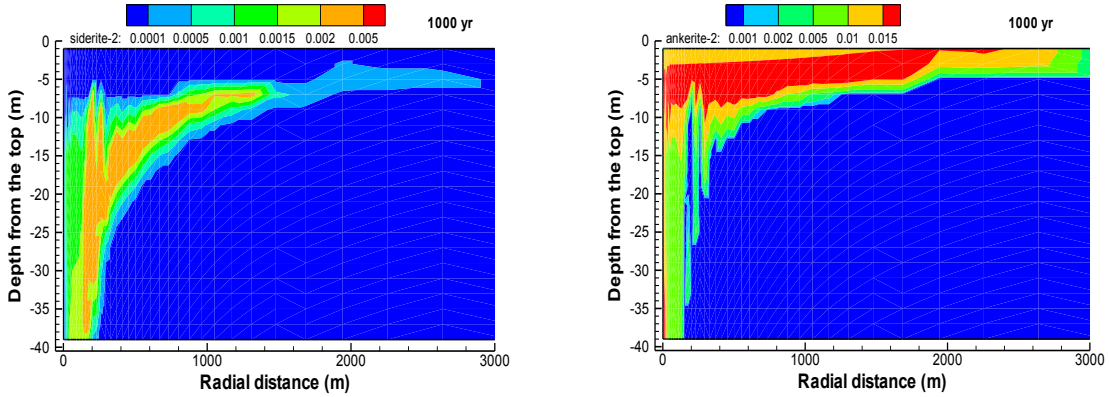

Figure 1.6—5 Distribution of porosity change at 1000 yr.

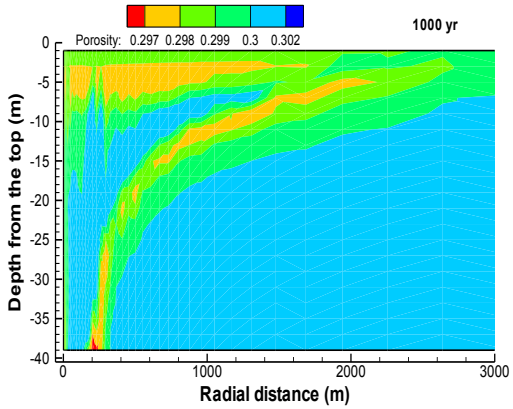

Mineral alteration and CO_2 trapping capability depends on the primary mineral composition. Precipitation of siderite and ankerite requires Fe^{2+}, which can be supplied by the dissolution of iron-bearing minerals, such as chlorite, or by reduction of Fe^{3+} in small amounts of hematite. Variation in Ca content in plagioclase significantly affects carbonate mineral precipitation, and thus CO_2 mineral trapping. The time required for mineral alteration and CO_2 sequestration depends on the rates of

mineral dissolution and precipitation, which are products of the kinetic rate constant and reactive surface area. The current simulated mineral alteration pattern is generally consistent with available mineralogy observed at natural high-pressure CO_2 gas reservoirs.

1.7 Problem 7 – Supergene Copper Enrichment (EOS9)

1.7.1 Problem statement

This simulation problem was published in Xu et al. (2001). Supergene copper enrichment (SCE) involves hydrochemical differentiation by near-surface weathering processes in which water transports metals from a source region or leached zone (Brimhall et al., 1985; Brimhall and Dietrich, 1987; Ague and Brimhall, 1989) to an enrichment blanket zone where they are reprecipitated as secondary ore compounds conserving mass (Figure 8.7-1). The schematic system shown in Figure 8.7-1 captures, in a simplified manner, conditions of desertification in Northern Chile that led to oxidation and chemical enrichment of copper deposits at certain times in the past (of order 15 Ma) when a decline of the ground water table exposed sulfides to unsaturated conditions (Brimhall et al., 1985; Brimhall and Dietrich, 1987; Alpers and Brimhall, 1989; Ague and Brimhall, 1989).

Figure 1.7—1 **A schematic representation of a supergene copper enrichment system according to Ague and Brimhall (1989).**

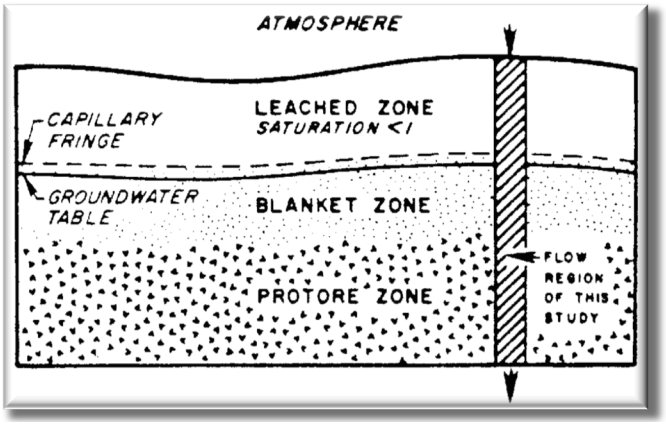

Oxidative weathering of pyrite (FeS_2) and chalcopyrite ($CuFeS_2$) causes acidification and mobilization of metals in the oxidizing zone and intense alteration of primary minerals, with subsequent formation of enriched secondary copper bearing sulfide mineral deposits (enrichment blanket) in the reducing conditions below the water table. Such oxidative weathering-driven processes have produced some of the world's largest copper deposits (Ague and Brimhall, 1989). The present investigation on geochemical transport in SCE systems is not specific to any field site, but the geochemistry for this work was based on field and laboratory studies of SCE systems as carried out

by Brimhall et al. (1985), and Ague and Brimhall (1989). The coupled modeling study is intended to provide a better understanding of the complex interplay of oxygen diffusion, sulfide mineral oxidation, subsequent intense alteration of primary minerals and reprecipitation of secondary minerals. The SCE processes typically took place in a fractured porous medium such as at the El Salvador mine, Chile (Mote et al., 2001). To gain better insight into the processes involved, we first considered a problem in a one-dimensional unsaturated-saturated porous medium. Then we considered the case of SCE processes in a variably saturated fractured rock system using the "multiple interacting continua" (MINC) method. Here we only present the case of SCE processes in a variably saturated fractured rock. The simple porous medium case is given in Xu et al. (2001)

1.7.2 Problem setup

The method of "multiple interacting continua'' (MINC) is used to resolve "global" flow and diffusion of chemicals in the fractured rock and its interaction with "local" exchange between fractures and matrix rock. This method was developed by Pruess and Narasimhan (1985) for fluid and heat flow in fractured porous media. The extension of the MINC method to reactive geochemical transport is described in detail by Xu and Pruess (2001b). It is well-known that in the case of reactive chemistry diffusive fluxes may be controlled by reactions occurring near (within millimeters) the fracture walls. The resolution of concentration gradients in matrix blocks is achieved by appropriate subgridding. The MINC concept is based on the notion that changes in fluid pressures and chemical concentrations propagate rapidly through the fracture system, while invading the tight matrix blocks only slowly. Therefore, changes in matrix conditions will be (locally) controlled by the distance from the fractures and can then be modeled by means of one-dimensional strings of nested grid blocks (Figure 8.7-2).

In general it is not necessary to consider explicitly subgrids in all the matrix blocks separately. Within a certain subdomain (corresponding to a finite difference grid block), all fractures will be lumped into continuum # 1, all matrix material within a certain distance from the fractures will be lumped into continuum # 2, matrix material at larger distance becomes continuum # 3, and so on. Quantitatively, the subgridding is specified by means of a set of volume fractions VOL(j), j = 1, ..., J, into which the "primary" porous medium grid blocks are partitioned. The information on fracturing (spacing, number of sets, shape of matrix blocks) required for this is provided by a "proximity function" PROX(x) which expresses, for a given domain V_0 , the total fraction of matrix material within a distance x from the fractures (Pruess and Karasaki, 1982). If only two continua are specified (one for fractures, one for matrix), the MINC approach reduces to the conventional double-porosity or dual permeability methods.

We consider an idealized fractured porous medium with two perpendicular sets of plane, parallel, vertical fractures of equal aperture and spacing. Because of symmetry only one column of matrix blocks needs to be modeled. Figure 8.7-2 shows an areal view of a rock matrix column that is surrounded by vertical fractures with a spacing of 0.5 m, with subgridding of the matrix according to the MINC method. Subgrid 1 represents the fracture domain that is defined to include 50 percent by volume of wall rock. Subgrids 2 through 7 represent the rock matrix. In the vertical direction, a total of 10 model layers are used with a thickness of 2 m. A net rainwater infiltration rate of 0.015 m yr^{-1} over the entire area was applied to the fractures. Water pressure is held constant at 2 bars at the bottom (z = -20 m), so that the water table is located at a depth of approximately 10 m. In addition to global water flow and chemical transport in the fracture network, the model considers flow and transport between fractures and matrix, as well as vertical matrix-matrix water flow and chemical transport. The steady-state water saturations obtained without chemical reactions are used as initial conditions for the calculation of reactive geochemical transport. Hydrological parameters for the fracture and matrix are listed in Table 8.7-1.

Figure 1.7—2 **Subgridding of a rock matrix in the method of "multiple interacting continua" (MINC). The figure represents an areal view of a rock matrix column that is surrounded by vertical fractures.**

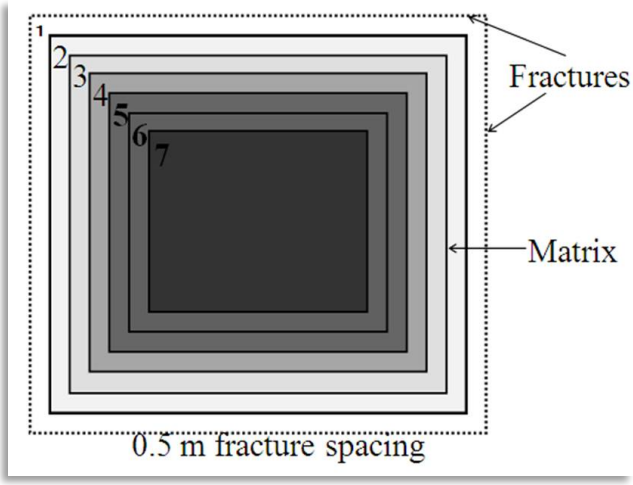

Table 1.7—1 **Hydrological parameters used for supergene copper enrichment in fractured rock.**

Parameter	Matrix	Fracture
Permeability (m^2)	10^{-16}	10^{-12}
Fracture domain volume fraction, v *		0.01
Fracture spacing (m)		0.5
Porosity	0.08	0.5

Relative permeability and capillary pressure (van Genuchten, 1980):		
λ	0.457	0.457
S_{lr}	0.1	0.05
S_{ls}	1.0	1.0
P_0(pa)	2.17×10^5	6.2×10^3

* **v = V_f/(V_f+ V_m) where V_f and V_m are fracture and matrix domain volumes.**

The geochemical transport simulation considers unsaturated-saturated liquid phase flow and diffusive supply of oxygen to the protore. The domain modeled is initially filled entirely with a protore mineral assemblage as listed in Table 8.7-2. The dissolution of the primary minerals is considered to be kinetically-controlled. The kinetic rate constants and reactive surface areas are also given in Table 8.7-2. Precipitation of secondary minerals (Table 8.7-2 with initial $V_f = 0$ where V_f is mineral volume fraction) is represented using the same expression as dissolution. To simplify the description of precipitation kinetics, in the present study all secondary minerals are assigned the same kinetic rate constant (2.0×10^{-10} mol $m^{-2}s^{-1}$) and reactive surface areas (0.1 m^2 per dm^3 bulk medium). Because the rate constants assumed for precipitation reactions are larger than those for dissolution of primary minerals, formation of secondary minerals occurs effectively at conditions close to local equilibrium. The kinetic rate of sulfide mineral oxidation can be strongly influenced by catalytic effects of bacteria (Singer and Stumm, 1970; Olson, 1991; Nordstrom and Alpers, 1997), which are not considered in the present study. Estimates of field oxidation rate cover a wide range of values (Nordstrom and Alpers, 1997). The rate determining process is commonly the transport of oxygen or other reactants to the reaction site. This process is the main focus of the simulation. Heat generation by pyrite oxidation may change temperature, but this effect is not considered in the simulations. Calculations are carried out at a constant temperature of 25°C. Thermodynamic data used in the simulations were taken from the EQ3/6 V8.2b database (Wolery, 1992), which were derived using SUPCRT92 (Johnson et al., 1992).

Table 1.7—2 **Initial protore mineral volume fractions (V_f) and possible secondary mineral phases (V_f = 0.0) considered in the supergene copper enrichment problem. Kinetic data for primary minerals are based on Ague and Brimhall (1989) and Gérard et al. (1997).**

Mineral	Composition	Volume fraction, V_f	Rate constant at 25°C (mol $m^{-2}s^{-1}$)	Surface area (m^2 dm^{-3} medium)
Primary:				
pyrite	FeS_2	0.090	4.0×10^{-11}	0.0587
chalcopyrite	$CuFeS_2$	0.045	4.0×10^{-11}	0.0587

magnetite	Fe_3O_4	0.045	$2.0x10^{-11}$	0.0787
k-feldspar	$KAlSi_3O_8$	0.180	$3.1x10^{-12}$	0.2710
albite	$NaAlSi_3O_8$	0.090	$3.1x10^{-12}$	0.1360
anorthite	$CaAl_2Si_2O_8$	0.090	$1.5x10^{-12}$	0.1420
annite	$KFe_3AlSi_3O_{10}(OH)_2$	0.045	$2.4x10^{-14}$	0.0587
muscovite	$KAl_3Si_3O_{10}(OH)_2$	0.090	$2.4x10^{-14}$	0.0123
quartz	SiO_2	0.180	$4.3x10^{-14}$	0.0850
anhydrite	$CaSO_4$	0.045	$1.5x10^{-12}$	0.0510
		total=0.9		
		porosity=0.1		
Secondary:				
covellite	CuS	0.0	$2.0x10^{-10}$	0.1
chalcocite	Cu_2S	0.0	$2.0x10^{-10}$	0.1
bornite	Cu_5FeS_4	0.0	$2.0x10^{-10}$	0.1
goethite	FeOOH	0.0	$2.0x10^{-10}$	0.1
hematite	Fe_2O_3	0.0	$2.0x10^{-10}$	0.1
kaolinite	$Al_2Si_2O_5(OH)_4$	0.0	$2.0x10^{-10}$	0.1
alunite	$KAl_3(OH)_6(SO_4)_2$	0.0	$2.0x10^{-10}$	0.1
amorphous silica	SiO_2	0.0	$2.0x10^{-10}$	0.1

Oxygen is treated as an ideal gas, and its interaction with the aqueous solution is assumed to be at equilibrium. The oxygen partial pressure at the land surface boundary is assumed to be constant at 0.2 bars. A dilute oxidized water that was equilibrated with an oxygen partial pressure of 0.2 bars is initially placed in the unsaturated zone, while a reducing water is assumed for the saturated zone. The infiltrating water composition is the same as the initial unsaturated water. The aqueous complexation is assumed at equilibrium, even though some aqueous redox pairs such as sulfite and sulfide species may not be at equilibrium (Stumm and Morgan, 1981). Whether a particular reaction should be described as governed by the local equilibrium approximation (LEA) or by kinetic rates depends not only on the reaction itself but also on the rates of hydrodynamic transport processes (Domenico and Schwarz, 1990). The LEA is applicable when the characteristic time for transport of reactants is longer than the time required to reach chemical equilibrium. In the present simulations for reactive geochemical transport, the choice of equilibrium depends mainly on kinetic rate, infiltration rate, oxygen availability, and space discretization.

The EOS9 flow module was used for this ambient mineral deposition problem. The input and output files for the problem are provided with the distribution files. To shorten the run time for benchmarking purposes, the simulation time in the PARAM input block of flow.inp is specified as 3.15576E08 s (or 10 years). Users can reset this variable to their desired time. Parts of output files

for fluid flow, aqueous chemical concentrations, and changes of mineral abundances are given in Figures 8.7-3, 8.7-4 and 8.7-5.

Figure 1.7—3 Part of file flow.out for Problem 7.

```
@@@@@@@@@@@@@@@@@@@@@@@@@@@@@@@@@@@@@@@@@@@@@@@@@@@@@@@@@@@@@@@@@@@@@@@@@@

 TOTAL TIME      KCYC    ITER  ITERC    KON         DX1M
 0.31557E+08    7330       2  14660      2       0.22258E-06

@@@@@@@@@@@@@@@@@@@@@@@@@@@@@@@@@@@@@@@@@@@@@@@@@@@@@@@@@@@@@@@@@@@@@@@@@@

ELEM.  INDEX    PRES         S(liq)       PCAP         K(rel)       DIFFUS.
                (PA)                      (PA)                      (m^2/s)

TOP 0      1 0.10000E+06 0.29322E-01 0.00000E+00 0.00000E+00 0.00000E+00
    1      2 0.10000E+06 0.26921E+00 -.28543E+05 0.14555E-04 0.43658E-08
2   1      3 0.10000E+06 0.97605E+00 -.44640E+05 0.51420E+00 0.75917E-06
3   1      4 0.10000E+06 0.97605E+00 -.44641E+05 0.51419E+00 0.75914E-06
4   1      5 0.10000E+06 0.97604E+00 -.44645E+05 0.51416E+00 0.75906E-06
5   1      6 0.10000E+06 0.97604E+00 -.44652E+05 0.51411E+00 0.75890E-06
6   1      7 0.10000E+06 0.97602E+00 -.44664E+05 0.51402E+00 0.75862E-06
7   1      8 0.10000E+06 0.97601E+00 -.44677E+05 0.51393E+00 0.75833E-06
    2      9 0.10000E+06 0.25775E+00 -.30146E+05 0.88783E-05 0.29217E-08
2   2     10 0.10000E+06 0.98320E+00 -.36590E+05 0.57672E+00 0.98343E-06
3   2     11 0.10000E+06 0.98320E+00 -.36591E+05 0.57672E+00 0.98342E-06
4   2     12 0.10000E+06 0.98320E+00 -.36591E+05 0.57671E+00 0.98339E-06
5   2     13 0.10000E+06 0.98319E+00 -.36593E+05 0.57670E+00 0.98334E-06
6   2     14 0.10000E+06 0.98319E+00 -.36596E+05 0.57668E+00 0.98325E-06
7   2     15 0.10000E+06 0.98319E+00 -.36598E+05 0.57665E+00 0.98315E-06
```

Figure 1.7—4 Part of file Amic_aqu.dat for Problem 7 after t = 1 yr (Sl is water saturation, unit of concentrations is mol/l).

```
   X       Y          Sl         pH     t_so4-2     t_fe+2      t_cu+2      t_na+

 0.000     0.000  0.2932E-06  7.0000  0.1037E-11  0.7326E-12  0.1030E-11  0.1007E-04
 0.000    -1.000  0.2692E-05  3.7720  0.1449E-03  0.3642E-04  0.2163E-04  0.1209E-04
 0.254    -1.000  0.9760E-05  3.7660  0.1470E-03  0.3698E-04  0.2194E-04  0.1212E-04
 0.900    -1.000  0.9760E-05  3.7471  0.1540E-03  0.3880E-04  0.2298E-04  0.1222E-04
 2.247    -1.000  0.9760E-05  3.7140  0.1668E-03  0.4217E-04  0.2490E-04  0.1240E-04
 5.215    -1.000  0.9760E-05  3.6703  0.1856E-03  0.4703E-04  0.2770E-04  0.1266E-04
10.790    -1.000  0.9760E-05  3.6422  0.1988E-03  0.5041E-04  0.2967E-04  0.1284E-04
14.340    -1.000  0.9760E-05  3.6362  0.2017E-03  0.5116E-04  0.3011E-04  0.1288E-04
 0.000    -3.000  0.2578E-05  3.6711  0.1849E-03  0.4648E-04  0.2760E-04  0.1265E-04
 0.254    -3.000  0.9832E-05  3.6699  0.1855E-03  0.4665E-04  0.2768E-04  0.1266E-04
 0.900    -3.000  0.9832E-05  3.6661  0.1873E-03  0.4718E-04  0.2795E-04  0.1268E-04
 2.247    -3.000  0.9832E-05  3.6588  0.1907E-03  0.4819E-04  0.2847E-04  0.1273E-04
 5.215    -3.000  0.9832E-05  3.6472  0.1963E-03  0.4973E-04  0.2930E-04  0.1281E-04
10.790    -3.000  0.9832E-05  3.6379  0.2009E-03  0.5094E-04  0.2998E-04  0.1287E-04
14.340    -3.000  0.9832E-05  3.6357  0.2020E-03  0.5122E-04  0.3015E-04  0.1289E-04
```

Figure 1.7—5 Part of file Amic_sod.dat for Problem 7, showing changes in mineral abundances (in volume fraction, positive values indicate precipitation and negative dissolution) after t = 1 yr.

```
   X       Y          pyrite    chalcopyrit  magnetite   k-feldspar   albite

 0.000     0.000  0.0000E+00  0.0000E+00  0.0000E+00  0.0000E+00  0.0000E+00
 0.000    -1.000 -0.9909E-08 -0.7578E-08 -0.4777E-08 -0.3563E-08 -0.1678E-08
 0.254    -1.000 -0.1322E-06 -0.1011E-06 -0.6373E-07 -0.4753E-07 -0.2239E-07
 0.900    -1.000 -0.1322E-06 -0.1011E-06 -0.6373E-07 -0.4753E-07 -0.2239E-07
```

```
 2.247     -1.000 -0.1322E-06 -0.1011E-06 -0.6372E-07 -0.4753E-07 -0.2239E-07
 5.215     -1.000 -0.1322E-06 -0.1011E-06 -0.6372E-07 -0.4753E-07 -0.2239E-07
10.790     -1.000 -0.1322E-06 -0.1011E-06 -0.6372E-07 -0.4753E-07 -0.2239E-07
14.340     -1.000 -0.1322E-06 -0.1011E-06 -0.6372E-07 -0.4753E-07 -0.2239E-07
 0.000     -3.000 -0.9488E-08 -0.7257E-08 -0.4574E-08 -0.3412E-08 -0.1607E-08
 0.254     -3.000 -0.1332E-06 -0.1018E-06 -0.6419E-07 -0.4788E-07 -0.2255E-07
 0.900     -3.000 -0.1332E-06 -0.1018E-06 -0.6419E-07 -0.4788E-07 -0.2255E-07
 2.247     -3.000 -0.1332E-06 -0.1018E-06 -0.6419E-07 -0.4788E-07 -0.2255E-07
 5.215     -3.000 -0.1332E-06 -0.1018E-06 -0.6419E-07 -0.4788E-07 -0.2255E-07
10.790     -3.000 -0.1332E-06 -0.1018E-06 -0.6419E-07 -0.4788E-07 -0.2255E-07
14.340     -3.000 -0.1332E-06 -0.1018E-06 -0.6419E-07 -0.4788E-07 -0.2255E-07
```

1.7.3 Results

Some selected plots of simulation results are presented in Figures 8.7-6, 8.7-7, and 8.7-8. More results and discussion are presented in Xu et al. (2001).

Figure 1.7—6 Steady-state water saturation and water flux (relative to total infiltration) passed through the fractures

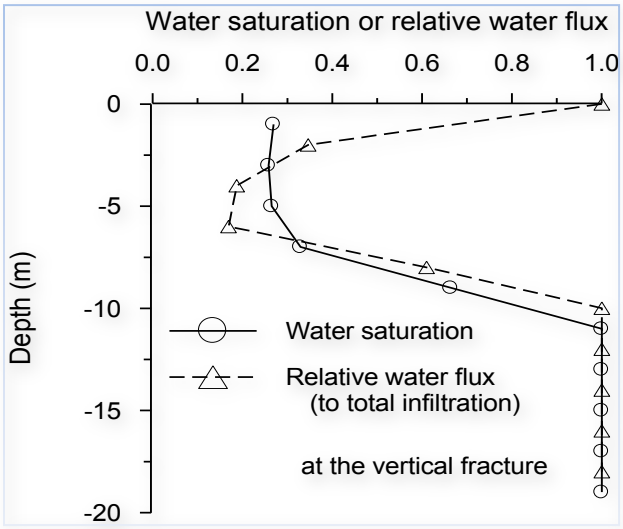

Figure 1.7—7 Change of mineral abundance (positive values indicate precipitation and negative dissolution) after 20,000 yrs in the fractured rock.

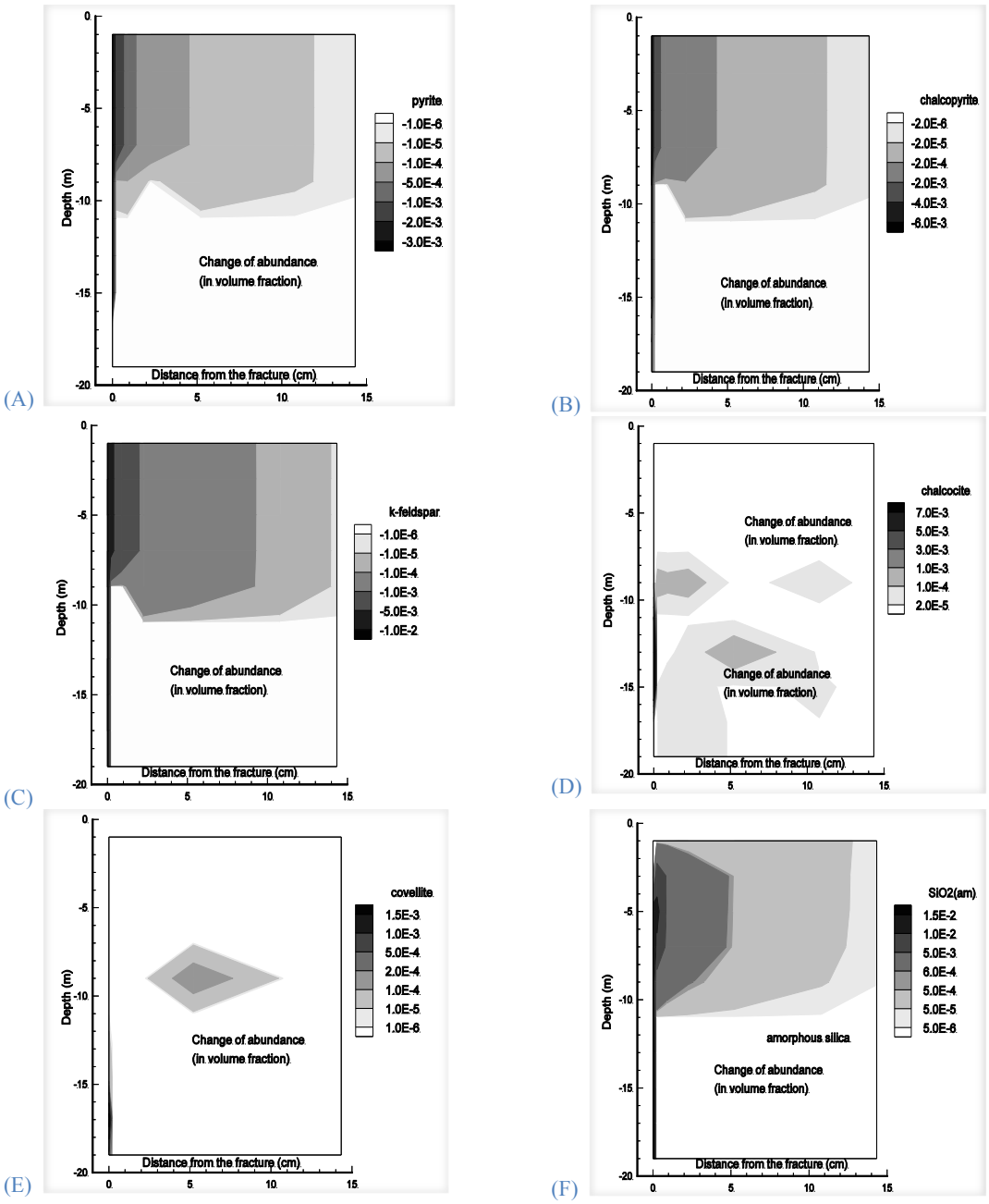

Figure 1.7—8 pH and dissolved copper concentration at 20,000 yrs in the fractured rock.

(A)

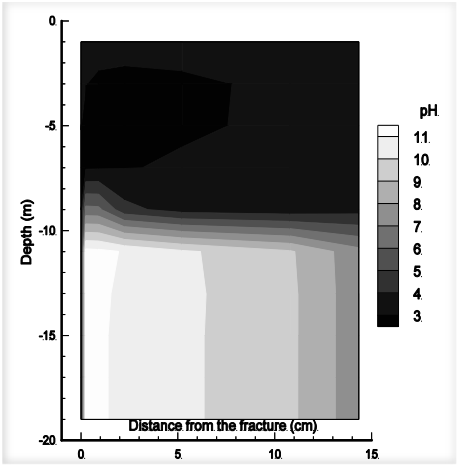

(B)

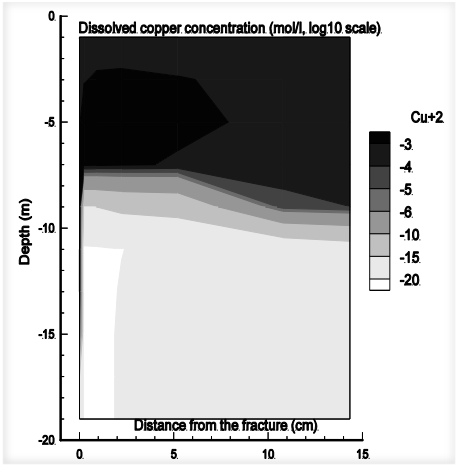

1.8 Problem 8 – Injection Well Scaling and Acidizing at Tiwi Field, Philippines (EOS1)

1.8.1 Problem statement

Nag-67 is one of the hot brine injectors located to the south-east of the Tiwi geothermal field, Philippines. The well was completed in March 1987. The injectivity of the well decreased significantly with time. The drop in injection capacity was attributed to scaling inside the wellbore as early as October 1992.

Records of injection history (Figure 8.8-1) and fluid chemistry for Nag-67 were reviewed to determine the nature of the deposited scale and to estimate the amount and location of the deposits. The well was acidized in January 1989 primarily to clear the near-wellbore formation of drilling mud damage and to improve its injectivity. Injection capacity of the well after the stimulation was 126 kg/s at a wellhead pressure of 1.38 MPa. In 1996, the well was found to accept only 38 kg/s at an injection wellhead pressure of about 1 MPa. In 1999, an injectivity test indicated that the capacity of the well had dropped to 17 kg/s at an injection wellhead pressure of 1.31 MPa. In March 2000, the recorded injection rate in Nag-67 suddenly decreased to 3. 8 kg/s.

In January 2001, the scale inside the Nag-67 wellbore was drilled-out, and the scale deposited in the near-well formation was dissolved by acid. Measurements after the scale drillout indicated that the capacity of the injector went up to 25.2 kg/s, and another test after the acid stimulation showed a further increase to 113.4 kg/s. These results strongly suggested that the decline in injectivity of the well was caused primarily by scale deposition in the near-well formation. Based on the chemistry of the brine injected and analysis of deposited scale, it was determined that most of the scale in Nag -67 was amorphous silica.

The silica concentration and pH of the brine being supplied to the Nag-67 injector were monitored between 1989 and 2000. Complete brine analyses were also available for every year except 1999 and were used to characterize the saturation state of the brine with respect to other minerals. From this historical chemical record, the degree of amorphous silica saturation in each analyzed water sample was determined.

Figure 1.8—1 Historical injection rates (kg/s) in Nag-67.

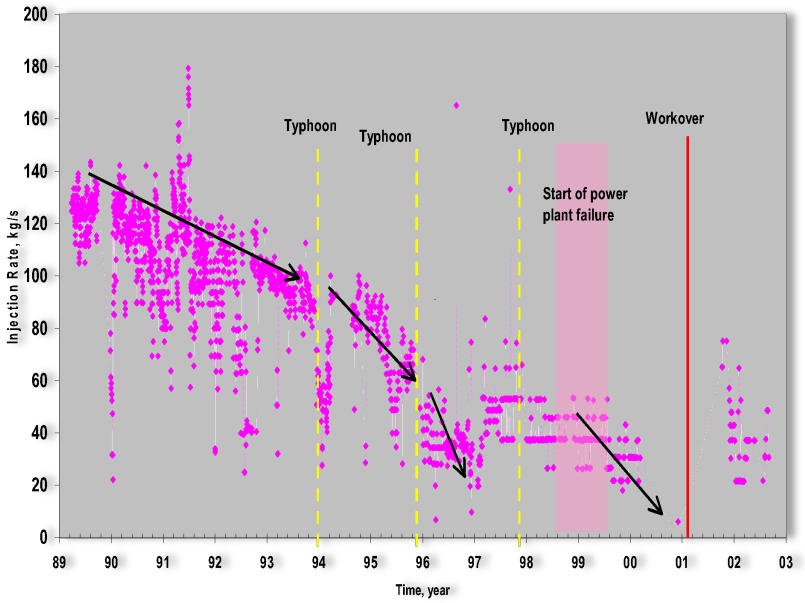

The estimated amount of silica (in the formation) dissolved by acid stimulation was calculated by assuming that the acid dissolved a stoichiometrically equivalent amount of silica. The silica scale volume calculated in this way was only 1.4 m^3. The dissolution of this seemingly small amount of amorphous silica nevertheless increased the injection capacity of the well to near original capacity. Therefore, it would appear that a significant part of the injectivity loss was related to silica deposition in the formation close to the wellbore, as opposed to in the wellbore itself.

To understand the scaling process and loss of injectivity in hot brine injectors, Ontoy et al. (2003) identified factors that cause the deposition of amorphous silica in the near-well formation and the extent of their effect using TOUGHREACT. These factors include the silica concentration in the hot brine injectate, the temperature of the injectate, the flowrate of the injectate, the pH of the injectate, and the temperature and pressure conditions of the reservoir in the vicinity of the injector.

Xu et al. (2004b) conducted a large number of numerical simulations to reproduce the loss of injectivity and its recovery by acid injection. A porosity-permeability relationship (Verma and Pruess,

1988; see Eq. F.8 in Appendix F) was calibrated by comparing predicted injection indexes with field observed data. Here we give brief description of the work of Xu et al. (2004b).

1.8.2 Problem setup

Grid and fluid flow parameters

A 120 m thick reservoir formation at the bottommost permeable zone of the injection well (Nag-67) was modeled. A simple one-dimensional radial flow model was used, consisting of 50 radial blocks with logarithmically increasing radii (Figure 8.8-2). The 50 blocks represent a distance of 1000 m from the wall of the drilled open hole. A fracture porosity of 1% (ratio of fracture volume over the total formation volume) was assumed. The initial bulk permeability has been estimated at 8.5×10^{-14} m^2, to be consistent with the observed initial injectivity index of the well. Conductive heat exchange with rocks of low permeability above and below this zone is an important process. The confining layers are modeled as semi-infinite half spaces, and heat exchange is treated with a semi-analytical technique due to Vinsome and Westerveld (1980).

Figure 1.8—2 Simplified conceptual model for injection well Nag-67.

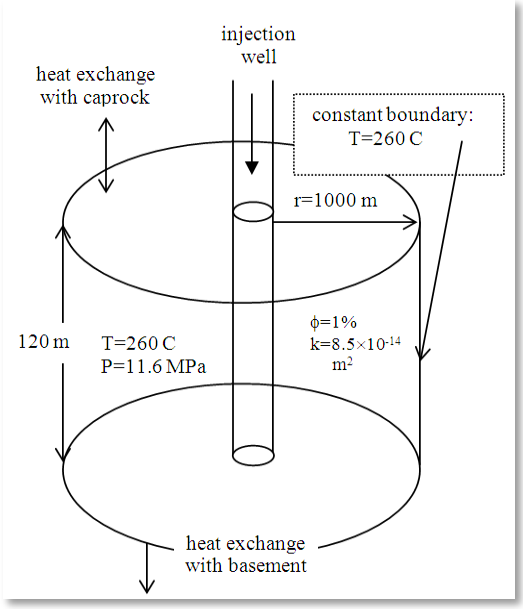

Only the fracture network is considered in the flow simulation, with the assumption that the fluid exchange with the surrounding low permeability matrix is insignificant. To allow for chemical reaction with the rock, 50% porosity was assigned to the blocks, and the total volume was accordingly doubled. The simulation zone was therefore “compressed” into a 2.4 m thick layer with

50% pore volume and 50% rock volume. A fracture permeability of 4.3×10^{-12} m^2 was used in the simulation (corresponding to a bulk fracture permeability value of 8.5×10^{-14} m^2 for the whole formation thickness with 1% fracture porosity). For consistency, bulk fracture porosity and permeability are reported here.

Initial reservoir temperature and pressure were assumed as 260°C and 11.6 MPa, respectively. The injection history of the well was used to define the amount of injected mass versus time (Figure 8.8-1): 50% of the total injection rate in Nag-67 was used because spinner surveys showed that the bottommost permeable zone accepted about 50% of the injectate. A constant injection temperature of 160°C was used because measured temperature fluctuations were generally small and with a relatively flat average trend (Figure 8.8-3).

Figure 1.8—3 Measured temperature of the injected water.

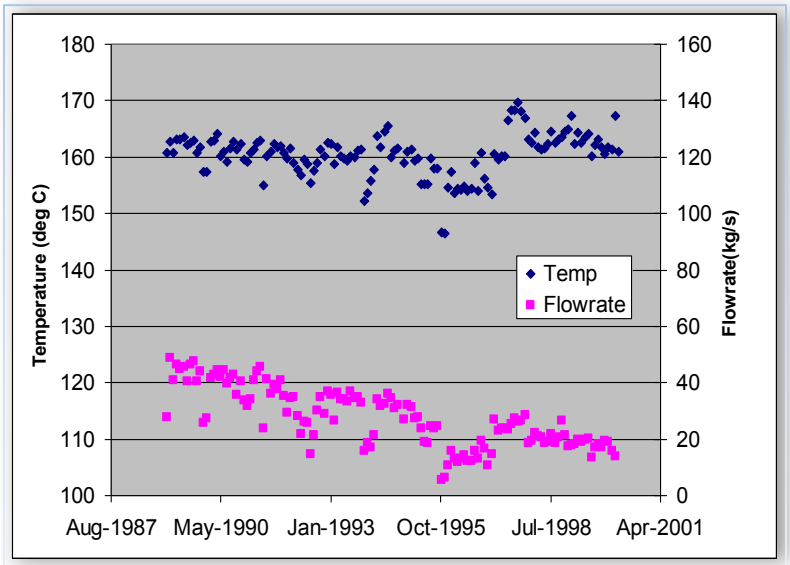

Geochemical data

The types and initial abundances of primary minerals were determined from the reported Nag-67 alteration mineralogy at the 1798-1920 m MD permeable zone (propylitic/phyllic rock). Secondary minerals were also determined from field observations (Table 8.8-1).

Table 1.8—1 List of minerals and aqueous species considered in the simulations

Mineral	Mineral Precipitation/Dissolution	Mineral Initial Volume fraction	Primary Aqueous Components
Primary:			
albite-low	Kinetic	0.18	H_2O H^+ Ca^{+2} Mg^{+2} Na^+ Cl^- $SiO_{2(aq)}$ HCO_3^- SO_4^{-2} K^+ AlO_2
anorthite	Kinetic	0.02	
illite	Kinetic	0.05	
quartz	Kinetic	0.14	
muscovite	Kinetic	0.16	
clinochlore-7a	Kinetic	0.08	
clinozoisite	Kinetic	0.01	
calcite	Equilibrium	0.13	
Secondary:			
amorphous silica	Kinetic		
microcline	Kinetic		
kaolinite	Kinetic		
anhydrite	Equilibrium		

The composition of the injected brine was provided from historical analytical data. The formation water was reconstituted from the known brine composition as follows. First, the brine was diluted to yield saturation with quartz at the observed reservoir temperature of 260°C (thus reversing the concentrative effect of flashing). The resulting water was then equilibrated with minerals identified in the well mineralogy log (calculating the aluminum concentration using equilibrium with microcline, sodium using albite, pH using calcite, calcium using clinozoisite, and magnesium using clinochlore). Calcite and anhydrite were assumed to react at equilibrium because their reaction rate is typically quite rapid. Other minerals were set to react under kinetic constraints (Table 8.8-1). Thermodynamic and kinetic data for amorphous silica were taken from Carroll et al. (1998), and Gunnarsson and Arnorsson (2000). For other minerals, thermodynamic and kinetic data were taken from various other literature sources.

For all minerals except amorphous silica, input surface areas were estimated from the geometry of the modeled fracture (around 130 m^2/m^3 medium). For amorphous silica, a large surface area was estimated (10^7 cm^2/g) from Parks (1990, Fig. 16). Such a large value takes into account the very small size of amorphous silica particles in solution. Silica concentrations of 705 and 710 ppm were used, within the range of observed values (Figure 8.8-4).

Figure 1.8—4 Evolution of silica concentrations in the injected water.

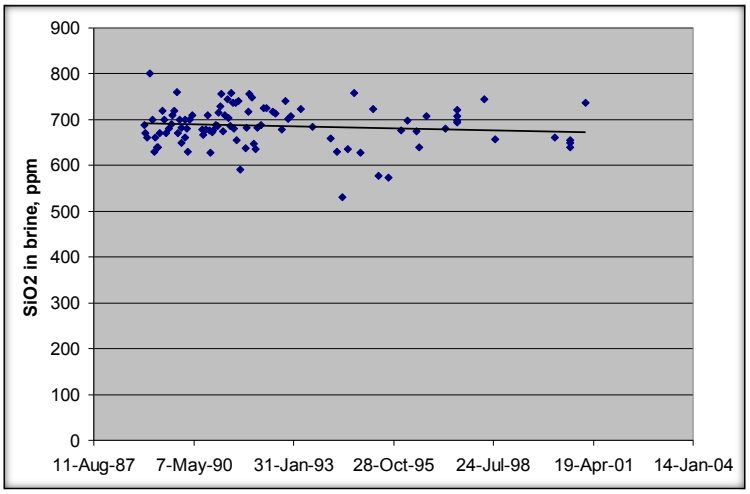

Parameters ϕ_c and n in Eq. (F. 8) in Appendix F were calibrated by comparing simulated injection indexes with measured data. The injection index is defined as

$$II = \frac{Flowrate}{P_b - P_i} \tag{8.1}$$

where, P_b is the borehole pressure and P_i is the initial reservoir pressure (116 bar). A total of 18 simulations were performed using the silica concentrations and values of parameters ϕ_c and n as listed in Table 8.8-2. The simulated time of injection was approximately 12 years, corresponding to the time from the initial acidization of the well in January, 1989, to the time of the well workover in January, 2001.

Table 1.8—2 List of simulations using different injection silica concentrations and values of parameters ϕ_c and n.

Silica concentration (ppm)	ϕ_c(%)	n	Simulation number
705	0.88	9	1
		11	2
		13	3
	0.90	7	4
		9	5
		11	6
	0.92	6	7
		8	8
		10	9

	0.94	3	10
		5	11
		6	12
710	0.90	3	13
		4	14
		5	15
	0.92	2	16
		3	17
		4	18

1.8.3 Results and discussion

The injection indexes can be reproduced by different sets of parameter combinations in the porosity-permeability relationship, Eq. (F.8) in Appendix F. For an injection silica concentration of 705 ppm, reasonable fits are obtained for the following combinations of ϕ_c and n values: (1) ϕ_c = 0.88% and n = 13, (2) ϕ_c = 0.9% and n = 11, (3) ϕ_c = 0.92% and n = 10, and (4) ϕ_c = 0.94% and n = 6. Here results obtained with only two sets of ϕ_c and n values are presented in Figure 8.8-5. More results can be found in Xu et al. (2004b). A smaller critical porosity ϕ_c requires a larger power term n. For a silica concentration of 710 ppm, the matching parameter combinations are (1) ϕ_c = 0.9% and n = 5, and (2) ϕ_c = 0.92% and n = 4. The simulated results show that small decreases in porosity result in steep reductions in permeability. This is consistent with a permeability experiment of Moore et al. (1983) in which a heated aqueous fluid was passed down a temperature gradient through Westerly Granite. The experiment showed a reduction in permeability of 96% with an 8% reduction of the initial porosity over a two-week period.

Figure 1.8—5 **Simulated injection indexes using an injection silica concentration of 705 ppm, together with measured data.**

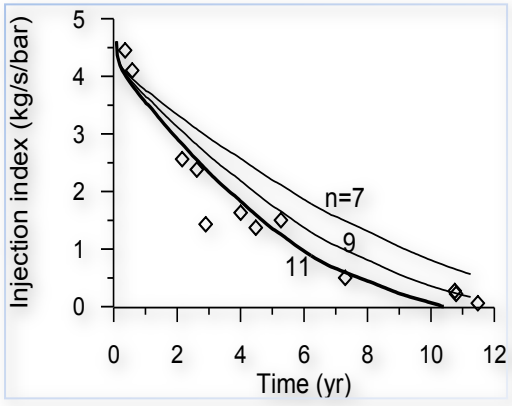

(a) ϕ_c = 0.90%

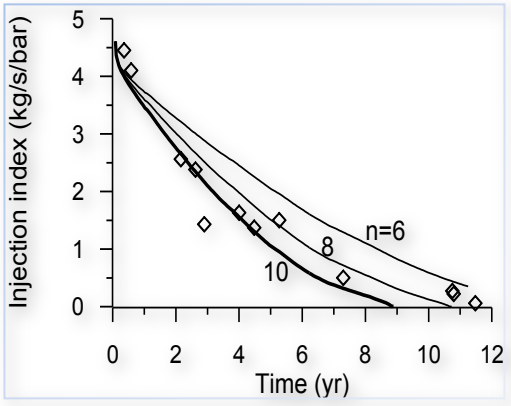

(b) ϕ_c = 0.92%

An injection silica concentration of 705 ppm results in a total amorphous silica precipitation of 5.9 m^3 in the reservoir formation, while a silica concentration of 710 ppm results in 19.5 m^3. The estimated amount of amorphous silica in the formation dissolved by acid is about 1.4 m^3. Therefore, an injection silica concentration of 705 ppm could be a reasonable number for capturing total silica precipitation.

Further review of Figure 8.8-5 shows that the simulated injection indexes reach zero at earlier times than observed. Figure 8.8-3 indicates that after January 1996 (seven years after the simulation start) temperatures increase significantly above 160°C. We then performed an additional simulation using an injection temperature of 161°C for the later time period. Other parameters for the additional simulation are an injection silica concentration of 705 ppm, ϕ_c = 0.92% and n = 10. Results of the additional simulation are presented in Figure 8.8-6, showing that the match of injection indexes to observations for the later period was improved. The higher temperature results in some early precipitated silica dissolving at later time. At the end of the simulation, a total of 2 m^3 of amorphous silica remains in the formation, similar to the actual amount of 1.4 m^3 estimated to have been dissolved by acid.

Figure 1.8—6 **Simulated injection indexes using an injection temperature of 161°C for the later time period, together with measured data (silica concentration = 705 ppm, ϕ_c = 0.92%, and n = 10).**

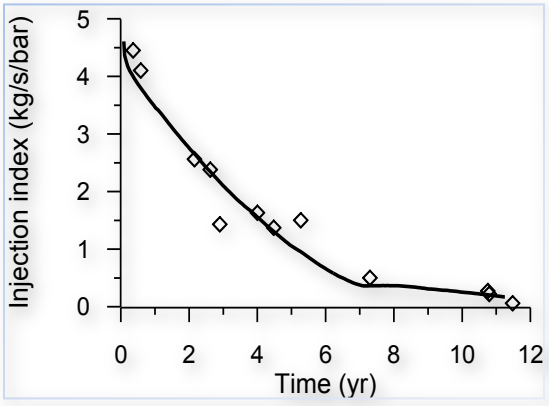

Significant reductions in porosity and permeability occur within a 10 m radius of the well (Figure 8.8-7). The pattern of permeability change on a logarithmic scale is similar to porosity change on a linear scale. The porosity reduction is mainly due to precipitation of amorphous silica (Figure 8.8-8). Some low-albite precipitation and minor illite precipitation and calcite dissolution occur in the simulations.

Figure 1.8—7 **Computed distribution of porosity and permeability along the well radius.**

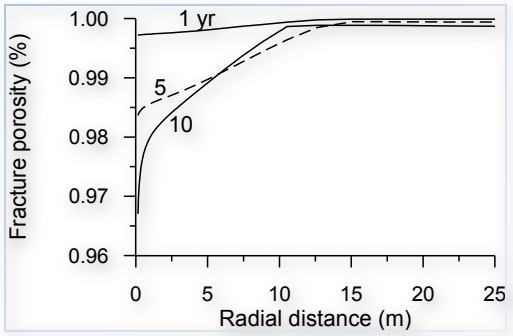

(a) Porosity

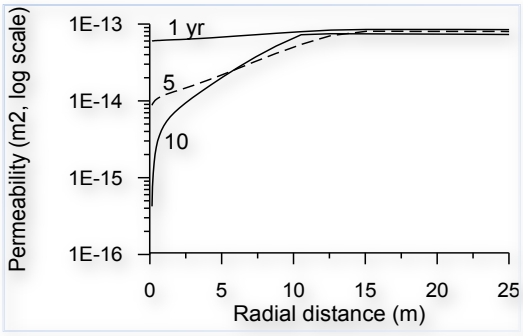

(b) Permeability

Figure 1.8—8 Predicted amorphous silica precipitation along the well radius.

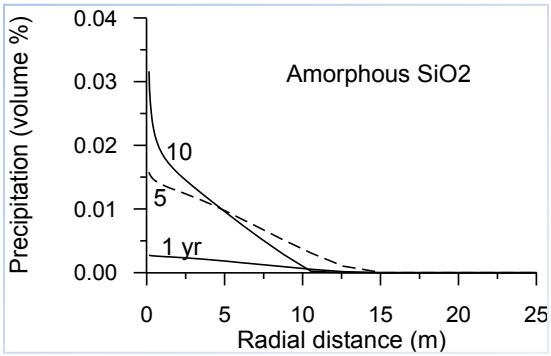

For only one simulation corresponding to Figure 8.8-6, input and output files are provided with the distribution files. To shorten the simulation time for benchmarking purposes, the time in the PARAM input block of flow.inp is specified as 3.5478e+07 s (1/10 of the entire simulation time and slightly longer than 1 year). Users can reset this variable to their desired time.

Other simulations can be achieved by modifying the ϕ_c and n values in file chemical.inp (under key word 'Permeability-Porosity Zones'). As mentioned before, only the fracture network is considered in the simulation. To allow for chemical reaction with the rock, 50% porosity was assigned to the blocks (with 50% pore volume and 50% rock volume). Therefore, an intrinsic porosity of 0.46 (in file chemical.inp) corresponds to bulk $\phi_c = 0.46 \times 2\% = 0.92\%$.

After the first phase of simulations of injectivity loss due to silica scaling, a simulation of acidizing for the injectivity recovery was performed. For the actual acidizing, a 5 wt% (about 2.5 mol/kg) HF acid was injected for five hours at an average rate of 18.2 kg/s. In the recovery simulation, a HF concentration of 1.25 mol/kg was used to account for some dilution by wellbore and formation waters. The predicted amount of amorphous silica dissolved by acid was also consistent with the estimated amount. Detailed results are given in Xu et al. (2004b).

1.8.4 Summary

A review of historical injection records, fluid chemistry data, and analyses of scale materials suggest silica scaling at Nag-67 occurred mainly in the rock formation immediately adjacent to the wellbore. Silica scaling (precipitation) decreases porosity, and in turn permeability and injectivity. A reactive transport numerical model, including the porosity-permeability relationship of Verma and Pruess (1988) was used to simulate injection loss and recovery. The porosity-permeability relationship involves two parameters: a "critical" porosity ϕ_c (which is the value of porosity at which permeability goes to zero) and a power term n (Eq. F.8). A number of simulations were performed using different combinations of values of ϕ_c and n under two different injection silica concentrations.

Significant precipitation of amorphous silica, and reductions of porosity and permeability occur within a 10 m radius from the well. The pattern of log10 scale of permeability is similar to linear scale of porosity. The simulated injection indexes were compared to measured data for each simulation. A good match was obtained using different parameter combinations; a smaller critical porosity ϕ_c requires a larger power term n. The porosity-permeability relationship is well suited for capturing the steep loss of injectivity at Nag-67. A steep reduction in permeability with a small decrease in porosity is consistent with a published permeability experiment. Taking an injection silica concentration of 705 ppm, within the range of observed values, results in a total amorphous silica precipitation of 2 m^3 in the reservoir formation, close to the amount of 1.4 m^3 estimated from the quantity of acid used to recover injectivity.

1.9 Problem 9 – Denitrification and Sulfate Reduction

1.9.1 Problem statement

To test the applicability of TOUGHREACT to reactive transport of denitrification and sulfate reduction, the column experiments of von Gunten and Zobrist (1993) were modeled. The experimental data were first used by Zysset et al. (1994) for their macroscopic model involving the transport of dissolved substances in groundwater-biofilm systems. Later, Doussan et al. (1997) used the same experimental data set for their model testing. They treated the diffusion dominated microscopic transport processes within the biofilm by using a mass-transfer coefficient in the macroscopic transport equations. These experiments were designed to simulate infiltration of an organically polluted river into an aquifer. Thus, synthetic river water, including an organic substrate (lactate) and electron acceptors of oxygen, nitrate and sulfate, were injected into columns filled with river sediments. Results of two column experiments were reported (von Gunten and Zobrist, 1993). The two columns have the same size of diameter 5 cm and length 29 cm. The model aquifer was a sand fraction (0.125 - 0.25 mm) from a fluvio glacial deposit. The sand contains only a small amount

of organic material (<0.1%). The columns were kept at ambient temperature. Column 1 was inoculated at the inflow with an aqueous extract from a humus soil. Column 2 was inoculated with 1 g of material from the first 1-2 cm of Column 1. In the first column, only nitrate is added to the solution as an electron acceptor. In the second column, oxygen, nitrate, and sulfate are used as electron acceptors. The TOUGHREACT simulation results for experiments of two columns have been presented in Xu (2008).

1.9.2 Biodegradation kinetics and parameters

As described by the previous investigators, three major microbially-mediated reactions are involved in the experiments. Three electron acceptors are reduced, while dissolved organic matter (DOC) using lactate ($C_3H_5O_3^-$) in the experiment, are oxidized as follows:

$$3O_2(aq) + C_3H_5O_3^- \rightarrow 3HCO_3^- + 2H^+ \tag{8.9.1}$$

$$12NO_3^- + 5C_3H_5O_3^- + 2H^+ \rightarrow 15HCO_3^- + 6N_2(aq) + 6H_2O \tag{8.9.2}$$

$$3SO_4^{2-} + 4C_3H_5O_3^- \rightarrow 4C_2H_3O_2^- + 4HCO_3^- + 3HS^- + H^+ \tag{8.9.3}$$

The bacterial growth rates due to three different electron acceptors are given in Equations (8.9.4), (8.9.5) and (8.9.6), respectively. Denitrification is inhibited by oxygen, and sulfate reduction is inhibited by both oxygen and nitrate. The rate parameters for Equations (8.9.4) through (8.9.6) are given in Table 8.9-1.

$$r_b^{O_2} = k_b^{O_2} X_b \left(\frac{C_{DOC}}{K_{DOC}^{O_2} + C_{DOC}} \right) \left(\frac{C_{O_2}}{K_{O_2} + C_{O_2}} \right) \tag{8.9.4}$$

$$r_b^{NO_3} = k_b^{NO_3} X_b \left(\frac{C_{DOC}}{K_{DOC}^{NO_3} + C_{DOC}} \right) \left(\frac{C_{NO_3}}{K_{NO_3} + C_{NO_3}} \right) \left(\frac{I_{O_2 \rightarrow NO_3}}{I_{O_2 \rightarrow NO_3} + C_{O_2}} \right) \tag{8.9.5}$$

$$r_b^{SO_4} = k_b^{SO_4} X_b \left(\frac{C_{DOC}}{K_{DOC}^{SO_4} + C_{DOC}} \right) \left(\frac{C_{SO_4}}{K_{SO_4} + C_{SO_4}} \right) \left(\frac{I_{O_2 \rightarrow SO_4}}{I_{O_2 \rightarrow SO_4} + C_{O_2}} \right) \left(\frac{I_{NO_3 \rightarrow SO_4}}{I_{NO_3 \rightarrow SO_4} + C_{NO_3}} \right) \tag{8.9.6}$$

The overall biomass growth rate is expressed as

$$r_b = r_b^{O_2} + r_b^{NO_3} + r_b^{SO_4} - bX_b \tag{8.9.7}$$

where X_b is biomass concentration (mg/l), b is decay constant, and a value of 5.787×10^{-7} 1/s was used according to Doussan et al. (1997).

Table 1.9—1 **List of biodegradation rate parameters used in Equations (8.9.4) through (8.9.6) (according to Doussan et al., 1997).**

	O_2	NO_3	SO_4
Maximum specific growth constant k (1/s)	1.1574×10^{-4}	1.1667×10^{-5}	3.01×10^{-6}
Half-saturation constant of electron acceptors (mg/l)	0.77	7	5.35
Half-saturation constant of electron donor (mg/1)	3	3	3
Inhibition constants (mg/1)	$O_2 \rightarrow NO_3$ 10^{-3}		O_2 , $NO_3 \rightarrow SO_4$ 2×10^{-3}

In this example, biomass is assumed not subject to transport. Most of the bacteria are fixed on the solid phase within geologic media. A general multi-region model for hydrological transport interacting with microbiological and geochemical processes was used (Figure 8.9-1). The model consists of: (1) a mobile region (a fraction of the porosity), (2) an immobile region (another fraction of the porosity), and (3) a solid particle region where mineral dissolution/ precipitation and surface reactions may occur. Here the immobile region contains stagnant water and biomass. Currently, TOUGHREACT does not consider the dynamic changes in the volume of immobile region. The dynamic changes in porosity and volume will be implemented in the future. In principle, the multi-region model is similar to the model of "multiple interacting continua'' (MINC) for resolving “global” fluid and heat flow and diffusion of chemicals in fractured rock and their interaction with the “local” exchange between fracture and matrix rock (Pruess and Narasimhan, 1985). Details on the multi-region model can be found in Xu (2008).

Figure 1.9—1 **Schematic representation of a multi-region model for resolving local diffusive transport.**

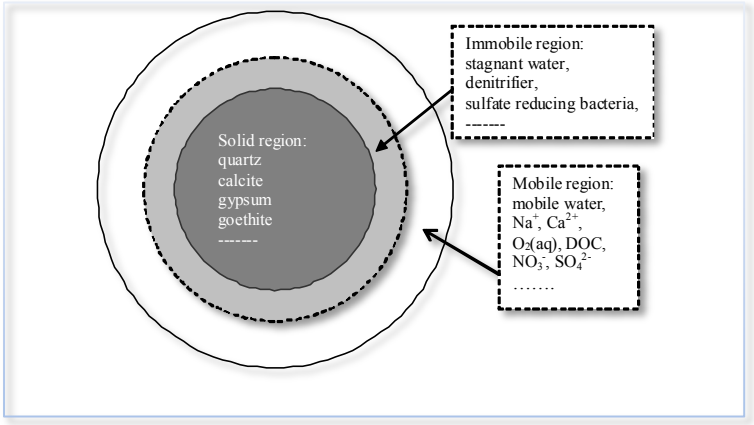

1.9.3 Denitrification

In the first column, only nitrate is added to the solution as an electron acceptor. As mentioned above, Doussan et al. (1997) modeled the reactive transport of denitrification in Column 1. They treated the diffusion-dominated microscopic transport processes within the biofilm by a mass-transfer coefficient, which was calibrated by the experimental data. Maximum specific growth rates and half-saturation constants were also calibrated. These calibrated parameters were also used for their Column 2 simulation. These parameter estimates were obtained with biomass growth. A yield coefficient of 0.4 was used in their simulations.

The experiments were started by inoculating the water in the columns with a small amount of bacteria, but no biomass concentration is reported in von Gunten and Zobrist (1993). Here a starting biomass concentration of 0.15 mg/l calibrated by Zysset et al. (1994) was used. Initial concentrations for all other species are set equal to a very small value of 10^{-10} mg/l (practically zero, because TOUGHREACT uses log10 calculations for a better convergence). Constant concentrations at the boundary were used in the simulation, which are given in Table 8.9-2. A diffusion coefficient of 1×10^{-9} m^2/s was used.

Table 1.9—2 **Boundary conditions used in the column experiments. Values are experimental data taken from Doussan et al. (1997).**

	Column 1	Column 2
Injection flow rate (Darcy velocity, m/day)	1.8	0.37
O_2 (mg/l)		7
NO_3 (mg/l)	34.1	18.6
SO_4 (mg/l)		21.5
DOC (mg/l)	43.2	43.2

The physical parameters used for the three regions are given in Table 8.9-3. For the first trial run, 15% of the bulk porosity (0.4) was assumed for the immobile region. In the multi-region simulations, a porosity of 1 was assigned for the mobile region and a porosity of 0.5 was assigned for the immobile region consisting of stagnant water and biomass. Changes in porosity caused by bacterial growth are not currently considered. A 0.05 porosity was assumed for the solid particle region. In Section 8.9.5, a mineral composition is assigned for the solid particle region to illustrate the coupling of microbially-mediated redox reactions with mineral dissolution and precipitation. The distance (Table 8.9-3, $d = d_1 + d_2$) between the mobile and immobile regions is assumed to be 2×10^{-5}

m, a fraction of the sand particle sizes range from 1.252×10^{-4} to 2.52×10^{-4} m (von Gunten and Zobrist, 1993). The interfacial area (A) was calibrated by matching the measured nitrate concentrations. The d between the immobile and solid regions (3×10^{-5} m) was set slightly larger than the mobile-immobile regions. The same A was used for immobile and solid regions. In fact, diffusive flux between regions is proportional to $D_0\tau A/d$, where D_0 is diffusion coefficient (10^{-9} m^2/s) and τ is tortuosity. The τ between two regions is calculated according to values in two regions (see Table 8.9-3) by $\tau = (d_1\tau_1+d_2\tau_2)/(d_1+d_2)$. Values of d, D_0, τ, and A all affect the diffusive flux. Therefore, errors in d, D_0, and τ will be passed along to A, because only the interfacial area is calibrated. The other conditions and parameters are unchanged from the previous 1-D porous medium simulation.

Table 1.9—3 List of physical parameters used for the three regions.

Parameter	Hydro-Region	Bio-Region	Chem-Region
Volume fraction of the medium	0.34	0.06 (15% of the bulk porosity)	0.60
Porosity	1.0	0.5	0.05
Distance (in m)	d_1	d_2 d_1	d_2
	10^{-5}	10^{-5} 10^{-5}	2×10^{-5}
Tortuosity	0.5	0.3	0.1
	0.4	0.1667	

The concentration profile of nitrate at different times obtained with the multi-region model is presented in Figure 8.9-2. Starting from a 15% immobile region, the 7-day curve agrees well the observed data. However, the 14-day curve is above the corresponding data (less reactive), but improved from the porous model. This may result from bacterial growth increasing volume of the immobile region. Currently, we simply let the run stop at 7 days and then restart by increasing the immobile region to 25% of the bulk porosity. The diffusion length was kept the same. Dynamic changes of the diffusion length together with immobile region volume and the interfacial area will be addressed in the future. The 14-day curve of 25% immobile region captures the observed data (Figure 8.9-2). Only one data point at (x = 0.0167) was off the curve, possibly because of other reasons (such as measurement errors). The simulated concentrations of dissolved organic carbon (DOC) and biomass obtained are presented in Figure 8.9-3. DOC decreases slowly here and is not a limiting factor for the bacterial growth. The growth is very slow until 7 days; then it accelerates dramatically.

The matches were adjusted with the interfacial area A between mobile and immobile regions. The calibrated values are 38 m^2 per cubic bulk medium for the initial period, 75 m^2 for the

late period. The match and parameter calibration suggest that TOUGHREACT can not only be a useful interpretative tool for biogeochemical experiments, but also can produce insight into processes and parameters of microscopic diffusion and their interplay with biogeochemical reactions.

Figure 1.9—2 **Nitrate concentrations obtained with the multi-region model after 7 and 14 days, together with measured data.**

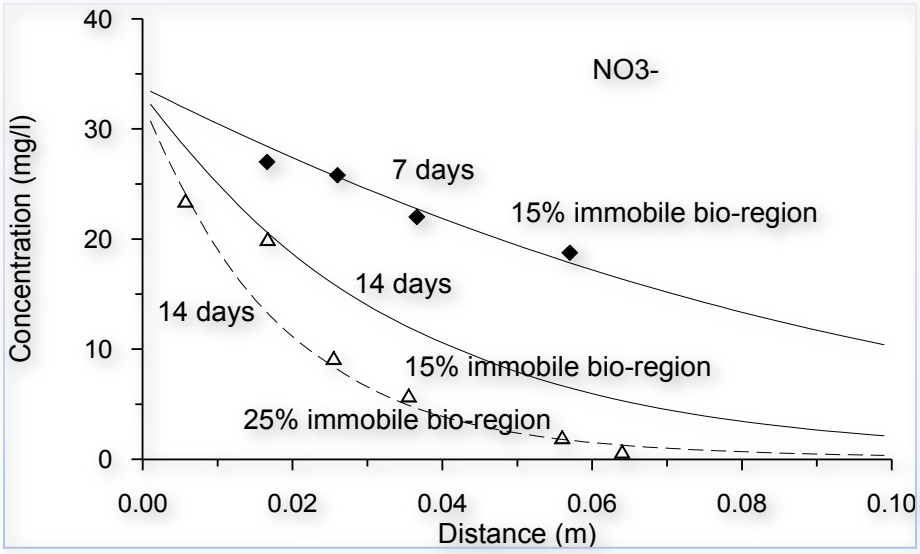

Figure 1.9—3 **Concentrations of dissolved organic carbon (DOC) and biomass obtained with the multi-region model after 7 and 14 days.**

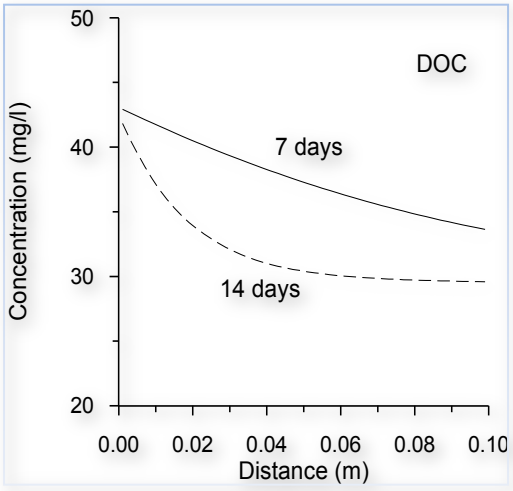

(a) DOC

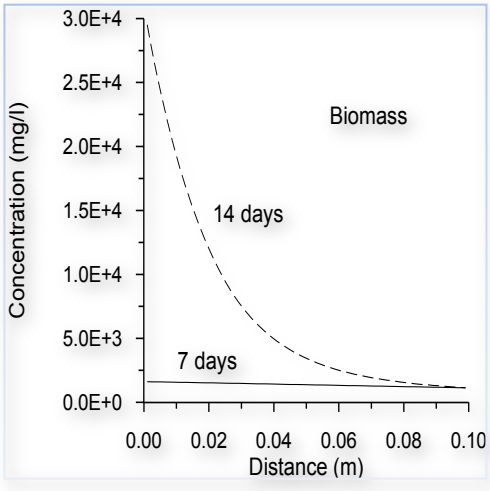

(a) Biomass

The EOS9 flow module is used for this denitrification problem. The flow and solute transport input files are similar to the previous examples. Here we only present the chemical input file in Figure 8.9-4. The complete input and output files are provided with the distribution files.

Figure 1.9—4 Chemical input file (chemical.inp) for Problem 9.

```
# Title
'Column a of Nitrate problem in Doussan et al., 1997, in Contam. Hydrology'
# '-------------------------------------------------------------------------------'
# 'DEFINITION OF THE GEOCHEMICAL SYSTEM'
# 'PRIMARY AQUEOUS SPECIES'  NoTransport
'h2o'                       0
'h+'                        0
'no3-'                      0
'DOC'                       0     ! Dissolved organic matter
'biomass'                   1     ! Biomass, not subject to transport
'*'
# 'AQUEOUS KINETICS'
  2                         ! Total number of kinetic aqueous reactions
  1                         ! Denitration, NO3-
       4   -6.195 'no3-' -2.5 'DOC'  1.0 'biomass'   -1.665e-5 'h+'  ! Consumption:
negative; production positive
       1      1              ! rate model index, No.mechanism
          1.6667E-5          ! rate constant (mass/L/s, maximum specific growth rate
          1   'biomass' 2  1.0                          ! Product    term,   2
means concentration
          2   'DOC'   2  3.0    'no3-' 2  7.0           ! Monod      terms
          0                                            ! Inhibition terms
  2                           ! Biomass decay
       1     1.0 'biomass'    ! Consumption: negative; production positive
       1     1                ! rate model index; No.mechanism
         -5.787d-07           ! rate constant (decay constant, -b here)
          1   'biomass' 2  1.0                          ! Product    term,
          0                                            ! Monod      terms
          0                                            ! Inhibition terms
'*'
# 'AQUEOUS COMPLEXES'
'oh-'
'*'
# 'MINERALS'
'*'
# 'GASES'
'*'
# 'SURFACE COMPLEXES'
'*'
# 'species with Kd and decay    decay constant(1/s)'
'*'
# 'EXCHANGEABLE CATIONS'
'*'
# '-------------------------------------------------------------------------------'
# 'INITIAL AND BOUNDARY WATER TYPES'
3   1       ! niwtype, nbwtype = number of initial and boundary waters
# Index  Speciation T(C)  P(bar)
1          20.0           1.0
# '        icon        guess         ctot          '
'h2o'        1        1.000e+00      1.000e+00  '*'  0.
'h+'         3        1.0e-7         1.0e-7     '*'  0.         ! mol/l
'no3-'       1        1.0e-10        1.0e-10    '*'  0.         ! mg/l
'DOC'        1        1.0e-10        1.0e-10    '*'  0.         ! mg/l
'biomass'    1        1.5e-80        1.5e-80    '*'  0.         ! mg/l
'*'
# Index  Speciation T(C)  P(bar)
2          20.0           1.0
# '        icon        guess         ctot          '
'h2o'        1        1.000e+00      1.000e+00   '*'  0.
'h+'         3        1.0e-7         1.0e-7      '*'  0.      ! mol/l
'no3-'       1        1.0e-10        1.0e-10     '*'  0.      ! mg/l
```

```
'DOC'         1        1.0e-10        1.0e-10      '*'  0.      ! mg/l
'biomass'     1        1.0e-0         1.0e-0       '*'  0.      ! mg/l
'*'
# Index  Speciation T(C)  P(bar)
3          20.0            1.0
# '        icon        guess         ctot          '
'h2o'        1        1.000e+00      1.000e+00    '*'  0.
'h+'         3        1.0e-7         1.0e-7       '*'  0.      ! mol/l
'no3-'       1        1.0e-10        1.0e-10      '*'  0.      ! mg/l
'DOC'        1        1.0e-10        1.0e-10      '*'  0.      ! mg/l
'biomass'    1        1.5e-80        1.5e-80      '*'  0.      ! mg/l
'*'
# Index  Speciation T(C)  P(bar)
1          20.0            1.0
# '        icon        guess         ctot          '
'h2o'        1        1.000e+00      1.000e+00    '*'  0.
'h+'         3        1.0e-7         1.0e-7       '*'  0.
'no3-'       1        34.1           34.1         '*'  0.
'DOC'        1        43.2           43.2         '*'  0.
'biomass'    1        1.5e-80        1.5e-80      '*'  0.
'*'
# '-------------------------------------------------------------------------------'
# 'INITIAL MINERAL ZONES'
'*'
# '-------------------------------------------------------------------------------'
# 'INITIAL gas ZONES'
'*'
# '-------------------------------------------------------------------------------'
# 'Permeability-Porosity Zones'
'*'
# '-------------------------------------------------------------------------------'
# 'INITIAL SURFACE ADSORPTION ZONES'
'*'
# '---------------------------------------if Sden=0 Kd store retardation factor'
# 'INITIAL LINEAR EQUILIBRIUM Kd ZONE'
'*'
# '---------------------------------------if Sden=0 Kd store retardation factor'
# 'INITIAL ZONES OF CATION EXCHANGE'
'*'
# '-------------------------------------------------------------------------------'
# 'end'
```

1.9.4 Sulfate reduction

The evolution of sulfate in the Column 2 experiment of von Gunten and Zobrist (1993) was simulated together with that of oxygen and nitrate. Organic matter is successively oxidized by oxygen, nitrate, and sulfate. Denitrification is inhibited by oxygen, whereas sulfate reduction is inhibited by both oxygen and nitrate. The multi-region model used 25% of the bulk porosity (0.4) for the immobile region throughout the simulation. The increased immobile volume was attributed to (1) a longer simulation time (35 over 14 days) and (2) more electron acceptors (three over one). An interfacial area of 75 m^2 per cubic meter bulk medium, calibrated from the simulation of 7 to 14 day of Column 1 was used for the simulation of Column 2. The two columns have different injection flow rates (1.83 m/day for Column 1, and 0.37 m/day for Column 2). All other physical parameters were assumed to be the same as Column 1, because the sediment material is the same in both columns. Simulated concentrations of sulfate captured the measured data well (Figure 8.9-5). According to von Gunten and Zobrist (1993), the spatial resolution of the experiments did not allow for clear

separation of oxygen respiration from denitrification. Virtually complete nitrate reduction took place within the first several centimeters of the flow distance. The simulation results are consistent with the nitrate observations.

Figure 1.9—5 The simulated concentration profiles (lines) of sulfate, nitrate, and oxygen at steady-state (35 days), together with measured data of sulfate along Column 2.

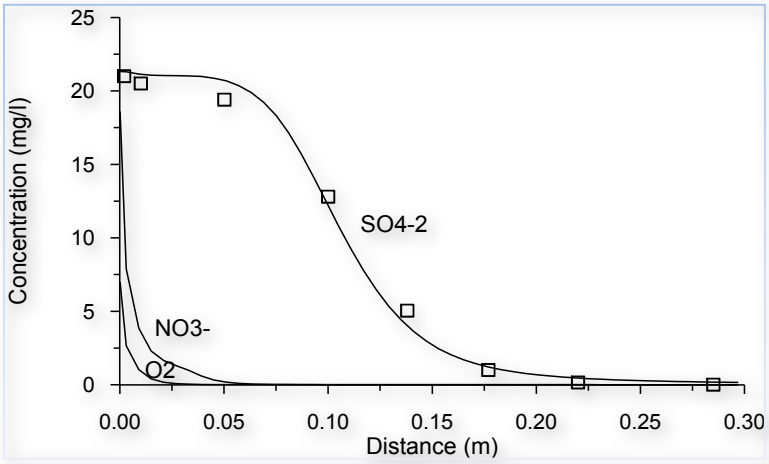

1.9.5 Interacting with the solid particle

To illustrate the possible participation of minerals in the solid particle region, and the interplay between biodegradation and geochemical reactions, two reactive minerals gypsum and goethite were assumed to be initially present in the region. SO_4 dissolved from gypsum diffuses to the immobile region and then is reduced to HS. In the solid region, Fe generated from goethite dissolution and HS diffused back from the immobile region may precipitate as pyrite. Ca from gypsum and HCO_3 from organic matter biodegradation may form calcite. The later two minerals were specified as potential secondary minerals. The parameters used for the rate law Equation (B.12) in Appendix B are presented in Table 8.9-4, only neutral mechanism was considered. Rate constants for goethite and pyrite were increased by 5 orders of magnitude from the values in Palandri and Kharaka (2004), who compiled and fitted many of the experimental data reported by a large number of investigators. The rate increase was for explicitly accounting for bacterial catalysis. The dissolution-rate constants for gypsum and calcite were assigned to be two times those of goethite and pyrite. The assigned geochemical reaction rates could be comparable to sulfate bio-reduction. Note that kinetic parameters, volume fractions and reactive surfaces in Table 8.9-4 may not reflect the field conditions, but the purpose of considering mineral dissolution and precipitation is to demonstrate the TOUGHREACT capabilities for geochemical processes. It should also be mentioned that typically the abundant iron in sediments is present as Fe(Ⅲ) and it inhibits sulfate reduction. This inhibition

effects is not considered here. However, in the pH range of natural waters, Fe(Ш) is extremely insoluble and dissolved iron exists mainly as Fe(П) (von Gunten and Zobrist, 1993).

Table 1.9—4 List of parameters for calculating kinetic rate of dissolution and precipitation of minerals.

Mineral	Chemical formula	Volume fraction (%)	Specific surface area (cm^2/g)	k ($mol/m^2/s$)
Gypsum	$CaSO_4 \cdot 2H_2O$	4	9.8	5.0×10^{-7}
Goethite	FeOOH	2	9.8	2.5×10^{-7}
Pyrite	FeS_2	0	9.8	2.5×10^{-7}
Calcite	$CaCO_3$	0	9.8	5.0×10^{-7}

The biogeochemical simulation of the multi-region model was based on sulfate reduction of Column 2, using 25% of the bulk porosity for the immobile region and an interfacial area of 75 m^2 per cubic meter medium. An arbitrary increased initial biomass concentration of 60 mg/l was used to allow for significant biodegradation from the start. Initial concentrations for all other species are set equal to a very small value. Only DOC is assumed to be available in the injection water, with a concentration of 10 mg/l. The only electron acceptor SO_4 results from the leaching of the materials in the solid region (gypsum dissolution).

Simulation results are presented in Figures 8.9-6 and 8.9-7. SO_4 concentrations increase along the distance (Figure 8.9-6a) because of gypsum dissolution (Figure 8.9-7b; Ca concentrations take on the same pattern). Significant SO_4 concentration gradients occurs between solid and immobile regions because of (1) consumption by sulfate reduction in the immobile region and (2) larger d of solid-immobile (3×10^{-5} over 2×10^{-5} m) and smaller τ (see Table 8.9-3). SO_4 concentration in the immobile region is slightly higher than that in the mobile region. HS concentrations are higher in the immobile region due to sulfate reduction there (Figure 8.9-6b), but its concentrations are reduced in the solid region resulting from the sink of pyrite precipitation (Figure 8.9-7d). HCO_3 concentrations increase (Figure 8.9-6c) and DOC decrease (Figure 8.9-6d) along the distance because of biodegradation. The difference of the latter two species among the three regions is very small.

Bacterial growth rates over the distance (Figure 8.9-7a) increase close to the inlet, because of the increase in SO_4 concentration, but later downstream decreases due to the low DOC concentrations. Biomass concentrations increase almost linearly with time. Returning to the solid region, pyrite precipitation pattern is similar to that of goethite dissolution. The former volume is slightly larger than the latter because of the slightly larger mole volume (23.94 over 20.82 cm^3/mol). Calcite was not found in the simulation for the shorter column distance, but it could form along flow path if the distance was long enough, because the HCO_3 concentrations steadily increase (Figure 8.9-

6c). Gypsum dissolution promotes bio-reduction of sulfate. Then the bio-generation of HS reacts with Fe from goethite dissolution, resulting in pyrite precipitation. Geochemical processes in the solid region and micro-biological processes in the immobile region influence each other via micro-diffusion.

Figure 1.9—6 Simulated concentrations of dissolved components in the three regions after 13 days for the biogeochemical simulation.

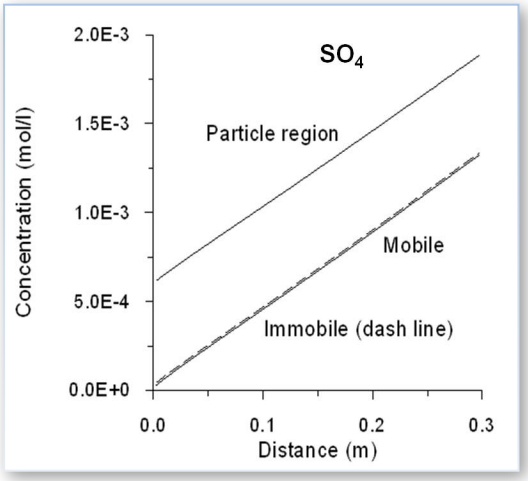

(a) SO4

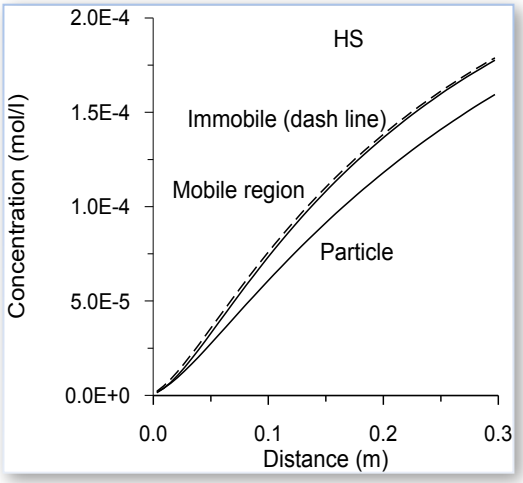

(b) HS

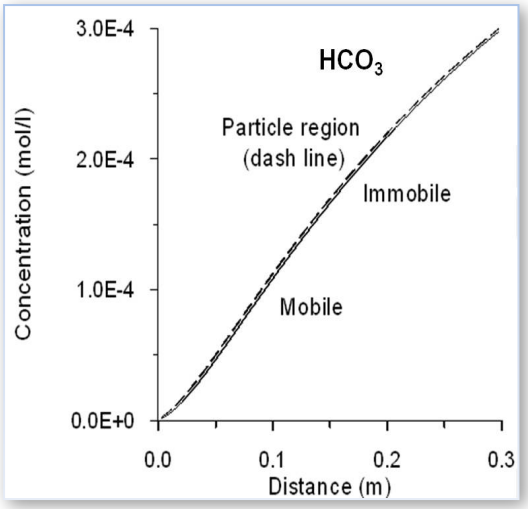

(c) HCO3

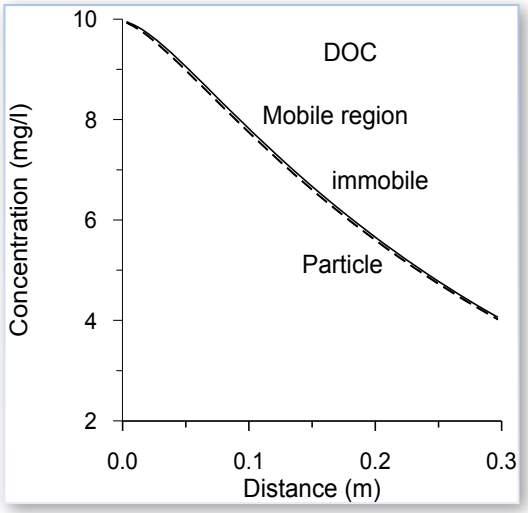

(d) DOC

Figure 1.9—7 Simulated biomass concentrations in the immobile region (a) and mineral dissolution and precipitation in the solid region (b, c, and d) at different times.

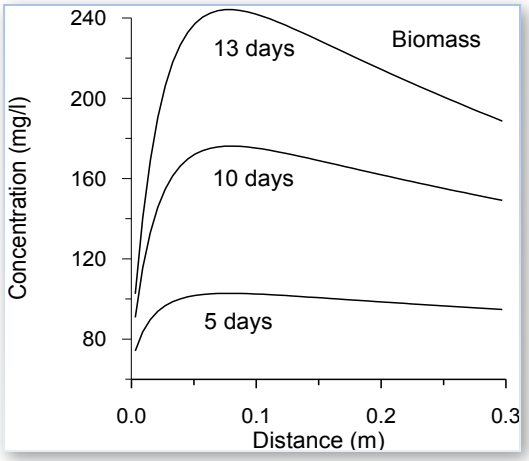

Biomass

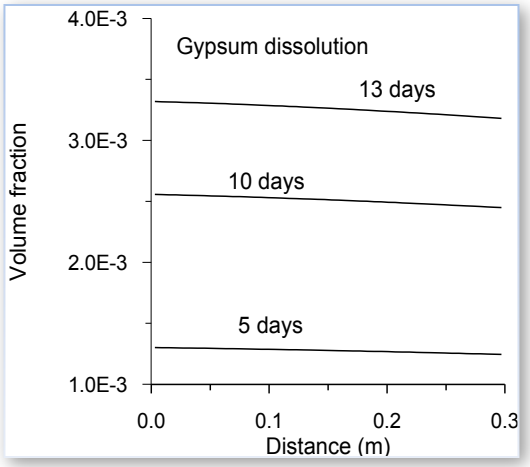

Gypsum

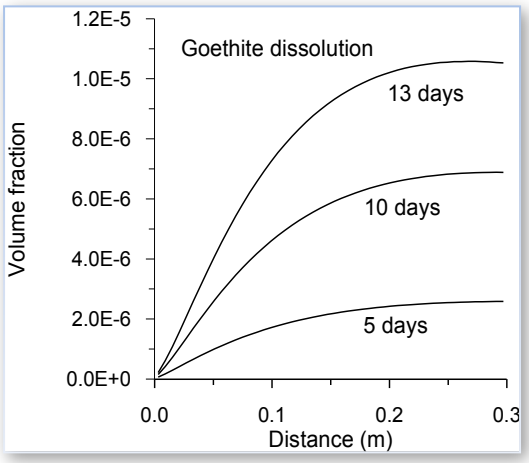

Goethite

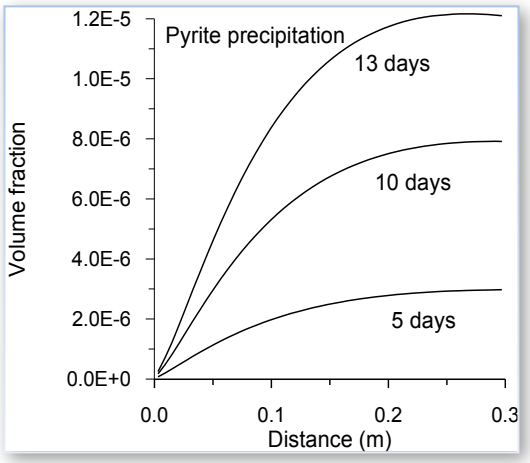

Pyrite

1.9.6 Summary

The applicability of this enhanced multi-region model for reactive transport of denitrification and sulfate reduction was evaluated by comparison with column experiments and model calibration. The matches with measured nitrate and sulfate concentrations were adjusted with the interfacial area between mobile and immobile regions. The values of 38 m^2 per cubic bulk medium for the initial period and 75 m^2 for the late period were calibrated. The match and parameter calibration suggest that TOUGHREACT can not only be a useful interpretative tool for biogeochemical experiments, but also can produce insight into the processes and parameters of microscopic diffusion and their interplay with biogeochemical reactions.

The interacting of an immobile region with solid particles consisting initially of reactive-minerals gypsum and goethite, was modeled. Gypsum dissolution promotes bio-reduction of sulfate,

after which the bio-generation of HS reacts with Fe from goethite dissolution, resulting in pyrite precipitation. It has been shown that geochemical processes in the solid region and micro-biological processes in the immobile region influence each other via micro-diffusion.

The resulting biogeochemical-transport-simulation capabilities may be useful for many subsurface problems, including acidic mine drainage remediation, organic matter decomposition, oil and gas maturation, sulfite reduction in oil fields, and effective environmental remediation of groundwater contamination. However, evaluation of the model against experimental data at larger than a column, and in multi-dimensional flow fields, is recommended before to field-scale problems.

1.10 Problem 10 – Biogeochemical Cycling of Heavy Metals in Lake Sediments

This example builds on the work presented by Sengor et al. (2007a, b) on modeling the diffusive transport of heavy metals (Zn, Pb, Cu) in the sediments of Lake Coeur d'Alene, Idaho. Details on the conceptual model and implemented biogeochemical reaction network are given in Sengor et al. (2007a) and summarized below.

The sediments of Lake Coeur d'Alene have been heavily impacted by mining activities and, as a result, contain elevated concentrations of iron and heavy metals. These sediments contain significant amounts of iron hydroxides, primarily as ferrihydrite (Toevs et al., 2006; Moberly et al. 2009), together with quartz and siderite as major minerals. The microbial reductive dissolution of iron hydroxides in the sediments is thought to lead to the release of metals sorbed onto these mineral phases, generating benthic fluxes of metals from the sediments to the lake water (Balistrieri, 1998; Kuwabara et al., 2003). Deeper into the sediments, metals mobilized by reductive dissolution become immobilized by reaction with biogenic sulfide to form sulfide minerals. These coupled processes are simulated for a 1D sediment column under redox disequilibrium conditions (Figure 8.10-1).

Figure 1.10—1 Conceptual 1D diffusive biogeochemical model (Sengor et al., 2007a)

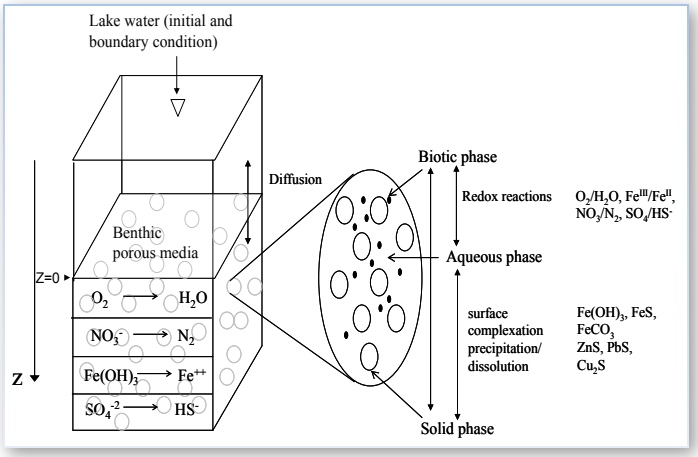

The model setup and input data are essentially unchanged from the model presented earlier (Sengor et al. 2007a), which was built using PHREEQC (Parkhurst and Appelo, 1999). The model incorporates a multicomponent biotic reaction network with multiple terminal electron acceptors (TEA) (Table 8.10-1), diffusive transport, mineral precipitation and dissolution, and surface complexation. The switch from one TEA to the next is implemented using inhibition factors (K^{in} in Table 8.10-1) in the manner proposed by Van Cappellen and Gaillard (1996). We have added to the original 1-D model the effect of sedimentation, approximated by advecting sediment solids and pore water downward at a rate decreasing with depth to mimic compaction. In addition to species originally considered for sorption onto Fe hydroxides (Zn^{2+}, Cu^{2+}, Cu^{+}, Pb^{2+}, H^{+}, Ca^{2+}, Mg^{2+}, SO_4^{2-}; Dzombak and Morel, 1990), Fe^{2+} surface complexation (Liger et al., 1999) was also added to the original model. Note that rate laws for the various biotic reactions (Table 8.10-1) are multiplied by a thermodynamic affinity term ($1 - Q/K$, where Q and K are the ion activity product and the equilibrium constant, respectively, of the reaction) that effectively shuts down the reaction if/when equilibrium is reached (at which point $Q = K$).

Table 1.10—1 **Microbial reactions and rate laws (from Sengor et al., 2007a). See Table 8.10-2 for parameter values.**

Microbially mediated reactions:

$CH_3COO^- + 2O_2 \rightarrow 2CO_3^{-2} + 3H^+$ R_{O2}

$CH_3COO^- + 1.6NO_3^- \rightarrow 2CO_3^{-2} + 0.8N_2 + 1.4H^+ + 0.8H_2O$ R_{NO3}

$CH_3COO^- + 8Fe^{+3} + 4H_2O \rightarrow 8Fe^{+2} + 2CO_3^{-2} + 11H^+$ R_{Fe+3}

$CH_3COO^- + SO_4^{-2} \rightarrow 2CO_3^{-2} + HS^- + 2H^+$ R_{SO4-2}

Kinetic rate laws:

$$R_{O2} = V_m^{O2} \frac{[O_2]}{[O_2] + K_s^{O2}}$$

$$R_{NO3} = V_m^{NO3} \frac{[NO_3]}{[NO_3] + K_s^{NO3}} \frac{K_{O2}^{in}}{K_{O2}^{in} + [O_2]}$$

$$R_{Fe+3}^{(*)} = V_m^{Fe} \frac{K_{O2}^{in}}{K_{O2}^{in} + [O_2]} \frac{K_{NO3}^{in}}{K_{NO3}^{in} + [NO_3]}$$

$$R_{SO4-2} = V_m^{SO4} \frac{[SO_4^{2}]}{[SO_4^{2}] + K_s^{SO4}} \frac{K_{O2}^{in}}{K_{O2}^{in} + [O_2]} \frac{K_{NO3}^{in}}{K_{NO3}^{in} + [NO_3]} \frac{K_{Fe}^{in}}{K_{Fe}^{in} + [Fe^{+3}]}$$

V_m^i Maximum substrate utilization rate constant
K_s^i Half saturation constant
K_i^{in} Inhibition constants
(*) Assumes unlimited Fe^{+3} supply from abundant solid Fe hydroxides

Table 1.10—2 **Values of parameters in Table 8.10-1 (from Sengor et al., 2007a, except for V_m^{Fe}). The value of V_m^{Fe} was recalibrated to take into account the effect Fe(II) sorption onto ferrihydrite, which was ignored in the original model.**

Parameter (units)	Model Value
V_m^{O2} (s^{-1})	5×10^{-9}
V_m^{NO3} (s^{-1})	2×10^{-10}
V_m^{Fe} (s^{-1})	15×10^{-12}
V_m^{SO4} (s^{-1})	3×10^{-9}
K_s^{O2} (molal)	2.41×10^{-5}
K_s^{NO3} (molal)	1.13×10^{-4}
K_s^{SO4} (molal)	1×10^{-3}
K_{O2}^{in} (molal)	1.61×10^{-8}
K_{NO3}^{in} (molal)	1×10^{-7}
K_{Fe}^{in} (molal)	1×10^{-8}

The top model boundary is located at the lake water-sediment interface. It is set at a fixed composition equal to the (measured) composition of lake water equilibrated with sorption sites on ferrihydrite. Transport is entirely diffusive, with a closed bottom model boundary. The simulated 1D sediment column is 45 cm long, with a grid spacing of 0.5 cm for the first top 8 cells, then increasing

to 1 cm through the remainder of the column. The sedimentation rate is set at 2 cm/yr at the top of the column (Horowitz et al., 1995), and linearly decreasing to zero at the base of the column. The diffusion coefficient is low (~4×10^{-6} cm^2/s), reflecting very fine-grained sediments (Ballistrieri, 1998). Simulations are carried out for a period of about 5 years, after which nearly steady conditions prevail.

The same aqueous reaction network is modeled as in Sengor et al. (2007a) (Tables 8.10-1 and 8.10-2). Higher in the sediment column, iron-reducing bacteria reduce iron hydroxides:

$$8Fe(OH)_{3(s)} + CH_3COO^- + 15H^+ \rightarrow 8Fe^{2+} + 2HCO_3^- + 20H_2O \qquad (8.10.1)$$

This reaction leads to the release of sorbed metals (Zn, Cu, Pb). At depth, sulfate reducing bacteria produce sulfide, which can react with Fe(II) and other metals to form precipitates:

$$Fe^{2+} + CH_3COO^- + SO_4^{2-} \rightarrow FeS_{(s)} + 2HCO_3^- + H^+ \qquad (8.10.2)$$

Reactions (8.10.1) and (8.10.2) represent overall reactions that proceed though the coupling of the reaction network (Table 8.10-1) with ferrihydrite (modeled as $Fe(OH)_3$) and mackinawite (FeS, disordered) reacting at equilibrium. Sphalerite (ZnS), galena (PbS) and chalcocite (Cu_2S) are included as "proxy" phases precipitating under kinetic constraints to provide a sink for heavy metals. Siderite ($FeCO_3$) is also included as a phase reacting under kinetic constraints. The only minerals initially present in the modeled column consist of ferrihydrite and siderite, which are observed throughout the lake sediments in significant amounts (Toevs et al., 2006), likely from both detrital and diagenetic origins (Table 8.10-3).

Simulations are started with (oxic) lake water (Table 8.10-4) initially throughout the column. Redox stratification eventually develops through the microbial reaction network (Table 8.10-1), from oxic lake-water conditions at the top of the column to sulfate-reducing conditions at the bottom of the column. Kinetic reaction parameters are initially obtained from the literature, then are adjusted as necessary to best match the model results to field data (Winowiecki, 2002) (Figure 8.10-2). Note that the electron donor is taken as acetate, which is reported in pore water at ~150 μM and is assumed un-limiting.

Table 1.10—3 Minerals included in the simulation, and reaction constraints.

Mineral	Initial Amount (% Volume)	Constraint on reaction	$k \times A$ (mol s^{-1} kg^{-1}_{water})
Ferrihydrite	1.4	Equilibrium	None
FeS	none	Equilibrium	None

Siderite	10	$R_{FeCO3} = kA(Q/K-1)$	5×10^{-14}
Sphalerite[1]	none	$R_{ZnS} = kA[Zn^{+2}][H_2S](Q/K-1)^{0.01}$	2.7×10^{-3}
Galena[1]	none	$R_{PbS} = kA[Pb^{+2}][H_2S](Q/K-1)^{0.01}$	2.7×10^{-3}
Chalcocite[1]	none	$R_{Cu2S} = kA[Cu^{+}][H_2S](Q/K-1)^{0.01}$	2.7×10^{-3}

For each mineral, k and A represent the rate constant and reactive surface area, respectively, and Q and K represent the activity product and solubility product, respectively. Values of $k \times A$ were roughly calibrated, and intentionally kept low for heavy metal sulfides, which are only used here as "proxies" for precipitation in various sulfide forms. The form of the rate law for sulfides is after Rickard (1995), except for the $(1-Q/K)$ term, which was added to ensure the rate convergence to zero at equilibrium. The small exponent on this term is meant to keep it near 1 except at equilibrium when this term drops to 0.

Table 1.10—4 Input water composition (oxic lake water, from Sengor et al., 2007a).

Components	Concentration	Units
pH (25°C)	7.2	
Cl	1.95×10^{-5}	molal
$CO_{3(tot)}$	3.54×10^{-4}	molal
SO_4	5.83×10^{-5}	molal
Ca	1.37×10^{-4}	molal
Mg	8.64×10^{-5}	molal
Na	1.00×10^{-4}	molal
K	1.28×10^{-5}	molal
NO_3	8.00×10^{-5}	molal
$O_{2(aq)}$	4.25×10^{-4}	molal
Fe	3.11×10^{-9}	molal
Pb	5.31×10^{-8}	molal
Zn	8.72×10^{-6}	molal
Cu	1.18×10^{-8}	molal

Modeled concentrations trends for key species are generally consistent with measured data (Figure 8.10-2). The behavior of heavy metals is driven by desorption at shallow depth, accompanied by the microbial reductive dissolution of ferrihydrite, and precipitation with biogenic sulfide deeper into the sediment column. In the present case, the precipitation rates of heavy metal sulfides are kept relatively low and roughly adjusted to yield metal concentrations within the range of observed concentrations. A delicate balance is predicted between the competition of FeS and $FeCO_3$ precipitation for Fe(II), and the competition of soluble (bi)sulfide complexes and sulfide mineral precipitation for biogenic sulfide. Results compare well with the original PHREEQC model developed by Sengor et al. (2007a), with small differences resulting from processes added to the original model, namely Fe(II) sorption onto ferrihydrite and sedimentation, and differences in the affinity terms on the kinetic rate laws of minerals (Table 8.10-3). This example provides a typical application of TOUGHREACT V2.0 to a complex reaction network in a shallow, low-temperature environmental system at redox disequilibrium.

Figure 1.10—2 Concentrations of key parameters, redox species, and metals with depth from the top of the sediment column. Lines show computed values, symbols (Summer 2001: triangle symbols; Fall 2001: square symbols) are measured values by Winowiecki (2002), except for Cu (average over interval shown, from Sengor et al. 2007a).

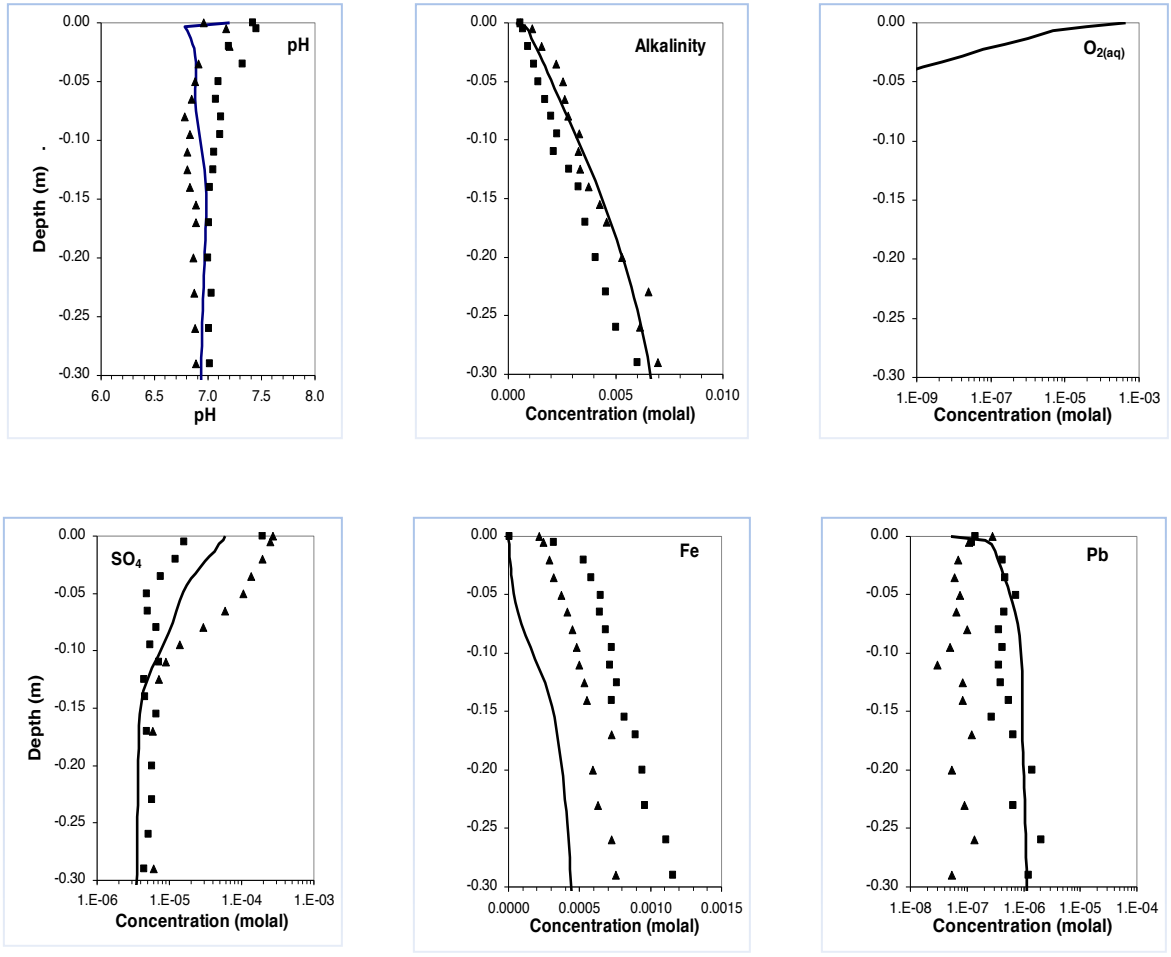

Figure 1.10—3 Computed change in abundance of Fe minerals from the top of the sediment column. The reductive dissolution of ferrihydrite leads to an increase in Fe(II) (Figure 8.10-2) and subsequent FeS and siderite precipitation.

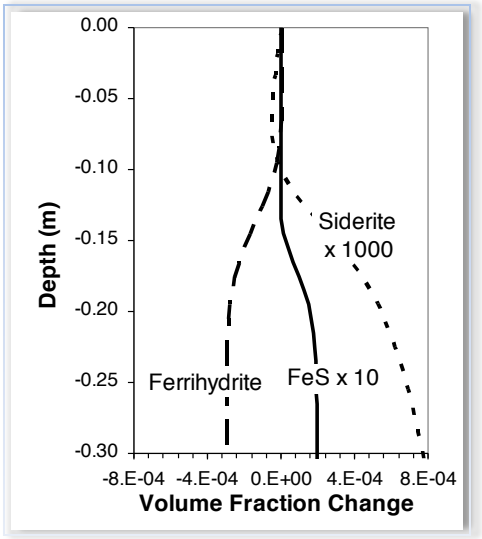

The EOS1 flow module is used for this metal cycling problem. The flow is similar to the previous examples. Here we present the solute and chemical input files in Figures 8.10-4 and 8.10-5, respectively. The complete input and output files are given in the distribution provided with the distribution files.

Figure 1.10—4 Solute input file (solute.inp) for Problem 10.

```
# Title
'LCdA 1D mesh1 '
# ISPIA ITERSFA ISOLVC NGAMM NGAS1 ichdump  kcpl Ico2h2o   nu
    2     0       5       1     0      0       1    0        0
# SL1MIN        rcour     STIMAX    CNFACT(=1 fully implicit)
   1.00e-2      0.000      22.0        1.0
# Read input and output file names:
thermok3.01.dat                ! thermodynamic database
iter.out                       ! iteration information
aqconc.tec                     ! aqueous concentrations in tecplot form
minerals.tec                   ! mineral data  in tecplot form
gases.tec                      ! gas data  in tecplot form
time.out                       ! concentrations at specific elements over time
# ITIME     WUPC    DFFUN     DFFUNG
 1.0       1.0   4.27d-10      0.0
# MAXITPTR  TOLTR    MAXITPCH  TOLCH    MAXITPAD  TOLAD      TOLDC    TOLDR
   1     0.100E-05    300   0.100E-05   30     0.100E-05  0.00E-00 0.00E-00
# NWTI NWNOD NWCOM NWMIN NWAQ NWADS NWEXC iconflag minflag  igasflag
1000    2     19    6    36   17    0        0        1       0
# Nodes for which to output data in time file (15a5):
A21 1BA1 1
# Primary (total) aqueous species for which to output concentrations in time and
plot files:
3 4 5 6 7 8 9 10 11 12 13 14 15 16 17 18 19 20 21
# Minerals for which to output data in time and plot files:
1 2 3 4 5 6
# Individual aqueous species for which to output concentrations in time and plot
files:
8 15 16 18 31 32 33 34 35 36 46 47 48 67 70 75 93 94 95 96 104 105 107 108 109 112
113 114 115 116 117 118 119 20 21 6
# Adsorption species for which to output concentrations in time and plot files:
1 2 3 4 5 6 7 8 9 10 11 12 13 14 15 16 17
# Exchange species for which to output concentrations in time and plot files:
```

```
# IZIWDF IZBWDF IZMIDF IZGSDF IZADDF IZEXDF IZPPDF IZKDDF IZBGDF (default chemical
zones)
    1     0       1    0        1      0      0     0      0
# ELEM(a5) NSEQ NADD IZIW IZBW IZMI IZGS IZAD IZEX izpp IZKD IZBG (chemical zones
for specific nodes)
# this "end" record is needed now
end
```

Figure 1.10—5 Chemical input file (chemical.inp) for the metal cycling problem.

```
# Title
LCdA 1D mesh1
# ---------------------------------------------------------------------------
# DEFINITION OF THE GEOCHEMICAL SYSTEM
# PRIMARY AQUEOUS SPECIES
'h2o'           0
'h+'            0
'hco3-'         0
'ca+2'          0
'cl-'           0
'cu+'            0
'fe+3'          0
'fe+2'          0
'k+'            0
'mg+2'          0
'no3-'           0
'na+'           0
'n2(aq)'        0
'o2(aq)'        0
'pb+2'          0
'hs-'           0
'so4-2'         0
'zn+2'          0
'Ac-'           0
'hfo_soh'       2  'ferrihydrite' 4.428E-07 3
'hfo_woh'       2  'ferrihydrite' 1.780E-05 3
'*'
# AQUEOUS KINETICS
 4                ! total number of kinetic aqueous reactions
  1   !Oxygen TEA
       4   -1.0000 'Ac-' -2.0000 'O2(aq)'  2.0000 'HCO3-'  1.000 'H+'
       1      1                    !kinetic model index,  No.mechanism
          5.0d-09                  !forward rate constant (mol/kg,s)
          0                        !species in product term
          1  'O2(aq)' 1  2.41d-5    !species in monod terms, flag=1 for concentr.,
half sat.cst.
          0                        !species in inhibition terms, flag=1 for
concentr., half sat.cst.
2   !NO3 TEA
6   -1.0000 'Ac-' -1.6000 'NO3-' -0.6000 'H+' 2.0000 'HCO3-' 0.8 'N2(aq)' 0.8 'H2O'
1      1                    !kinetic model index,  No.mechanism
2.0d-10                   !forward rate constant (mol/kg,s)
0                         !species in product term
1 'NO3-'  1  1.13d-4 !species in monod terms, flag=1 for concentr., half sat.cst.
1 'O2(aq)' 1 1.61d-8 !species in inhibition terms, flag=1 for concentr., half
sat.cst.
  3   !FeIII TEA
6  -1.0000 'Ac-' -8.000 'Fe+++' -4.000 'H2O' 8.000 'Fe++' 2.0000 'HCO3-' 9.000 'H+'
       1      1                    !kinetic model index,  No.mechanism
          3.0d-12                  !forward rate constant (mol/kg,s)
          0                        !species in product term
          0                        !species in monod terms, flag=1 for concentr.,
half sat.cst.
          2  'O2(aq)' 1  1.61d-8 'NO3-' 1  1.d-7   !species in inhibition terms
  4
       4   -1.0000 'Ac-'  -1.0000 'SO4--'  2.0000 'HCO3-'  1.000 'HS-'
       1      1                    !kinetic model index,  No.mechanism
          3.0d-09                  !forward rate constant (mol/kg,s)
```

```
          0                          !species in product term
          1 'SO4--'   1  1.e-3       !species in monod terms, flag=1 for concentr.,
half sat.cst.
          3 'O2(aq)'  1  1.61e-8 'NO3-' 1  1.d-7  'Fe+++' 1  1.d-8
'*'
# AQUEOUS COMPLEXES
'*'
# MINERALS         ! equilibrium mineral goes first
'ferrihydrite' 0  0  0   0
0. 0. 0.
'FeS_m' 0  0  0   0
0. 0. 0.
'siderite'   1 3 0  0
1.00e-15 0 1.0 1.0 48.1  0.0 0.0 0.0                  !lowered to get FeS ppt
1.00e-15 0 1.0 1.0 48.1  0.0 0.0 0.0  1.e-12   0       !lowered to get FeS ppt
0.0 0.0 0.0
'chalcocite'  1    3   0    0
              1.e-15     0   1.0  1.0  50.    0.0  0.0  0.0
              0.E-00     2   0.01 1.0  0.0    0.0  0.0  0.0  1.e-12  0
                         1
                         1.e-4    50.   3  'h+' 1. 'hs-' 1. 'cu+' 2.
0.0 0.0 0.0
'galena1'      1    3   0    0
              1.e-15     0   1.0  1.0  50.    0.0  0.0  0.0
              0.E-00     2  0.01  1.0  0.0    0.0  0.0  0.0  1.e-12  0
                         1
                         1.e-4    50.   3  'h+' 1. 'hs-' 1. 'pb+2' 1.
0.0 0.0 0.0
'sphalerite'  1    3   0    0
              1.e-15     0   1.0  1.0  50.    0.0  0.0  0.0
              0.E-00     2   0.01 1.0  0.0    0.0  0.0  0.0  1.e-12  0
                         1
                         1.e-4    50.   3  'h+' 1. 'hs-' 1. 'zn+2' 1.
0.0 0.0 0.0
'*'               0      0    0            0
# GASES
'CO2(g)'       0
'*'
# SURFACE COMPLEXES
'*'
# species with Kd and decay    decay constant(1/s)
'*'
# EXCHANGEABLE CATIONS
'*'
# ------------------------------------------------------------------------------
# INITIAL AND BOUDARY WATER TYPES
1   0   ! niwtype, nbwtype = number of initial and boundary waters
# Index  Speciation T(C)  P(bar)
1            25.0         1.0
#       icon     guess     ctot             constrain
'h2o'     1   0.1000E+01 0.1000E+01           '*'   0.0
'h+'      3   3.981E-08  6.30957E-08          '*'   0.0
'hco3-'   1   3.877e-04  3.535e-04            '*'   0.0
'ca+2'    1   6.239e-04  1.372e-04            '*'   0.0
'cl-'     1   7.899e-05  1.946e-05            '*'   0.0
'cu+'     1   1.180e-08  1.180e-08            '*'   0.0
'fe+3'    2   1.650e-16  3.009e-09 'Ferrihydrite'   0.0 !els 11/26/12 changed guess
'fe+2'    1   1.183e-16  2.034e-19          '*'     0.0 !els 11/26/12 changed guess
'k+'      1   1.586e-04  1.279e-05          '*'     0.0
'mg+2'    1   3.004e-04  8.641e-05          '*'     0.0
'no3-'    1   8.000e-05  8.000e-05          '*'     0.0
'na+'     1   1.001e-04  1.000e-04          '*'     0.0
'n2(aq)'  1   9.150e-19  9.150e-19          '*'     0.0
'o2(aq)'  1   2.5351E-04 4.249e-04          '*'     0.0 !els 11/26/12 changed guess
'pb+2'    1   6.275e-08  5.309e-08          '*'     0.0 !els 11/26/12 changed guess
'hs-'     1   1.000e-32  2.207e-28          '*'     0.0 !els 11/26/12 changed guess
'so4-2'   1   6.142e-04  5.830e-05          '*'     0.0
'zn+2'    1   2.906e-05  8.717e-06          '*'     0.0
'Ac-'     1   7.e-3      7.e-3              '*'     0.0
'hfo_soh' 1   0.1E-07    1.0000             '*'     0.0
'hfo_woh' 1   0.1e-07    1.0000             '*'     0.0
```

```
'*'
# ------------------------------------------------------------------------------
# INITIAL MINERAL ZONES
 1                                        ! nmtype= number of mineral zones
 1                                       ! imtype
#  mineral         volume fraction
'ferrihydrite'   1.3915e-2    0
'FeS_m'          0.0      0
'siderite'       0.1      1
0.0          1107.    0        !area cm2/g assumes 10 micron spherical grains
'chalcocite'       0.0    1
0.0          470.     2        !area m2/3  *por*dens_w to = about 1 for rate law
'galena1'       0.0      1
0.0          470.     2        !area m2/3  *por*dens_w to = about 1 for rate law
'sphalerite'       0.0    1
0.0          470.     2        !area m2/3  *por*dens_w to = about 1 for rate law
'*'
# ------------------------------------------------------------------------------
# INITIAL gas ZONES
'*'
# ------------------------------------------------------------------------------
# Permeability-Porosity Zones
'*'
# ------------------------------------------------------------------------------
# INITIAL SURFACE ADSORPTION ZONES
1                       !ndtype= number of sorption zones
# zone       ad.surf.(cm2/g)  total ad.sites (mol/m2)
1  1    ! zone index, equilibration flag
'hfo_soh'    0    2.049E+06
'hfo_woh'    0    2.049E+06
'*'
# ---------------------------------------if Sden=0 Kd store retardation factor
# INITIAL LINEAR EQUILIBRIUM Kd ZONE
'*'
# ------------------------------------------------------------------------------
# 'INITIAL ZONES OF CATION EXCHANGE'
'*'
# ------------------------------------------------------------------------------
# end
```

1.11 Problem 11 – Heater Test Problem (EOS4 or EOS3)

This test problem of a large-scale *in-situ* thermal test at Yucca Mountain (Nevada) provides a complex 2-D example of coupled thermal, hydrological, and chemical (THC) processes in unsaturated fractured rock. The model setup incorporates many aspects of the capabilities of both TOUGH2 and TOUGHREACT, including time-dependent heat generation, dual-permeability, vapor pressure lowering (EOS4), numerous aqueous, gaseous, and mineral species, CO_2 diffusion (P- and T-dependent), and coupling of permeability and capillary pressure to porosity changes.

1.11.1 Background

The Drift Scale Test (DST) is the second underground thermal test carried out in the Exploratory Studies Facility (ESF) at Yucca Mountain, Nevada. The purpose of the test was to evaluate the coupled thermal, hydrological, chemical, and mechanical processes that take place in unsaturated fractured tuff over a range of temperatures (approximately 25°C to 200°C). Briefly, the DST consists of an approximately 50 m long drift that is 5 m in diameter. Nine electrical floor canister heaters were placed in this drift (the Heated Drift) to simulate nuclear-waste-bearing containers.

Electrical heaters were also placed in a series of horizontal boreholes (wing heaters) drilled perpendicular outward from the central axis of the Heated Drift. These heaters were emplaced to simulate the effect of adjacent emplacement drifts. The DST heaters were activated on December 3, 1997, with a planned period of 4 years of heating, followed by 4 years of cooling. After just over 4 years, the heaters were switched off on January 14, 2002, and since that time the test area has been slowly cooling.

The first predictive model for THC processes in the DST was begun just prior to the initiation of heating in late 1997 with the final predictive report completed several months after the test had begun (Sonnenthal et al. 1998; Xu et al., 2001). The 2-D numerical grid, and thermal and hydrological properties for the THC model were based on the original TH model developed for the DST (Birkholzer and Tsang, 1997; 1998). Model development, results, and data shown in this test problem are based on Spycher et al. (2003b), and Sonnenthal et al. (2005).

1.11.2 Conceptual model for THC processes

The evolution of the chemical regime in the unsaturated zone surrounding a heat source is closely related to the spatial distribution of temperature and the transport of water and vapor. An important aspect of the unsaturated fractured tuff at Yucca Mountain is that the highly permeable fractures are nearly dry, whereas the low permeability and porosity rock matrix has a water saturation of about 90 percent. Heating of the rock results in boiling of the matrix pore water, transport of water vapor into fractures, and condensation along fracture walls. The numerical model for reaction-transport processes in the fractured welded tuffs must account for the different rates of transport in fractures, compared to a much less permeable rock matrix. Transport rates greater than the rate of equilibration via diffusion leads to disequilibrium between waters in fractures and matrix. Because the system is unsaturated, and undergoes boiling, the transport of gaseous species, especially CO_2, is an important consideration. The model must also capture the differences in initial mineralogy in fractures and matrix and their evolution.

In order to handle separate yet interacting processes in fractures and matrix, the dual permeability method has been adopted, such that each grid block is divided into matrix and fracture continua, characterized by their own pressure, temperature, liquid saturation, water and gas chemistry, and mineralogy. In the dual-permeability model, the fracture continuum is considered as co-located but interacting with the matrix continuum, in terms of the flow of heat, water, and vapor through advection, diffusion, and conduction (for heat). The aqueous and gaseous species are transported via advection and molecular diffusion between the fractures and matrix. Each continuum has its own well-defined initial physical and chemical properties.

1.11.3 Drift Scale Test 2-D numerical grid

The two-dimensional dual-permeability numerical grid for the DST represents a vertical cross section through the Heated Drift at a distance approximately 30 m from the bulkhead, separating the Heated Drift from the Access Drift (Figure 8.11-.1a). The mesh consists of 4,490 grid blocks, including fracture and matrix (Figure 8.11-1a and b). The top boundary is approximately 99 m above the drift center, with the bottom boundary at approximately 157 m below the center. The DST includes a plane of linear wing heaters on each side of the drift that are given small grid blocks in the model. Small grid blocks are also employed adjacent to the wing heaters and drift wall to capture the strong gradients in temperature and liquid saturation in these regions (Figure 8.11-1b). Radial mesh blocks in the drift interior were removed from the original mesh and replaced near the drift base by Cartesian grid blocks to represent the concrete invert (Figure 8.11-1b). The Heated Drift grid block is connected directly to the Heater Test Alcove grid block. The connection area and distance were adjusted so that heat loss from the drift resulted in roughly similar crown temperatures to the maximum observed values. In the approximate location of the observation drift, the grid block volumes were increased to a large value to represent connection to the atmosphere. The distances from the drift center grid block and the connecting elements were modified to represent the true distance, so that heat could be applied to the drift center to approximate the effect of the electrical canister heaters.

Figure 1.11—1 **Three-dimensional schematic diagram of the DST showing perspective view of 2-D numerical mesh for DST THC model simulations (mesh extends in all directions from area shown).**

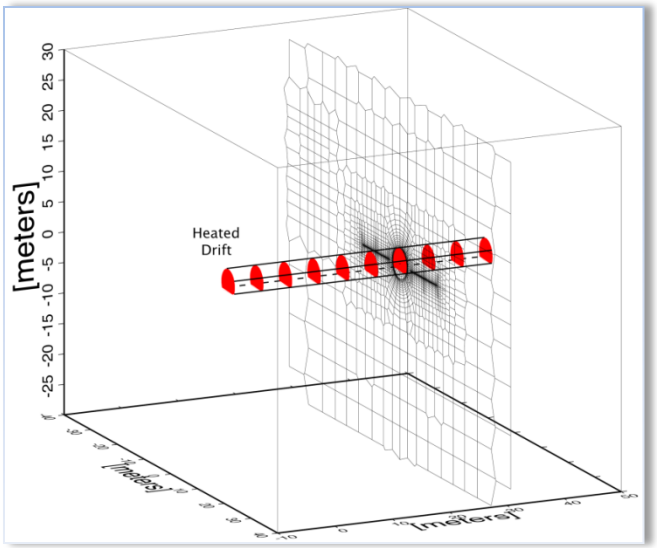

Figure 1.11—2 **Enlarged view of the numerical mesh showing the locations of grid blocks representing the heated drift, wing heaters, and concrete invert.**

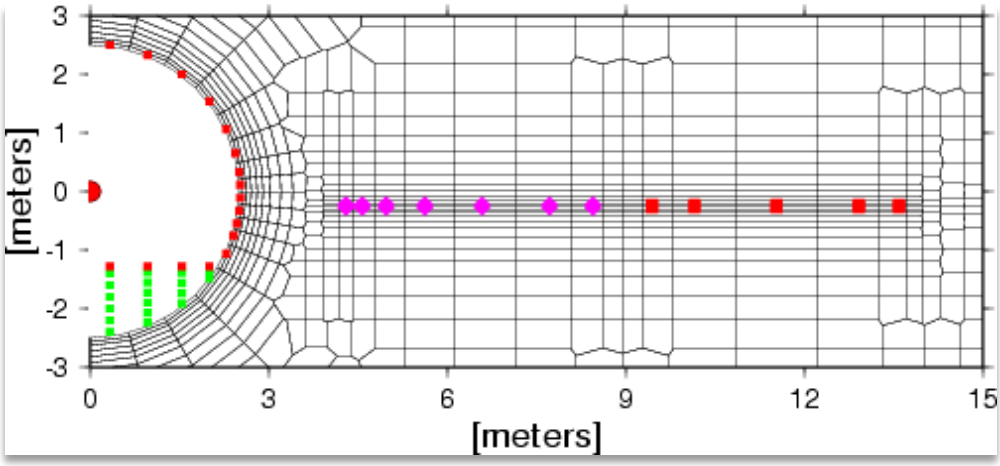

NOTE: Inner (violet diamonds closer to drift) and outer wing heater (red squares) indicate grid block coordinates. Heat was applied to the drift center. Green squares indicate grid block locations for the concrete invert.

In the Heated Drift, heat was applied solely to the drift-center grid block, which is connected to all surrounding grid blocks. The wing heaters are split into inner and outer zones, with more power applied to the outer zone to approximate the presence of an adjacent parallel drift. The positions of grid blocks representing heaters are shown in Figure 8.11-1b. The heating schedule was based on step-wise averages of the 10-day incremented power data. A 9-month initial period is set to the ambient temperature, corresponding approximately to the time that was required to set up the test. Intentional power reductions were directly accounted from the power data. Estimates were made of the duration of the longer (approximately greater than 1/2 day) temporary power outages. Table 8.11-1 gives the step-wise averaged power data implemented in the model simulations in the GENER file. Each time in Table 8.11-1 represents the initiation of a specific period of heating or power loss that continues until the succeeding time. The simulation can be run for the full period of heating plus a 4-year period of cooling (shown by the hypothetical end time at the base of Table 8.11-1). Depending on the speed of floating point calculations on a particular computer, the full simulation could take up to a few days or longer. The complexity of this heating schedule provides a good example of stepwise heat generation in TOUGHREACT.

Table 1.11—1 Step-Wise Averaged Power Data

Date	Time (s)	Time (days)	Canister Power (watts)	WH (inner) Power (watts)	WH (outer) Power (watts)	Comments
3/5/97	0.00000E+00	0.00	0.0000	0.0000	0.0000	pre-test
12/3/97	2.35872E+07	273.00	1091.37407	1232.40	1626.76	heaters turned on
3/15/98	3.24000E+07	375.00	1091.37407	0.0000	0.0000	outage - right rib
3/16/98	3.25080E+07	376.25	1091.37407	1232.40	1626.76	
4/12/98	3.48192E+07	403.00	1077.99	1198.57	1582.12	
8/10/98	4.51872E+07	523.00	1119.68	1201.80	1586.38	
1/27/99	5.98752E+07	693.00	0.0000	0.0000	0.0000	power outage
1/27/99	5.99400E+07	693.75	1123.57	1204.44	1589.86	
2/16/99	6.16032E+07	713.00	1102.59	1189.08	1569.58	
5/27/99	7.02432E+07	813.00	0.0000	0.0000	0.0000	power outage
5/27/99	7.03080E+07	813.75	1102.59	1189.08	1569.58	
5/29/99	7.04160E+07	815.00	0.0000	0.0000	0.0000	power outage
5/30/99	7.04808E+07	815.75	1087.86	1155.52	1525.29	
6/18/99	7.21440E+07	835.00	0.0000	0.0000	0.0000	power outage
6/19/99	7.22088E+07	835.75	1087.86	1155.52	1525.29	
7/9/99	7.39584E+07	856.00	0.0000	0.0000	0.0000	power outage
7/15/99	7.44768E+07	862.00	1087.86	1155.52	1525.29	
8/27/99	7.81920E+07	905.00	0.0000	0.0000	0.0000	power outage
8/29/99	7.83216E+07	906.50	1087.86	1155.52	1525.29	
11/22/99	8.57088E+07	992.00	1087.86	0.0000	0.0000	outage - right rib
11/24/99	8.58816E+07	994.00	1087.86	1155.52	1525.29	
2/11/00	9.27072E+07	1073.00	0.0000	0.0000	0.0000	power outage
2/11/00	9.27720E+07	1073.75	1078.74	1184.66	1563.75	
3/2/00	9.44352E+07	1093.00	1029.19	1115.36	1472.28	power reduction
3/12/00	9.52992E+07	1103.00	0.0000	0.0000	0.0000	power loss
3/13/00	9.54072E+07	1104.25	1029.19	1115.36	1472.28	

5/2/00	9.97056E+07	11 54.00	3	964.526	13	1040.28	13	1373.17	power reduction
8/15/00	1.08778E+08	12 59.00	3	917.346	7	978.639	64	1291.93	power reduction
1/20/01	1.22429E+08	14 17.00		0.0000		0.0000		0.0000	power outage
1/21/01	1.22515E+08	14 18.00	3	917.346	7	978.639	64	1291.93	
5/1/01	1.31155E+08	15 18.00	1	875.571	2	925.467	68	1221.61	power reduction
7/1/01	1.36426E+08	15 79.00		0.0000		0.0000		0.0000	power outage
7/1/01	1.36490E+08	15 79.75	1	875.571	2	925.467	68	1221.61	
8/22/01	1.40918E+08	16 31.00	1	826.817	7	875.831	79	1156.09	power reduction
1/14/02	1.53446E+08	17 76.00		0.0000		0.0000		0.0000	heaters turned off
1/14/06	2.79677E+08	32 37.00		0.0000		0.0000		0.0000	cooling period end

1.11.4 Hydrological and thermal parameters

Values of hydrological and thermal input data are listed in Table 8.11-2. The fracture tortuosity (0.7) is based on models of in situ testing data. This value was further modified for fracture-fracture connections by multiplication of the tortuosity by the fracture porosity of the bulk rock. This operation yields a better approximation for the fracture-to-fracture interconnection area (only for calculation of diffusive fluxes; the entire grid block connection area is used for calculating advective fluxes, because the bulk fracture permeability is used for flow calculations). The capillary pressure in both fractures and matrix must reach some maximum, finite value upon complete dryout (zero liquid saturation). For fractures and matrix in the Tptpmn and Tptpll lithostratigraphic units (model units tsw34 and tsw35, respectively), the limit is set by the calculated slope of the Pcap versus liquid saturation curve at a liquid saturation value equal to Sr + ε. For these units, ε values for the matrix yield maximum Pcap values of 108 Pa (Table 8.11-2); for fractures, ε is set to 0.01 (maximum Pcap values around 103–104 Pa). These specific implementations of the van Genuchten equations are invoked by setting the MOPR(5) parameter to "2", in addition to the specific values given in the ROCKS block.

Table 1.11—2 Hydrological and thermal properties

Model Layer > Lithostratigraphic Unit >		tsw33 Tptpul	tsw34 Tptpmn	tsw35 Tptpll
MATRIX DATA				
permeability	k_m (m^2)	6.57E-18	1.77E-19	4.48E-18
porosity	ϕ_m	0.1425	0.1287	0.1486
van Genuchten α	α_m (1/Pa)	6.17E-6	8.45E-6	1.08E-5

van Genuchten m (or λ)	m_m	0.283	0.317	0.216
residual saturation	Slr_m	0.12	0.19	0.12
satiated saturation	Sls_m	1.00	1.00	1.00
epsilon (for max Pcap)	ε	0.138	0.091	0.216
rock grain density	ρ_g (kg/m3)	2358	2466	2325
rock grain specific heat	Cp (J/kg-K)	985	985	985
dry conductivity	λdry (W/m-K)	1.164*	1.419*	1.278*
wet conductivity	λwet (W/m-K)	1.675*	2.074*	1.890*
tortuosity	τ	0.2	0.2	0.2
FRACTURE DATA[1]				
permeability	k_f (m^2)	7.80E-13	3.30E-13	9.10E-13
porosity	ϕ_f	5.8E-3	8.5E-3	9.6E-3
van Genuchten α	α_f (1/Pa)	1.59E-3	1.04E-4	1.02E-4
van Genuchten m (or λ)	m_f	0.633	0.633	0.633
residual saturation	S_{lrf}	0.01	0.01	0.01
satiated saturation	S_{lsf}	1.00	1.00	1.00
active fracture parameter	Gamma	0.60	0.57	0.57
Frequency	f (1/m)	0.81	4.32	3.16
fracture to matrix area	A (m^2/m^3)	4.44	13.54	9.68
Tortuosity	t	0.7	0.7	0.7
epsilon (at max P_{cap})	ε	0.01	0.01	0.01

NOTE: [1] Fracture thermal properties are derived using matrix properties.
* Bulk conductivities converted from grain conductivity values and lithophysal porosities, using $K_{bulk} = K_{grain}\,(1-\phi_{lith}) + \phi_{lith}\,K_{air}$, with K_{air} = 0.028 (W/m-K) (see Spycher et al., 2003b).

The thermal conductivities of fracture and matrix grid blocks are calculated assuming a linear interpolation between dry and wet conductivities as a function of liquid saturation. These are the thermal conductivities for the solid + fluid system. For fractures, thermal conductivities are multiplied by the fracture porosity to account for the correct fracture-to-fracture connection area in calculations of heat conduction (i.e., this is needed because full grid block areas are input into the model). Fracture thermal conductivities are also reduced by a factor of 10 to account for the limited spatial continuity and connectivity between fracture grid blocks. The volume of the fracture continuum is, however, only a small fraction of the matrix continuum. Therefore heat conduction occurs primarily through the matrix continuum and, as a result, the model is not sensitive to the amount of heat conduction in fractures.

1.11.5 Geochemical input data

Thermodynamic data and kinetic data are provided in the thermok1.01.dat and the chemical.inp files, respectively. Equilibrium and kinetic mineral-water reactions are treated in this test problem. Different representations for reactive surface areas of minerals in fractures and in the porous rock matrix are provided in the chemical.inp file. In most cases, the chemical and physical properties of minerals that form solid solutions are approximated by their individual endmember compositions and properties. An ideal solid-solution model was implemented for smectite (Na, Ca, and Mg endmembers), with each endmember's activity equaling its mole fraction. Treating the smectite as a solid solution, results in individual smectite endmembers either all dissolving or all precipitating, providing a better physical representation of dissolution/precipitation processes. Feldspar solid solutions are not considered because albite (Na-feldspar) and anorthite (Ca-feldspar) are generally strongly undersaturated in the simulations, and thus their dissolution rates are governed primarily by the kinetic rate constant rather than the saturation index. Coupling of permeability to mineral precipitation for fractures is given as a function of the hydraulic aperture and fracture porosity for each rock type (see Appendix F). For the rock matrix it is given as a relation to porosity, using a simplified form of the Kozeny-Carman equation. Coupling of capillary pressure to porosity and permeability is performed using Leverett scaling and "turned on" by setting the MOPR(6) parameter in the flow.inp file to "1".

1.11.6 Initial and boundary conditions: Hydrological and thermal

The top and bottom boundaries were set to constant temperature, pressure, and liquid saturation, based on steady-state values obtained from simulations of a 1-D column extending from the land surface to the water table. The top boundary of the 2-D model extends 150 m above and below the drift center, but does not reach either the land surface or the water table. Under these conditions, the percolation flux at the top boundary is approximately 0.5 mm/yr. The bottom boundary condition is open to gas and to liquid flow. The side boundaries of the domain are located 81.5 m away from the drift center on each side (outside of the test influence area) and are no-flux for mass and heat. The air pressure and temperature in the observation drift are set to constant values. The Heated Drift wall is open to advection and conduction of heat and mass (e.g., air, water vapor, and CO_2). The INCON file provides the steady-state thermohydrological conditions in EOS3 format. Vapor-pressure lowering (EOS4) is implemented by setting MOP(19) = 2, and the simulation can be run using either EOS module.

1.11.7 Initial and boundary conditions: Geochemical

Aqueous and gaseous species concentrations in the rock were initially set to uniform values, based on the measured pore water composition and calculated equilibrium values for CO_2 and some aqueous species. The Heater Alcove and Observation Drift CO_2 concentrations were fixed to

approximately that of the atmosphere. The Heated Drift CO_2 concentration was initially set to the same value as that in the Observation Drift, but was allowed to exchange CO_2 with the Heater Test Alcove and with the surrounding rock. All initial geochemical conditions are provided in the chemical.inp and solute.inp files. Both the top and bottom boundary conditions are open to gas and aqueous species transport. The top and bottom boundaries were also set so that no mineral reactions take place (and therefore no changes in aqueous species concentrations occur as a result of mineral-water reactions). Their volumes were set to extremely large values, so that they act essentially as constant concentration boundaries. The side boundaries are no-flux for gas and aqueous-species transport.

1.11.8 Simulation parameters

The maximum simulation time for this test problem is set in the flow.inp file to 2.75 years (0.75 preheating period plus 2 years of heating), although the GENER file includes the full 8.65 year periods of preheating, heating, and cooling. The maximum time step is set to one day, so that errors due to the non-sequential iteration method, in particular related to gas phase CO_2 diffusion and rapid reaction rates, are reduced.

The corresponding input and some output files are given in the distribution provided with the distribution files. To shorten the simulation time for installation, the simulation time step variable, MCYC, in the PARAM input block of flow.inp is specified as 99. For the full simulation, users can reset MCYC to 9999. In TOUGHREACT, if MCYC = 9999, the simulation time is not controlled by MCYC, and is only controlled by TIMAX in Record PARAM.2 (see section 6.1). Parts of output files for fluid flow, aqueous chemical concentrations, and changes of mineral abundances are given in Figures 8.11-2, 8.11-3 and 8.11-4.

Figure 1.11—3 Part of file flow.out for Problem 11.

```
@@@@@@@@@@@@@@@@@@@@@@@@@@@@@@@@@@@@@@@@@@@@@@@@@@@@@@@@@@@@@@@@@@@@@@@@@@@@@@@@@@@@@@@@@@

  TOTAL TIME    KCYC    ITER  ITERC     KON     DX1M          DX2M          DX3M
 0.31557E+08     438       4    1714       2 0.722897E+03 0.141463E+00 0.386166E+03

@@@@@@@@@@@@@@@@@@@@@@@@@@@@@@@@@@@@@@@@@@@@@@@@@@@@@@@@@@@@@@@@@@@@@@@@@@@@@@@@@@@@@@@@@@

ELEM.  INDEX      P           T           SG          SL          XAIRG       XAIRL

f    5      1 0.88815E+05 0.87783E+02 0.98092E+00 0.19081E-01 0.37598E+00 0.39253E-05
m    5      2 0.91042E+05 0.87777E+02 0.26320E-01 0.97368E+00 0.39684E+00 0.42855E-05
f    6      3 0.88815E+05 0.86723E+02 0.97997E+00 0.20027E-01 0.40981E+00 0.43408E-05
m    6      4 0.90801E+05 0.86723E+02 0.25314E-01 0.97469E+00 0.42707E+00 0.46599E-05
f    7      5 0.88815E+05 0.85056E+02 0.97858E+00 0.21424E-01 0.45893E+00 0.49662E-05
m    7      6 0.90895E+05 0.85056E+02 0.24608E-01 0.97539E+00 0.47513E+00 0.53003E-05
f    8      7 0.88815E+05 0.83021E+02 0.97693E+00 0.23073E-01 0.51283E+00 0.56846E-05
m    8      8 0.91205E+05 0.83021E+02 0.24210E-01 0.97579E+00 0.52914E+00 0.60686E-05
f    9      9 0.88815E+05 0.81053E+02 0.97534E+00 0.24658E-01 0.55941E+00 0.63345E-05
m    9     10 0.91508E+05 0.81053E+02 0.23936E-01 0.97606E+00 0.57562E+00 0.67672E-05
```

```
f  10    11 0.88816E+05 0.79159E+02 0.97379E+00 0.26208E-01 0.59976E+00 0.69207E-05
m  10    12 0.91799E+05 0.79159E+02 0.23748E-01 0.97625E+00 0.61572E+00 0.74002E-05
f  11    13 0.88816E+05 0.76458E+02 0.97152E+00 0.28476E-01 0.65066E+00 0.76934E-05
m  11    14 0.92202E+05 0.76458E+02 0.23586E-01 0.97641E+00 0.66603E+00 0.82376E-05
f  12    15 0.88817E+05 0.73115E+02 0.96863E+00 0.31373E-01 0.70451E+00 0.85541E-05
m  12    16 0.92702E+05 0.73115E+02 0.23538E-01 0.97646E+00 0.71896E+00 0.91785E-05
```

Figure 1.11—4 Part of file aqconc.tec for Problem 11, giving concentrations (mol/kg H2O) of aqueous components after t = 1 yr.

X	Z	T(C)	Sl	pH	ca+2	mg+2	na+	cl-
1.999	-1.534	87.783	0.19081E-01	7.6881	0.7381E-03	0.3550E-03	0.3830E-02	0.3110E-02
1.999	-1.534	87.777	0.97368E+00	7.5975	0.8201E-03	0.3944E-03	0.4262E-02	0.3467E-02
2.039	-1.565	86.723	0.20027E-01	7.6697	0.7663E-03	0.3812E-03	0.4247E-02	0.3392E-02
2.039	-1.565	86.723	0.97469E+00	7.5894	0.8140E-03	0.3827E-03	0.4301E-02	0.3434E-02
2.102	-1.613	85.056	0.21424E-01	7.6478	0.7854E-03	0.3812E-03	0.4172E-02	0.3319E-02
2.102	-1.613	85.056	0.97539E+00	7.5777	0.8287E-03	0.3815E-03	0.4216E-02	0.3349E-02
2.182	-1.674	83.021	0.23073E-01	7.6216	0.8318E-03	0.3938E-03	0.4111E-02	0.3295E-02
2.182	-1.674	83.021	0.97579E+00	7.5595	0.8735E-03	0.3938E-03	0.4142E-02	0.3315E-02
2.261	-1.735	81.053	0.24658E-01	7.5995	0.8852E-03	0.4088E-03	0.4059E-02	0.3290E-02
2.340	-1.796	79.159	0.26208E-01	7.5815	0.9406E-03	0.4238E-03	0.4008E-02	0.3291E-02
2.340	-1.796	79.159	0.97625E+00	7.5252	0.9860E-03	0.4246E-03	0.4022E-02	0.3302E-02
2.459	-1.887	76.458	0.28476E-01	7.5606	0.1024E-02	0.4452E-03	0.3930E-02	0.3293E-02
2.459	-1.887	76.458	0.97641E+00	7.5049	0.1075E-02	0.4466E-03	0.3937E-02	0.3301E-02
2.618	-2.009	73.115	0.31373E-01	7.5418	0.1134E-02	0.4706E-03	0.3830E-02	0.3295E-02
2.618	-2.009	73.115	0.97646E+00	7.4855	0.1193E-02	0.4732E-03	0.3828E-02	0.3300E-02
2.777	-2.131	70.044	0.34129E-01	7.5303	0.1241E-02	0.4941E-03	0.3733E-02	0.3297E-02
2.777	-2.131	70.044	0.97637E+00	7.4735	0.1307E-02	0.4972E-03	0.3726E-02	0.3301E-02
2.975	-2.283	66.538	0.37212E-01	7.5233	0.1371E-02	0.5216E-03	0.3615E-02	0.3299E-02
2.975	-2.283	66.538	0.97613E+00	7.4673	0.1444E-02	0.5239E-03	0.3608E-02	0.3301E-02
3.213	-2.465	62.742	0.40306E-01	7.5246	0.1518E-02	0.5498E-03	0.3489E-02	0.3301E-02
3.213	-2.465	62.742	0.97570E+00	7.4717	0.1593E-02	0.5510E-03	0.3485E-02	0.3302E-02
3.768	-2.892	55.344	0.46284E-01	7.5585	0.1797E-02	0.5883E-03	0.3310E-02	0.3300E-02
3.768	-2.892	55.344	0.97451E+00	7.5205	0.1869E-02	0.5946E-03	0.3283E-02	0.3301E-02

Figure 1.11—5 Part of file tec_min.dat for Problem 11, giving changes in mineral abundances (in volume fraction, positive values indicate precipitation and negative dissolution) after t = 1 yr.

X	Z	gypsum	calcite	microcline	albite-low	anorthite
1.999	-1.534	0.0000E+00	0.2662E-04	-0.4580E-07	-0.4776E-06	-0.1750E-09
1.999	-1.534	0.0000E+00	0.7417E-05	-0.5739E-05	-0.2039E-04	-0.1816E-06
2.039	-1.565	0.0000E+00	0.3083E-04	-0.4868E-07	-0.4713E-06	-0.1691E-09
2.039	-1.565	0.0000E+00	0.7247E-05	-0.6391E-05	-0.1901E-04	-0.1703E-06
2.102	-1.613	0.0000E+00	0.3104E-04	-0.4912E-07	-0.4533E-06	-0.1592E-09
2.102	-1.613	0.0000E+00	0.7166E-05	-0.6191E-05	-0.1869E-04	-0.1536E-06
2.182	-1.674	0.0000E+00	0.2977E-04	-0.4846E-07	-0.4276E-06	-0.1471E-09
2.182	-1.674	0.0000E+00	0.6976E-05	-0.5700E-05	-0.1812E-04	-0.1354E-06
2.261	-1.735	0.0000E+00	0.2820E-04	-0.4752E-07	-0.4026E-06	-0.1360E-09
2.261	-1.735	0.0000E+00	0.6754E-05	-0.5208E-05	-0.1747E-04	-0.1200E-06
2.340	-1.796	0.0000E+00	0.2671E-04	-0.4654E-07	-0.3792E-06	-0.1260E-09
2.340	-1.796	0.0000E+00	0.6526E-05	-0.4747E-05	-0.1681E-04	-0.1070E-06
2.459	-1.887	0.0000E+00	0.2419E-04	-0.4497E-07	-0.3473E-06	-0.1129E-09
2.459	-1.887	0.0000E+00	0.6160E-05	-0.4098E-05	-0.1577E-04	-0.9102E-07
2.618	-2.009	0.0000E+00	0.2079E-04	-0.4301E-07	-0.3107E-06	-0.9848E-10
2.618	-2.009	0.0000E+00	0.5666E-05	-0.3333E-05	-0.1441E-04	-0.7491E-07
2.777	-2.131	0.0000E+00	0.1788E-04	-0.4134E-07	-0.2802E-06	-0.8689E-10
2.777	-2.131	0.0000E+00	0.5201E-05	-0.2691E-05	-0.1315E-04	-0.6304E-07
2.975	-2.283	0.0000E+00	0.1460E-04	-0.3951E-07	-0.2480E-06	-0.7507E-10
2.975	-2.283	0.0000E+00	0.4652E-05	-0.2025E-05	-0.1173E-04	-0.5227E-07
3.213	-2.465	0.0000E+00	0.1068E-04	-0.3739E-07	-0.2154E-06	-0.6369E-10
3.213	-2.465	0.0000E+00	0.4041E-05	-0.1372E-05	-0.1023E-04	-0.4330E-07
3.768	-2.892	0.0000E+00	0.6666E-06	-0.3324E-07	-0.1635E-06	-0.4646E-10

3.768 -2.892 0.0000E+00 0.2849E-05 -0.2941E-06 -0.7633E-05 -0.3160E-07

1.11.9 Model results and comparisons to measured data

Gas-Phase CO_2 Evolution

The concentration of CO_2 in the gas phase is a function of temperature, pressure, aqueous-phase chemistry, mineral-water reactions, and advective and diffusive transport. Simulation results are compared to concentrations measured in gas samples taken from boreholes during the heating phase of the DST. The modeled evolution of CO_2 has been validated by comparison to over 4 years of measurements from the Drift Scale Test. Simulated CO_2 concentrations in the fracture gas phase are shown after 3 years of heating in Figure 8.11-5. The results show the general outward migration of elevated CO_2 concentrations as the boiling front moves outward. The peak in CO_2 concentrations is centered at approximately the 60°C isotherm, and at higher temperatures the concentrations generally decline as a result of degassing and transport with water vapor to cooler regions.

Figure 1.11—6 **Modeled gas phase CO_2 concentrations in fractures after 3 years of heating. Note locations of numbered boreholes collared in the Observation Drift (circle at left).**

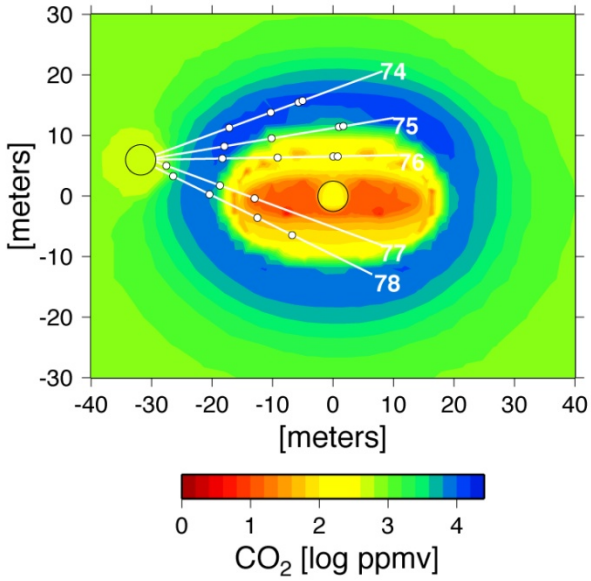

Comparisons of modeled CO_2 concentrations to measurements performed on gas samples from boreholes (shown in Figure 8.11-5) are presented in Figure 8.11-6. Samples were collected from zones a few meters (borehole interval 76-3) to about 15 meters away from the Heated Drift (borehole interval 74-3). Measured concentrations were corrected for water vapor condensation that took place as part of the procedure for gas sampling. Zones closest to the heaters (interval 76-3) exhibit narrower and earlier peaks in concentration compared to zones further out in the rock (interval 74-3). Simulated and measured concentrations are close in magnitude and in their trends.

There is little difference between fracture and matrix concentrations, because of rapid equilibration by advection and diffusion of gas species and their local equilibration with pore water.

Figure 1.11—7 **Modeled CO_2 concentrations in fractures and matrix compared to measured values from boreholes (corrected for vapor condensation) (a) Borehole interval 74-3 (average of bounding grid blocks); (b) Interval 75-3; (c) Interval 76-3.**

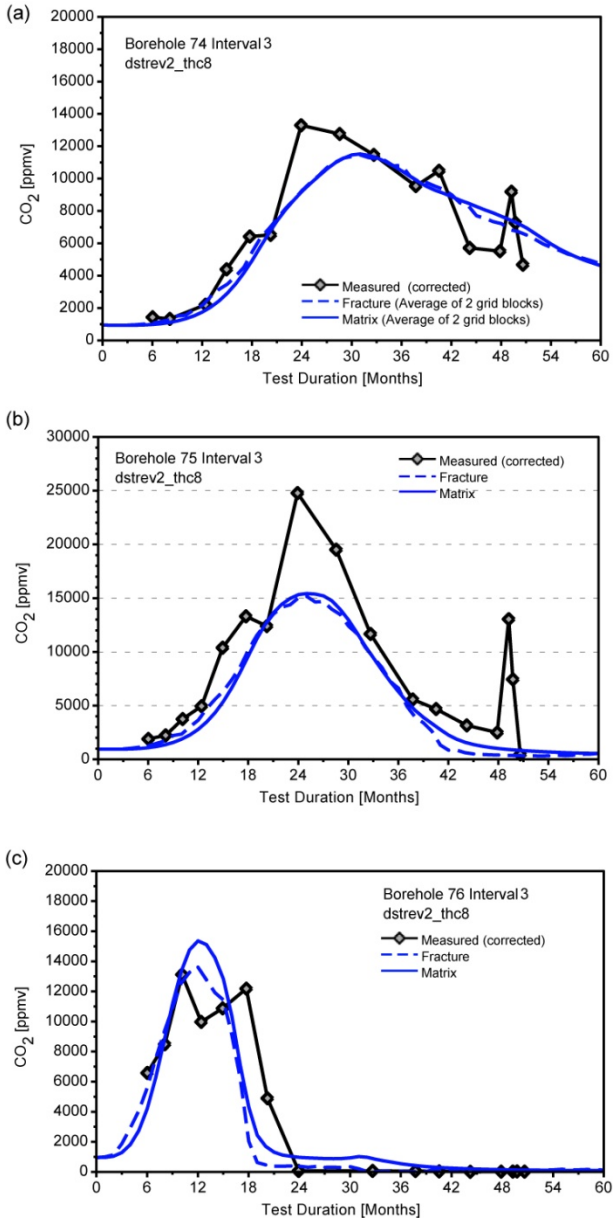

Aqueous species in waters collected in the DST exhibit small reductions in pH, from about pH 8 in the pore water to about 6-8 in condensate waters. The drop in pH is related to the local increases in CO_2 concentrations. Figure 8.11-7 shows an example of the initial drop in pH during vapor

condensation, followed by increasing pH as the zone is further heated and CO_2 is diluted by water vapor.

Figure 1.11—8 **Measured and modeled pH (in fractures) for samples collected from borehole interval 60-3, located below the heaters.**

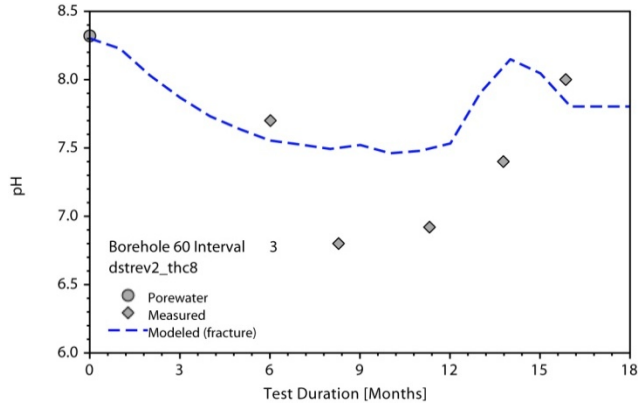

Simulated and measured concentrations of conservative species in the fractures, such as chloride, are much lower than in the initial matrix pore water, indicating that fracture-matrix interaction has been negligible. However, reactive species, such as silica and potassium show significant effects of reaction with fracture-lining silicate minerals.

Mineral Precipitation/Dissolution

Model predictions, followed by analyses of in-situ sidewall core samples, showed that amorphous silica, calcite and lesser amounts of gypsum are the dominant precipitating phases expected in the boiling regions. The greatest amount of mineral precipitation is predicted to be above the heaters where reflux of water condensed in fractures dissolves fracture-lining minerals and is boiled. Simulations and measurements of amorphous silica and calcite, along with locations of observed mineralization are shown in Figures 8.11-8 and 8.11-9. Amorphous silica forms only where strong evaporation by boiling takes place. Calcite also forms in the boiling zones, however calcite that is originally present in fractures dissolves in the lower pH waters that formed in condensation zones around the boiling zone and in the drainage zones below the heaters.

Figure 1.11—9 Volume percent change in amorphous silica abundance in fractures. Filled circle indicates sidewall core sample locations where it was observed.

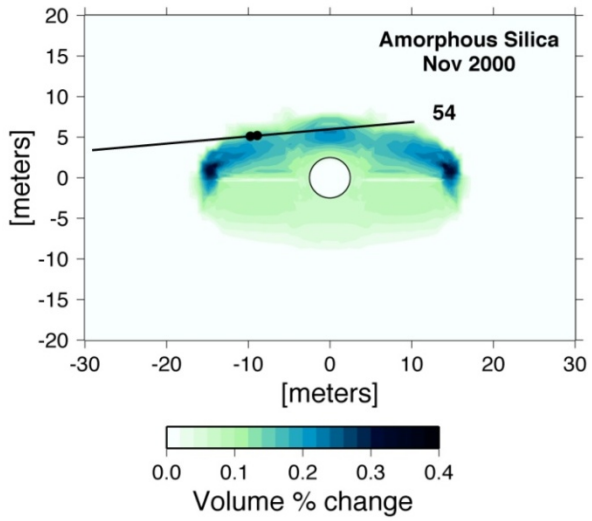

Figure 1.11—10 Volume percent change in calcite abundance in fractures. Filled circle indicates sidewall core sample locations where it was observed.